SURFACE-WATER CONNECTIVITY WITHIN A COASTAL LOWLAND RIVERINE LANDSCAPE

A Dissertation

by

CESAR R. CASTILLO

Submitted to the Office of Graduate and Professional Studies of
Texas A&M University
in partial fulfillment of the requirements for the degree of

DOCTOR OF PHILOSOPHY

Chair of Committee,	İnci Güneralp
Committee Members,	Burak Güneralp
	Anthony Filippi
	Huilin Gao
Head of Department,	David Cairns

May 2020

Major Subject: Geography

ABSTRACT

Lowland riverine landscapes regularly flood and create complex spatial patterns of inundation that create surface-water connections between landscape patches that allow energy, matter, biota, and information to be exchanged. While the importance of surface-water connections has been recognized in the literature, there is no formal framework for quantifying these connections. The research presented here is guided by one main objective that aims to build towards the development of a framework for quantifying surface-water induced landscape connectivity within lowland riverine landscapes. Three specific objectives (SOs) were pursued in order to address this main objective. SO1 involves analyzing potential surface-water connections using a terrain-based approach and developing a methodology that relies on object-based analysis and graph/network theory to quantify connectivity. Results indicate that surface-water connectivity has a nonlinear relationship with river-stage and the connectivity is largely controlled by a hub-like structure. This is important because these hubs are ultimately what maintains river-floodplain process and fluvial habitat health. SO2 involves simulating surface-water inundation across the range of historical flows using a hydrodynamic model and analyzing the hub-like surface-water connectivity structure. Results indicate that the dynamic network created by surface-water connections between landscape patches has a roughly scale-free structure for several of the flow conditions considered. This is important because scale-free networks are known to have universal structure and function that can potentially be used to better understand interactions

between elements of riverine landscape during flood events. SO3 involves developing sets of Stream Temperature, Intermittence, and Conductivity loggers (STICLs) that can monitor surface-water connectivity when deployed in the field. Results indicate that STICLs performed well at identifying intermittent inundation when they are deployed within portions of the riverine landscape that experience periodic inundation. Also, comparing STICL records with those from historical water quality samples allows the flooding mechanism for the inundating waters to be identified. This is important because STICLs provide a means for quantitatively monitoring surface-water connectivity in the field. These SOs collectively progress the development of a framework for quantifying surface-water connectivity of lowland riverine landscapes that ultimately allows for better management of these landscapes.

DEDICATION

I dedicate this work to my loving late father; my loving mother; my sisters and brother; my nieces and nephews; my family as a whole; my friend and mentor Dr. İnci Güneralp; friends I've made throughout my educational journey; and to the wonderful, vastly interesting, and precious planet that we all share.

ACKNOWLEDGEMENTS

I would like to thank my committee chair, Dr. İnci Güneralp, for her never-ending support, guidance, advice, positivity, and patience throughout the pursuit of my graduate degrees. I cannot thank her enough for encouraging her graduate student to pursue his own abstract ideas/methods and for enthusiastically supporting my efforts to secure funding and involve undergraduate students in my research. I would also like to thank my other committee members, Drs. Burak Güneralp, Anthony Filippi, and Huilin Gao for their guidance and support. In particular, I would like to thank Dr. Burak Güneralp for his ideas that helped improve this research and for the enthusiasm with which he evaluated my writings and public presentations. I would like to thank Dr. Anthony Filippi for his guidance on the technical aspects of my research and for his willingness and enthusiasm in helping me collect data in the field. I would like to thank Dr. Huilin Gao for her responsiveness and for her patience in dealing with a graduate student who did not communicate with her as much as he should've throughout the pursuit of this research.

I would also like to thank some of my colleagues. In particular, I thank Billy Hales for being like a brother throughout the entirety of my time spent pursuing my graduate degrees. I cannot thank him enough for all the help he provided on this work and for all the laughs, advice, and willingness to listen to my complaints over all these years. I also thank Eric Guenther for also being like a brother and for all the advice, laughs, and just all-around good times that he provided. I also thank Christy Attaway,

Courtney Guidry, and Mengqu Han for their help in the laboratory- and field-based aspects of this work and for all the laughs and support over the past few years. I also thank Dion Webster, Yair Torres, Andrew Vanderheiden, Matthew Powell, Joseph Wade, Sterlin Shaffer, Victoria Ramos, Megan Tennill, Emerald Starling, Emma Leppard, Nicole Hernandez, Jennifer Avila, Dara Pajouhafsar, and Collin Kohlmeyer for all the help they provided in field-data collection, mapping using Geographic Information Systems, and for their willingness to participate in undergraduate research under the supervision of a graduate student. I also thank other current and previous members of the Fluvial Landscape Dynamics Lab that include Andong Ma, Mingde You, Dongshuo Lu, Ying Liu, Xingchen Chen, Madalyn Caraway, Sydney Weyand, Hoonchong Yi, and Damla Arslan. I thank them for their support and attention when I gave presentations to the lab.

I also want to thank good friends within the Department of Geography that I have made while pursuing my doctoral studies. In particular, I would like to thank Rhett Douris, Carl Greene, Manny Salgado, Jinwoo Park, Taylor Siskind, Rosie Dwight, Crockett Walter, Mackenzie Schoemann, John Schiff, Dan Vecellio, Victoria Ford, Andy Evans, Sarah Trimble, Parveen Chhetri, and Phil Wernette for all the good times. I would also like to thank the faculty within Geography. In particular, I thank Drs. Daniel Goldberg and Andrew Klein for the guidance and employment opportunities that they have provided that not only funded me for over two years, but also allowed me to expand my technical skillset and understanding of how large organizations operate. I also thank Drs. Courtney Thompson, Julie Loisel, and Vatche Tchakerian for their

advice, guidance, and patience with their sometimes-noisy office neighbors. I also thank current and former office staff within Geography that include Carria Collins, Debbie French, Jessica Radnitzer, Fernanda Preciado, Donna Hoover, and Julie Monsees for all their help and patience over the years.

I would also like to acknowledge some other friends and organizations from outside Geography that have had a positive impact on this research. In particular, I thank Chenghai Yang, Fred Gomez, and Lee Denham from the Aerial Application Technology Research Group with the Agricultural Research Service of the U.S. Department of Agriculture for their friendship, sense of humor, advice, guidance, and for the multi-date collection of aerial imagery for my field site. I also thank the staff and leadership of Fennessey Ranch, Mission-Aransas National Estuarine Research Reserve, and the Town of Refugio for providing me and my research group access to their properties and for allowing me to have an extended deployment of instrumentation on their properties.

I also would like to thank my family for all their support, sacrifice, and for never doubting a student who spent a lot more time in school than anyone anticipated. In particular, I would like to thank my late father for all the advice and for the knowledge and skillset that he helped forge that set me apart from others in my situation. Unfortunately, he will not have the opportunity to read this document, but I know that he is still supporting me and my work from afar. I thank my mother for all the love, guidance, strength, and joy that she has provided over the years. She has always been the shining light that has guided my family forward. I thank my sisters and brother for their support and humor that they provided throughout the pursuit of my education. I thank

my nieces and nephews for being such wonderful additions to the family and for driving me to set a good example for them. I also thank Dri Bustos, Greg Lucero, Nallely Estrada, Monica Gonzales, Laly Gutierrez, Jennifer Gutierrez, Lus Ortiz, Nena Bejarano, Ever Bejarano, Damian Bejarano, Rosio Bejarano, Alonso Bejarano, Silvia Bejarano, and other members of my extended family for all the support while pursuing my education.

Finally, I would also like to thank my friends from back in New Mexico for all the laughs and comfort that they have provided while I pursued my graduate degrees. In particular, I want to thank Anthony Lovato, Kristen Weil, Will Byrne, James Sturgis, Bon Baca, Nathan Renley, Jason Quintana, and Eric Quintana for all the love and friendship over the years that I have been away.

CONTRIBUTORS AND FUNDING SOURCES

Contributors

This work was supervised by a dissertation committee consisting of Professors İnci Güneralp, Burak Güneralp, and Anthony Filippi of the Department of Geography and Professor Huilin Gao of the Department of Civil Engineering.

The research design and writing of Chapter II was aided in part by Professors İnci Güneralp and Burak Güneralp of the Department of Geography. Moreover, some of the computer code that was utilized in the analysis of Chapter II was developed by Billy Hales of the Department of Geography. The research design and writing of Chapter III was aided in part by Professors İnci Güneralp and Burak Güneralp. Moreover, the terrain data used in Chapters III and IV was provided by Professor İnci Güneralp that was collected as part of an NSF-GLDP grant and this terrain data was further edited by Billy Hales who also helped develop some of the figures in Chapter III. The research design and writing of Chapter IV were aided in part by Professor İnci Güneralp. Moreover, the data loggers used in Chapter IV in part were developed, calibrated, and deployed by Christy Attaway, Courtney Guidry, and Billy Hales of the Department of Geography.

All other work conducted for the dissertation was completed by the student independently.

Funding Sources

Graduate study was supported by a Graduate Assistant Teaching position from the Department of Geography at Texas A&M University and a Graduate Assistant Non-

Teaching position from the Division of Information Technology at Texas A&M University.

This work was also made possible in part by grants from the National Science Foundation (NSF), Texas Sea Grant (TSG), the Geomorphology Specialty Group of the American Association of Geographers (GSG-AAG), and the College of Geosciences at Texas A&M University (CoG-TAMU) under the Grant Numbers of NSF-GSSP-1657739, NSF-GLDP-1760717, the 2015-2016 TSG Grants-In-Aid of Graduate Research Program, the 2016 GSG-AAG Reds Wolman Graduate Student Research Award, and 2017-2018 CoG-TAMU Expanding High Impact Experiences in the Geosciences Program. Its contents are solely the responsibility of the authors and do not necessarily represent the official views of the Geography and Spatial Sciences Program of the National Science Foundation, the Geomorphology and Land-use Dynamics Program of the National Science Foundation, the Texas Sea Grant College Program, Geomorphology Specialty Group of the American Association of Geographers, or the College of Geosciences at Texas A&M University.

TABLE OF CONTENTS

Page

LIST OF FIGURES

Page

LIST OF TABLES

Page

CHAPTER I

INTRODUCTION

Introduction

Rivers and their floodplains are highly productive and diverse ecosystems that provide valuable ecosystem services such as flood risk reduction, water quality enhancement, and the maintenance of riverine and marine habitats/fisheries (Costanza et al., 1997, Opperman et al., 2010). While only encompassing a small proportion of the global land area (<2%), riverine floodplains contribute >25% of all land-based ecosystem services (Opperman et al., 2010, Tockner and Stanford, 2002); yet, they are some of the most threatened ecosystems around the world. Therefore, understanding the hydrologic, geomorphic, and ecological functioning of riverine floodplains is vital to successful resource management (Tockner and Stanford, 2002).

River-floodplain connectivity is a major driver of water, sediment, and nutrient recycling within river-floodplain systems and it ultimately creates the heterogeneous pattern of habitats and landforms commonly found within these environments (Junk et al., 1989, Meitzen et al., 2013). Flood inundation typically enables the largest and most abrupt material and energy exchanges between the river and its floodplain (Junk et al., 1989, Poff et al., 1997). The flood pulse concept (Junk et al., 1989, Tockner et al., 2000) and hyporheic corridor concept (Stanford and Ward, 1993) are two widely accepted paradigms for predicting the pattern and mechanism of surface water inundation within floodplains and the associated biotic response. While the primary source of flood waters differs between the two paradigms (surface water for the flood pulse concept and

hyporheic/groundwater for the hyporheic corridor concept), both emphasize the significance of interactions along the lateral and vertical dimensions of the riverine landscape (Poole, 2002). The most representative paradigm for a given river-floodplain system will depend on the hydroclimatological regime, floodplain geomorphology and land cover characteristics, and the degree of human modification within the river/floodplain reach. Moreover, the antecedent moisture conditions within a floodplain can also affect the dynamic exchange between the river and its floodplain by allowing widespread floodplain inundation without overbank flows from the river (Mertes, 2002). This type of interplay of water and associated constituents from regional (river) and local (floodplain) sources further complicates the classification of river-floodplain systems with regard to the mechanics of flooding. Regardless of the source of water that leads to river-floodplain connectivity induced by surface water, formally quantifying this connectivity continues to be a problem in hydrologic, geomorphic, and ecological studies (Kupfer et al., 2014, Meitzen et al., 2013).

Recent studies of river-floodplain systems have often employed the hydrologic connectivity approach that has become fundamental in understanding river-floodplain processes and concepts associated with environmental flow policies (Hudson et al., 2013). Pringle (2001) defines hydrologic connectivity as "water-mediated transfer of matter, energy, or organisms within or between the elements of the hydrologic cycle" (p. 981). Overbank flows typically cause the greatest variation in hydrologic connectivity from surface waters (surface-water connectivity, hereafter). However, widespread surface-water connectivity throughout a floodplain can occur below bankfull flow

conditions (Kupfer et al., 2014, Meitzen et al., 2013, Czuba et al., 2019). This variation in river-floodplain connectivity and its influence on sediment and nutrient recycling create the heterogeneous nature of floodplain environments (Poff et al., 1997, Sparks, 1992). Losses in river-floodplain connectivity due to human impacts (e.g., flow/flood control structures (Poff et al., 1997), channel modification (Tockner and Stanford, 2002), and land-use change (Allan, 2004)) across the globe have been well documented in the literature. However, a formal framework for determining the change in landscape connectivity in river-floodplain landscapes under a variety of flow and human influence regimes has so far been lacking.

Research Objectives

The overall objective of this research is to build towards the development of a framework for quantifying landscape connectivity induced by surface-water connections within river-floodplain (or lowland) riverine landscapes. We address this main objective through three specific objectives that involve employing some underutilized methods and tools that can be used to quantify surface-water connectivity dynamics. These specific objectives include:

1. Generate estimates of surface-water inundation and the associated connectivity for a lowland riverine landscape using a terrain-based approach. Moreover, use these estimates to develop an approach for quantifying surface-water connectivity dynamics that utilizes some of the methods employed by the landscape ecology literature that includes object-based analysis and graph/network theory.

2. Analyze the patterns of surface-water connectivity in a lowland riverine landscape generated using a hydrodynamic model and compare them to other connectivity patterns reported in the literature. Moreover, determine other properties of the landscape system that can be inferred from the observed patterns of connectivity.
3. Determine the efficacy with which field-based data loggers can be used to monitor surface-water connectivity in a lowland riverine landscape. Moreover, use low-cost data loggers proposed in the literature that can record common water quality indicators and used the logged values from the data loggers to infer the mechanisms that yielded the surface-water inundation.

References

ALLAN, J. D. 2004. Landscapes and riverscapes: The influence of land use on stream ecosystems. Annual Review of Ecology, Evolution, and Systematics, 35, 257-284.

COSTANZA, R., D'ARGE, R., DE GROOT, R., FARBER, S., GRASSO, M., HANNON, B., LIMBURG, K., NAEEM, S., O'NEILL, R. V., PARUELO, J., RASKIN, R. G., SUTTON, P. & VAN DEN BELT, M. 1997. The value of the world's ecosystem services and natural capital. Nature, 387, 253-260.

CZUBA, J. A., DAVID, S. R., EDMONDS, D. A. & WARD, A. S. 2019. Dynamics of Surface-Water Connectivity in a Low-Gradient Meandering River Floodplain. Water Resources Research, 55, 1849-1870.

HUDSON, P. F., SOUNNY-SLITTINE, M. A. & LAFEVOR, M. 2013. A new longitudinal approach to assess hydrologic connectivity: Embanked floodplain inundation along the lower Mississippi River. Hydrological Processes, 27, 2187-2196.

JUNK, W. J., BAYLEY, P. B. & SPARKS, E. 1989. The floodpulse concept in river-floodplain systems. Canadian Journal of Fisheries and Aquatic Sciences Special Publication, 110-127.

KUPFER, J. A., MEITZEN, K. M. & GAO, P. 2014. Flooding and surface connectivity of Taxodium-Nyssa stands in a southern floodplain forest ecosystem. River Research and Applications, 1-12.

MEITZEN, K. M., DOYLE, M. W., THOMS, M. C. & BURNS, C. E. 2013. Geomorphology within the interdisciplinary science of environmental flows. Geomorphology, 200, 143-154.

MERTES, L. A. K. 2002. Remote sensing of riverine landscapes. Freshwater Biology, 47, 799-816.

OPPERMAN, J. J., LUSTER, R., MCKENNEY, B. A., ROBERTS, M. & MEADOWS, A. W. 2010. Ecologically functional floodplains: Connectivity, flow regime, and scale. Journal of the American Water Resources Association, 46, 211-226.

POFF, N. L., ALLAN, J. D., BAIN, M. B., KARR, J. R., PRESTEGAARD, K. L., RICHTER, B. D., SPARKS, R. E. & STROMBERG, J. C. 1997. The natural flow regime: A paradigm for river conservation and restoration. BioScience, 47, 769-784.

POOLE, G. C. 2002. Fluvial landscape ecology: Addressing uniqueness within the river discontinuum. Freshwater Biology, 47, 641-660.

PRINGLE, C. M. 2001. Hydrologic connectivity and the management of biological reserves: A global perspective. Ecological Applications, 11, 981-998.

SPARKS, R. E. 1992. Risks of altering the hydrologic regime of large rivers. Advances in Modern Environmental Toxicology, 20, 119-152.

STANFORD, J. A. & WARD, J. V. 1993. An Ecosystem Perspective of Alluvial Rivers: Connectivity and the Hyporheic Corridor. Journal of the North American Benthological Society, 12, 48-60.

TOCKNER, K., MALARD, F. & WARD, J. V. 2000. An extension of the flood pulse concept. Hydrological Processes, 14, 2861-2883.

TOCKNER, K. & STANFORD, J. A. 2002. Riverine flood plains: Present state and future trends. Environmental Conservation, 29, 308-330.

CHAPTER II

TERRAIN-BASED ANALYSIS OF SURFACE-WATER CONNECTIVITY WITHIN A COASTAL RIVER-FLOODPLAIN SYSTEM

Introduction

Riverine landscapes are composed of a heterogeneous mosaic of landforms and habitat patches that have co-evolved over time (Harvey and Gooseff, 2015, National Research Council, 2002). This heterogeneity is largely controlled by the periodic connection between the active channel and floodplain/riparian portions of riverine landscape (Poff, 2014, Poff et al., 1997, Poff et al., 2006). The emphasis on connectivity has prompted many studies of river-floodplain systems to employ the hydrologic connectivity approach (Hudson et al., 2013). Hydrologic connectivity has been defined as the water-mediated exchange of energy, matter, and biota between elements of the riverine landscape (Wohl, 2017, Amoros and Roux, 1988, Wohl et al., 2018). Overbank flows typically cause the greatest variation in hydrologic connectivity from surface waters (surface-water connectivity, hereafter). However, widespread surface-water connectivity throughout a floodplain can occur below bankfull flow conditions (Kupfer et al., 2014, Meitzen et al., 2013). Tockner et al. (2000) termed these lower magnitude and higher frequency sub-bankfull flows as “expansion processes”. This variation in river-floodplain connectivity and its influence on sediment and nutrient recycling create the heterogeneous nature of floodplain environments (Poff et al., 1997, Sparks, 1992). Losses in river-floodplain connectivity due to human impacts (e.g., flow/flood control

structures (Poff et al., 1997), channel modification (Tockner and Stanford, 2002), and land-use change (Allan, 2004)) across the globe have been well documented in the literature. However, a formal framework for determining the change in landscape connectivity in river-floodplain environments under a variety of flow and human influence regimes has so far been lacking.

In this study, we examine how surface-water connectivity varies spatially with changes in river-stage within the floodplain of a coastal river in Texas. Specifically, we address the question: What type of relationship does floodplain-level surface-water connectivity have with river stage? Our approach first involves disaggregating the floodplain into hydrologic objects/facets (facets hereafter) in order to characterize the floodplain geomorphology. We then determine the river stage needed for these facets to become connected to the river by using a morphometric approach that mimics a rising water surface level as predicted by the flood pulse concept. We quantify surface-water connectivity within the floodplain as a function of river stage using graph theory. Hydrologic connectivity between a river and specific floodplain features (e.g., oxbow lakes (Bishop-Taylor et al., 2015), vegetation patches (Kupfer et al., 2014), species habitats (Ishiyama et al., 2014)) has been analyzed using graph theory, but little attention has been given to overall floodplain surface-water connectivity. Finally, we discuss how an understanding of the relationship between river-stage and floodplain surface-water connectivity can advance the knowledge-base of river-floodplain interactions and inform management of river-floodplain systems.

Study Area

Our study area is a 16 km stretch of the largely forested Mission River floodplain downstream of the Town of Refugio on the Coastal Bend of Texas (Figure II-1). Numerous floodplain landforms including secondary channels, backswamps, oxbow lakes, cutoffs, abandoned channels, meander scars, natural levees, and bluffs are littered throughout the study area. Elevation generally ranges from 0 to 19 m above sea level with the steepest slopes found along channel banks and edges of the floodplain (Figure II-1c). The study site has a mean slope of 3.1% with a range from 0 to 66% and a main channel slope of 0.1 mm/m. Clay, clay-loam, and sandy-loam are the dominant soils with the finer-grain soils generally found below the steep slopes along the floodplain edge (SSURGO). Floodplain forest/wetlands are the dominant land cover in areas near perennial and secondary channels, while scrub/shrub and pasture/grassland are the dominant land cover types in the uplands (Homer et al., 2015).

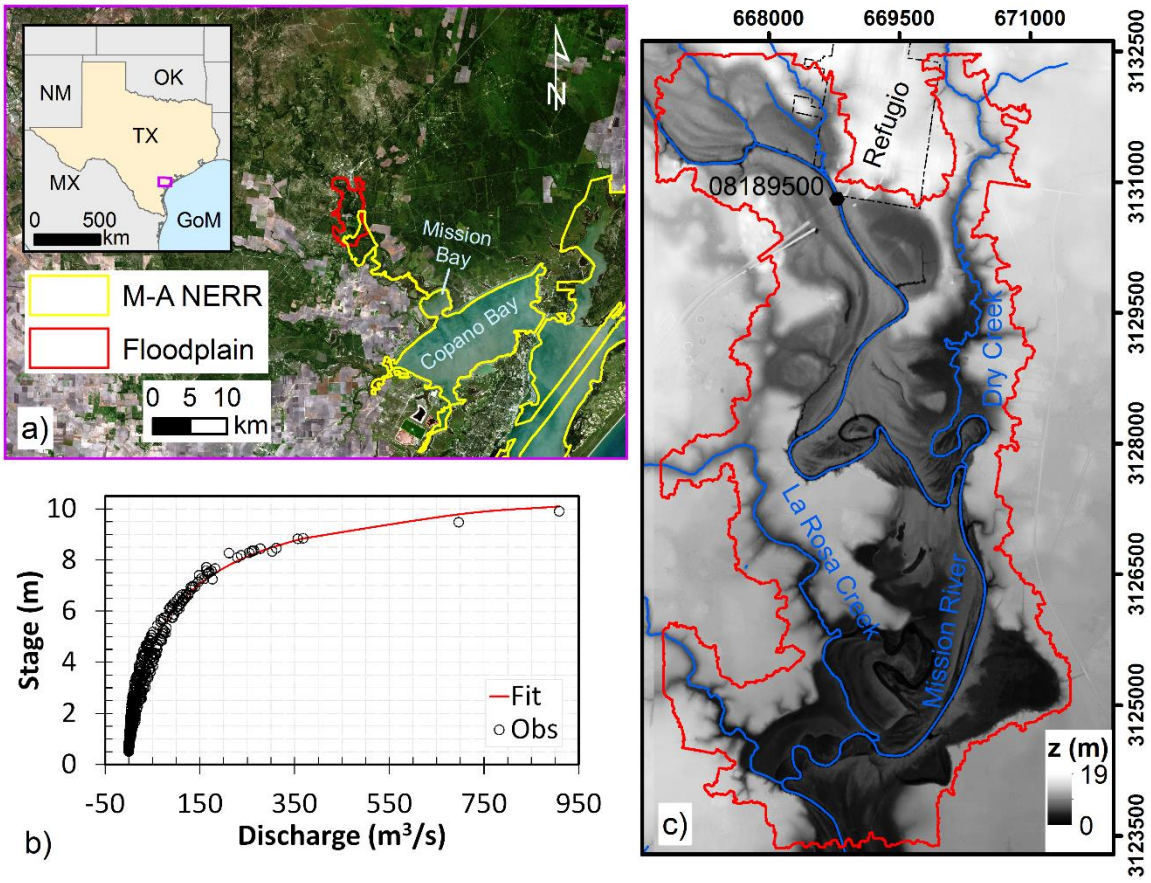

Figure II-1. a) Regional location map of the Mission River Floodplain (red polygon) on the Coastal Bend of Texas (Note M-A NERR = Mission Aransas National Estuarine Research Reserve). B) Rating curve generated using flow records for the years 1995-2014 from U.S. Geological Survey (USGS) gaging station 08189500 (Figure II-1c) on Mission River (Note: Obs indicates observed values and Fit is a fitted logistic equation). c) Location map of the Mission River floodplain (red polygon; horizontal coordinates are in UTM zone-14N). A gridded digital terrain model generated using Federal Emergency Management Agency/Texas Water Development Board point clouds from 2006, streams (blue lines), the USGS gaging station on MR (08189500), and boundary for the Town of Refugio are also included.

The study area has a subhumid-to-semiarid subtropical climate with extreme variability in precipitation (Davis and Smith, 2013, Fulbright et al., 1990, Norwine and John, 2007). Mean daily discharge at the U.S. Geological Survey gaging station below Refugio (Gage ID: 08189500) ranged from 0 to 1903 m^3/s with a mean of 3.4 m^3/s (USGS, 2016). The distribution for annual peak discharge is extremely skewed (Schoenbaechler and Guthrie, 2011), with a range of 1 to 2237 m^3/s. Similarly, the

distribution of stage is also skewed with range of 0.8 to 10.2 m and 1 to 12 m for mean daily and annual peak stage, respectively (USGS, 2016). Published estimates of bankfull conditions occur at the 08189500 gage with a discharge of 107 m^3/s and stage of 6.1 m, but the floodplain widens and the river becomes more sinuous in the downstream direction. This results in high variation of hydraulic and geomorphic conditions that can complicate the application of point-sampled streamflow measurements to other portions of the floodplain (Hudson et al., 2013, Tockner et al., 2000). Moreover, the lower half of the main channel within the study area is influenced by tidal processes (Davis and Smith, 2013, Nelson and Tolan, 2008), that further complicates hydraulic and geomorphic conditions.

Methods

Generation of Stage-Relative Digital Elevation Model

We develop a digital relative elevation model (DREM) to determine the height above or below the river water surface for all portions of the study area. The DREM is essentially a digital terrain model (DTM) without a longitudinal trend from the river. We generate the DREM using a DTM and the methodology from Poole et al. (2002) and Jones et al. (2008). We first generate a DTM of the study area with a 5-m spatial resolution by utilizing topographic LiDAR point clouds, inferred from near infrared light pulses (see Appendix A for the methodology used for the generation of the DTM).

To generate our DREM, we determine the water surface elevation along the main channel by generating transects spaced 5 m apart (i.e., at the resolution of the DTM) along that channel and restrict each transect to the channel banks. Although water

generally absorbs near infrared light, water with movement and turbidity returns a near infrared signal—and LiDAR point elevation. Given that, the minimum elevation value along each transect is assumed to correspond to the water surface elevation and it is assigned to all pixels intersecting a particular transect. We also manually adjust water surface elevation values at each transect to maintain "hydrological correctness." From water surface elevation values throughout the transects, we generate a height with respect to river stage (at time of LiDAR data acquisition) for every location in the study area by generating a raster surface using inverse distance weighted interpolation with parameter values of 4 and 400 for the decay parameter and sample size for each pixel, respectively. This methodology allows areas near transects to have a more localized height-value, while areas far from transects have a more regional value. Finally, we subtract the assigned river-stage value for each pixel from our DTM in order to remove the longitudinal trend in the floodplain surface and generate our DREM (Figure II-2).

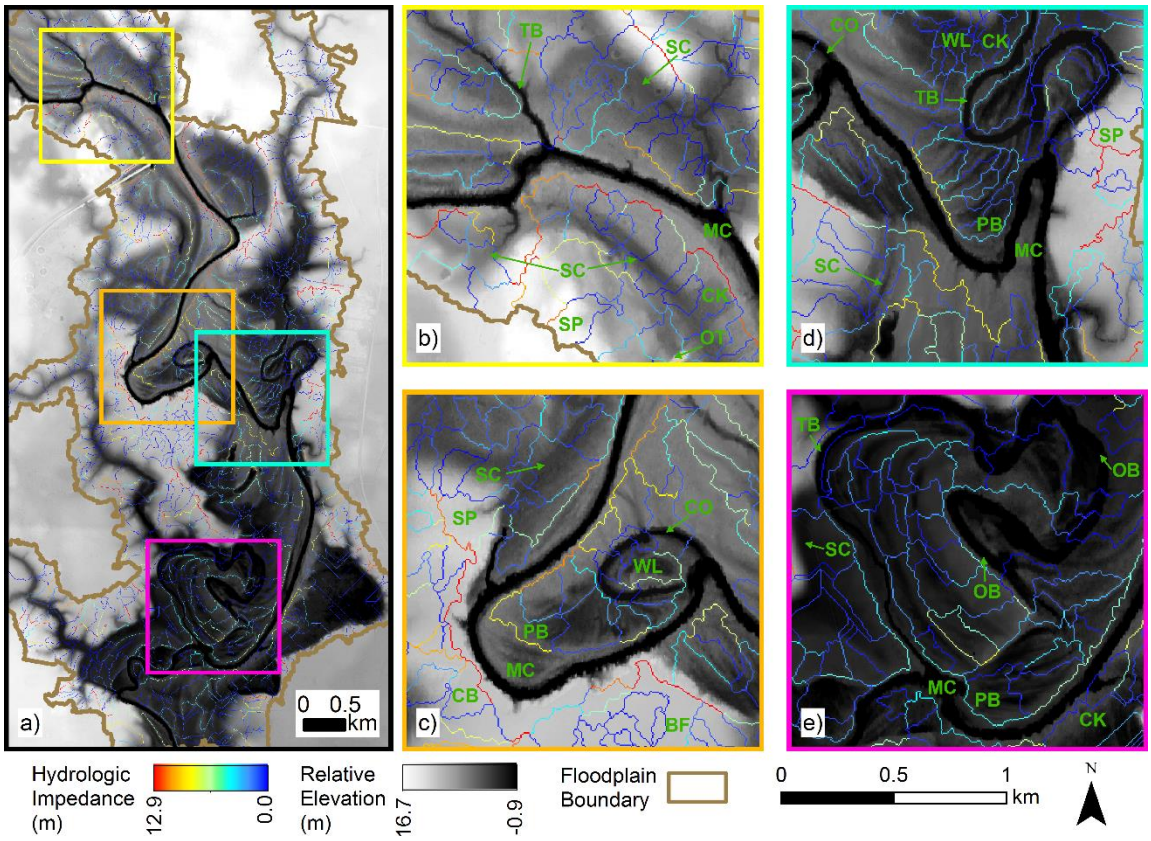

Figure II-2. a) Map of relative elevation above river-stage for the entire study area and hydrologic impedance between hydrologic facets (facets). Each colored square (yellow, orange, cyan, and magenta) depicts the location of the zoomed-in views of the floodplain in b-e. b) Area depicted by yellow square in (a) with facet classes of main channel (MC), secondary channels (SC), tributaries (TB), channel banks (CK), slopes (SP), and other (OT). C) Area depicted by orange square in (a) with the facet classes of MC, SC, SP, point bars (PB), cut banks (CB), cutoff (CO), and bluffs (BF). D) Area depicted by cyan square in (a) with facet classes of MC, SC, CO, TB, WL, CK, and SP. E) Area depicted by magenta square in (a) with facet classes of MC, SC, TB, OB, PB, CK, and oxbow (OB).

Delineation of Hydrologic Facets and Floodplain Boundary

Characterizing flow patterns in a spatial context often relies on digital elevation models with raster cells typically being the basic spatial unit (Heckmann et al., 2015). However, the hydrogeomorphological significance of raster cells has been questioned and has ultimately called for object-based approaches (Gascuel-Odoux et al., 2011, Guzzetti et al., 1999, Heckmann et al., 2015). We use a modified approach from Jones et

al. (2008) and our DREM in order to delineate hydrologic facets (facets hereafter) that are used to divide the study area into patches formed by common hydrogeomorphic properties. Facets are similar to floodplain level catchments in that they represent areas that drain towards a common point/outlet. We are interested in the connectivity between facets caused by a hydrologic connection amongst adjacent facets. A raster-cell based approach would only allow a maximum of eight immediate neighbors with all having the same geometric properties. Our object-based approach allows an individual facet to theoretically have an unlimited number of immediate neighbors with varying geometric properties.

We employ algorithms from the TauDEM Toolbox for ArcGIS (Tarboton and Mohammed, 2013) to generate facets within the study area. First, all depressions (real and artificial) within the DREM that signified internal drainage are "filled" using the standard Fill operation. Second, flow directions and upslope contributing areas are determined with the D8 flow direction algorithm (O'Callaghan and Mark, 1984). We chose the D8 approach because of its reliability and the large degree of functionality that D8 data allows within TauDEM. Third, the drainage network is extracted using the Peucker-Douglas Stream Definition algorithm. This algorithm utilizes a method put forth by Peucker and Douglas (1975) to identify "upwardly curved" pixels that helps depict the location of channels (Tarboton and Ames, 2001). In addition, Peucker-Douglas Stream Definition can incorporate Drop Analysis to objectively define a threshold for upstream contributing area (200 m^2 in this case) that is appropriate for an area while upholding "Horton's laws of drainage network composition" (Tarboton and Ames,

2001). Fourth, the drainage network is used to identify all areas that drain towards the lowest point of a particular channel reach and delineate facets.

We consider only the facets that intersect the Mission River floodplain. To select the appropriate facets, we use a simple thresholding of the DREM to find all areas that have a relative elevation ≤ 7 m (bankfull conditions occur at 6.1 m stage for the 08189500 gage). Areas at and near the Mission River main channel create a large patch that would be inundated with a uniform 7 m rise in the water surface elevation and we select all facets that intersect this patch. Due to a lack of flow records, we do not explicitly considered flows from three tributaries in the floodplain in our inundation estimates, but these tributaries allow the floodplain to extend in the upstream direction for each tributary. Not all facets are inundated using the ≤ 7 m criterion, but we also included non-inundated facets in our floodplain if they are completely surrounded by inundated facets. We also include non-inundated facets that intersect the floodplain edge that was inferred by manually identifying linear features beyond the main channel banks with steep slopes dipping perpendicularly to the general direction of flow.

Determination of Hydrologic Impedance

Here we assume that areas within a facet are always connected and that surface-water connectivity induced by river flooding follows the flood pulse concept (Junk et al., 1989, Tockner et al., 2000) in that water from lower areas (i.e. the river) moves to higher areas throughout the floodplain when a flood pulse occurs. Surface-water connectivity between two adjacent facets occurs when rising surface water levels within the topographically lower facet rises to the point where water can breach the boundary

between the two respective facets. Hydrologic impedance (*HI*) is used here as a term to describe the factor(s) controlling connectivity between a set of facets. Low *HI* promotes higher surface-water connectivity between facets, while high *HI* inhibits surface-water connectivity (Jones et al., 2008, Kondolf et al., 2006, Pringle, 2003). We quantify *HI* using Eq. II-1 from Jones et al. (2008) (also Eq. II-1 below) —which is a measure of the minimum water elevation it would take for the divide between two adjacent facets to be breached by a rising water level.

$$HI = Delv_{min} - Min(Facet_{elv,a}, Facet_{elv,b}) \quad \text{(Eq. II-1)}$$

$Delv_{min}$ is the minimum elevation along the facet divide and $Min(Facet_{elv,a}, Facet_{elv,b})$ is the minimum elevation value within facets a and b, respectively. $Min(Facet_{elv,a}, Facet_{elv,b})$ will be the outlet of the topographically lower facet and $Delv_{min}$ will be at the higher facet's outlet. The drainage network that forms a conduit of flow in the downstream direction also becomes the conduit for backwater flooding and allows flood waters to extend outward into the floodplain without the necessity of overbank flows.

Classification of Hydrologic Surface Connectivity with Stage

We classify a facet as connected by surface water (or connected) when rising surface waters breach the facet divide. The facet containing the main channel is considered to always be connected and the number of facets classified as connected will increase as river stage rises. By mapping *HI* within the floodplain (Figure II-2) and systematically thresholding the DREM, we determine the river stage needed for the divide between adjacent facets to be breached as follows. When a connected facet shares

a boundary with multiple facets that are not connected by surface water (or not-connected), the facet with the lowest *HI* with respect to the connected facet will be the first to be connected if river stage continues to rise. For example, the facets with the lowest *HI* with respect to the main channel facet are the first to be breached by the initial rise in river stage when a flood pulse occurs.

We use daily streamflow records for the 08189500 gage from Jul-1939 through Dec-2016 to characterize the flow regime. These historical flows inform our determination of the river stage that would cause facets to become connected to the main channel. Our design simulates an incremental increase in river stage at 10 cm intervals from 1.4 to 9.4 m, numbering 80 realizations, with flood water spreading into the floodplain using a backwater and flood pulse mechanism. The long-term mean river stage is 1.2 m, but we initiate our DREM thresholding at 1.4 m, which is the mean river stage during acquisition of the LiDAR data used to generate the DREM. In addition, we determine the return period for the flows that initiate connectivity between a respective facet and the main channel using river-stage values, a fitted rating-curve (Figure II-1b), and a Generalized Extreme Value distribution (see Appendix A for the methodology used in the determination of return periods).

Graph Conceptualization

We employ graph/network theory to quantify connectivity. Detailed descriptions of the theory can be found in Harary (1969), Chartrand (1977), and Chartrand and Lesniak (1986). For our graph formulation, vertices represent facets and the existence of an edge between any two vertices depicts a connection between the respective facets. To

maintain the geospatial context of the floodplain within our graphs, we conduct the determination of vertices and connections/edges within a GIS environment (ArcGIS 10.2). Specifically, two facets (vertices) need to share a boundary/divide and contain the same classification (connected or not-connected) in order for there to be an edge/link between the two vertices (facets) within the graph. Our analysis is mostly concerned with how connectivity varies within the floodplain as a result of rising surface water, but we are also interested in how the connections between not-connected facets changes with a rising river stage; thus we develop graphs determining connections between both classifications, connected and not-connected, of facets for each of our simulated river stage values.

The facet classification scheme utilized in our simulation of a rising river stage implicitly imposes a directed nature to our graph analysis (from connected to not-connected). This is because a rising river stage will transport water (and other materials such as sediment, nutrients, and biota) from topographically lower areas to higher areas. Thus, in our connectivity analysis, we use directed graphs (or digraphs). We determine the directionality by finding the minimum relative elevation within each facet and directing the connection from these points to neighboring facets that have a higher relative elevation.

We also incorporate *HI* into our graph conceptualization by using the *HI* of a particular facet with all adjacent facets in order to apply edge weights to our digraphs. Our edge weighting (w_i) varies between 0 and 100; and is determined as

$$w_i = \begin{cases} 0, & \text{if } n=0 \\ 100, & \text{if } n=1 \\ \left(1 - \dfrac{HI_i}{\dfrac{\sum_{i=1}^{n} HI_i}{n-1}}\right) \times 100, & \text{otherwise} \end{cases} \qquad (Eq.\ II\text{-}2)$$

where n is the number of adjacent facets with the same classification as the facet from which the directed edge will originate, HI_i is the hydrologic impedance between the two facets that will be connected with the directed edge, and $\sum_{i=1}^{n} HI_i$ is the summation of hydrologic impedance values for the set of adjacent facets with the same classification. The facet that has the lowest *HI* with respect to the facet from which the directed edge will originate will have the highest w_i. These weights ultimately allow the magnitude of individual connections amongst facets to be incorporated into the quantification of overall connectivity.

Quantification of Graph Connectivity

We calculate six graph-theoretical metrics (Table II-1) and examine their variations as a function of river stage. As we are concerned with surface-water connectivity within the floodplain as a whole, we compute all of our connectivity metrics at the graph level. Graph-level connectivity is typically analyzed using simple metrics that rely on topological properties and Table II-1 shows the ones we use here.

Table II-1. Graph theoretical metrics of connectivity and associated attributes.

Metric	Definition	Application Domain	Type of Information	Source
Graph Order (*N*)	Number of vertices (i.e., facets) in a graph.	Ecological	Indicator on the number or dominance of particular habitat patches (or facets) within an area.	Fagan (2002); Jordán et al. (2003); Marcot and Chinn (1982); Rayfield et al. (2011); and Treml et al. (2008)
Mean Node Degree $\overline{d}$	$\overline{d} = \frac{d}{N}$ *d* is vertex degree; *N* is number of vertices	Ecological	Indicator of mean habitat accessibility.	Cantwell and Forman (1993); Ferrari et al. (2006); Forman (1995); Jordán et al. (2003); Kupfer et al. (2014); Marcot and Chinn (1982); and Rayfield et al. (2011)
		Geomorphic	Indicator on the accessibility to the main conduits of material flow (main, tributary, and secondary channels).	
Graph Diameter (D)	Maximum geodesic distance in a graph	Ecological	Indicator of the compactness of a graph based on maximum distance between any two patches (or facets).	Forman (1995); Jordán (2001); Jordán et al. (2003); Rayfield et al. (2011); Phillips et al. (2015); and Ricotta et al. (2000)
S-metric (*S(g)*)	See Li et al. (2005) for description on how to compute.	Geomorphic	Measure of "hub-like" connectivity that is an indicator of scale-properties in graphs	Heckmann et al. (2015); Li et al. (2005); and Phillips et al. (2015)
Spectral Radius (λ_1)	Largest eigenvalue of the adjacency matrix of the graph (see Biggs (1993) for description of algebraic graph theory).	Geomorphic	Indicator of complexity in system response to external perturbations and the threshold for coherent/incoherent behavior amongst system elements.	Heckmann et al. (2015); Logofet (2013); Phillips (2011); Phillips et al. (2015); Restrepo et al. (2006); Restrepo et al. (2007); Schreiber and Hastings (1995); Tinkler (1972); and Yuan et al. (2008)
Algebraic Connectivity ($\lambda(A)_{N-1}$)	The second-smallest eigenvalue of the Laplacian matrix for the graph.	Geomorphic	Indicator of the synchronizability of the system being modeled (i.e., synchronized transitions from one connection class to another).	Biggs (1993); Duan et al. (2009); Heckmann et al. (2015); Phillips (2011); Phillips (2012); Phillips (2014); and Phillips et al. (2015)

Geometric Influence on Connectivity

Our graph analysis relies on spatially explicit graphs to model the connection between adjacent facets. Geometric and spatial relationships between facets can influence the values of our indicators described in *Quantification of Graph Connectivity*; thus we compute six different geometric variables for each facet (Table II-2) and determine how they influence connectivity for each of our simulated river stages. We plot the mean vertex degree ($\bar{d}$) for both the connected and not-connected facets as a function of river stage. We chose mean vertex degree, which is one the most widely used measures of graph connectivity, due to its conceptual and operational simplicity (Rayfield et al., 2011). The distribution of values for each geometric variable is used to divide the facets into four distinct groups using quantiles (see Table II-3 of Supplemental Material for variable value ranges and sample size within each quantile). The geometric variables and how we use them is outlined in Table II-2.

Table II-2. Geometric variables used in the geometric and spatial assessment of floodplain facets.

Geometric Variable	Description
Facet area (A_F)	Determines how facet size influences floodplain connectivity.
Elongatedness, ratio between the minor and major axes for the minimum bounding ellipse ($Axis_{min}$ /$Axis_{maj}$)	Determines how facet shape influences floodplain connectivity (values closer to 0 indicate more elongation and values close to 1 indicate more circular or compact).
Mean distance from the geometric centroid of a facet to all geometric centroids of facets within 3000 m ($\overline{dist_F}$)	Determines how spatial clustering influences floodplain connectivity (smaller values indicate more clustering).
Mean slope for terrain within facet ($\overline{slp_F}$)	Indicator of the types of landforms that can be found within and near groups of facets (banks and levees have steeper slopes, while backswamps and bluffs are flatter).
Length of delineated channel (L_{ch})	Indicator of how much influence the internal drainage network has a facet's connectivity.
Minimum distance to main channel ($\overline{dist_{mc}}$)	Determines how straight-line distance to main channel can influence floodplain connectivity.

Results

Generation of Stage Relative Digital Elevation Model

Relative elevation ranges from -0.9 to 16.7 m with a mean of 8.4 m for our DREM (Figure II-2a). The variability in DREM values increases in the downstream direction. DREM patterns are similar to the source DTM and it still allows the numerous floodplain features (e.g., main channel, tributaries, secondary channel, and oxbows) to be visually recognized. Facets containing some of these floodplain features are shown in Figures II-2b – II-2e. We classify each facet by the dominant landform it contains and present descriptive statistics on the distribution of relative elevation for the major landforms (Figure II-3). Bluffs, other, and slopes have the highest median relative elevation while oxbows and wetlands have the lowest mean relative elevation. In terms of variability in relative elevation, the main channel and tributaries have the highest while bluffs and oxbows have the lowest variability.

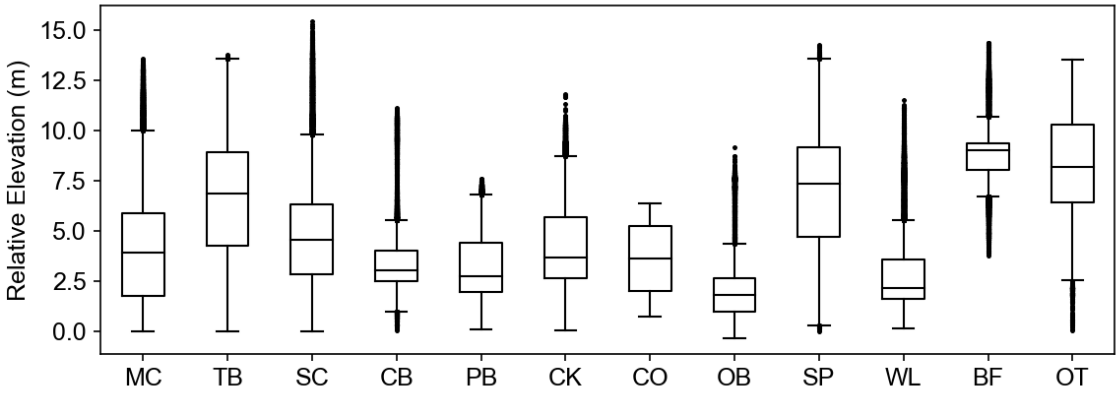

Figure II-3. Box-and-whiskers plots of relative elevation for the dominant floodplain landform within hydrological facets. (Note: MC = main channel; TB = tributary; SC = secondary channel; CB = cut bank; PB = point bar; CK = channel banks (include channel banks that are not a cut bank or point bar); CO = cutoff; OB = oxbow; SP = slope (facets that slope downhill but doesn't contain an obvious channel such ass floodplain edges and bluff flanks); WL = wetland (includes backswamps, marshes, forested, and other types of floodplain/riparian wetland); BF = bluff; other = OT (features that could not be classified as a landform; possibly due to human modification)).

Delineation of Hydrologic Facets and Floodplain

We delineate an initial set of 2241 facets for the entire study area using the DREM. These initial facets range in areal coverage from 0.02 to 17.55 hectares (hec) with a mean area of 1.88 hec, but *HI* between many of these initial facets is < 1mm. Applying a threshold to our DREM of 1 mm aggregates many of our initial facets and yields a final set of 939 facets. This new set of facets ranges in size from 0.02 to 341.97 hec with a mean area of 2.91 hec (Figure II-4a). Statistically significant ($p < 0.01$) spatial clusters of facets with low relief are found in more central portions of the floodplain (Figures II-2c – II2e, II-3). Moreover, clusters ($p < 0.01$) of high relief facets are found in upper portions of the study area (Figures II-2b, II-4). However, a large very flat patch of wetland area east of the natural levee (eastern bank of main channel in south-central

portions) creates ambiguous flow directions from the D8 algorithm and some facets in this area have spurious linear boundaries (Figure II-4a).

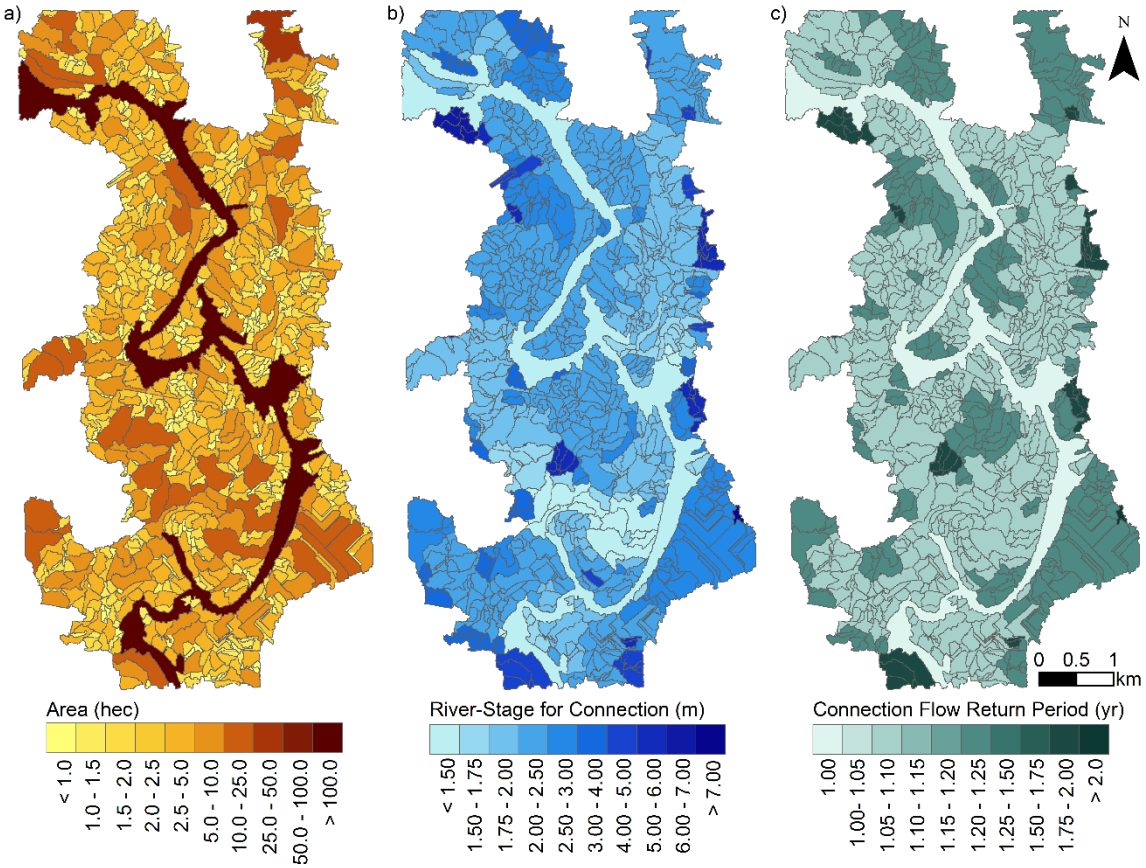

Figure II-4. a) Area occupied by each of the total of 939 hydrologic facets (facets) delineated within the Mission River floodplain. Facets are delineated using the digital relative elevation model (DREM). B) River stage needed for each facet to be connected to the main channel. C) Return period for the river stage needed for connection between a particular facet and the main channel. Return period determined using the fitted rating curve function (Figure 1b) and a Generalized Extreme Value distribution that is fitted to the peak flow statistics for the USGS Gage 08189500.

Determination of Hydrologic Impedance

HI ranged from ~0 to 12.9 m with a mean of 1.9 m (Figure 2a). Facets with low-lying floodplain features (i.e., secondary channels, oxbow lakes, meander scars, and back swamps) have lower *HI* values with their neighbors, while facets with upland features (i.e., natural levees, bluffs, and the floodplain edge) have higher *HI* values. The

HI relationship that the main channel facet has with its immediate neighbors highlights the significance of low spots along the main channel banks (Figures 2b-e) that ultimately allow high streamflows to leave the main channel and spread into the floodplain. Moreover, the spatial relations in *HI* present the importance of low-lying features to floodplain connectivity (especially secondary channels, oxbow lakes, and tributaries) because these features are the first to become connected to the river when surface water levels begin to rise.

Classification of Connectivity with Stage

Topographic features ultimately control similarities in river-stage values needed for facets to become connected to the main channel (Figure II-4b). The streamflows needed for the majority of facets to become connected have a return period of < 1.5 years (Figure II-4c). Facets on the edge of the floodplain or those associated with high-standing bluffs are the only ones that require streamflows with return periods > 2.0 years (Figure II-4c).

The number and proportion of connected facets increases nonlinearly as river stage rises (Figures II-4a – II-4b). Surface-water connectivity within the floodplain increases abruptly as river stage rises from 1.4 to 2.9 m (Figures II-5a – 11-5f); than the rate of increase in connectivity becomes more modest as river stage rises from 2.9 to 6.0 m (Figures II-5a – II-5b, II-5g - II-5h). The rate of change for surface-water connectivity becomes virtually zero for river-stage values from 6.0 to 9.4 m because there are only a handful of facets still classified as not-connected at that point (Figures II-5a - II-5b, II-

4h). Most of the floodplain is classified as not-connected for river-stage values of < 2.0 m; and connected facets dominate at higher river-stage values (Figure II-5).

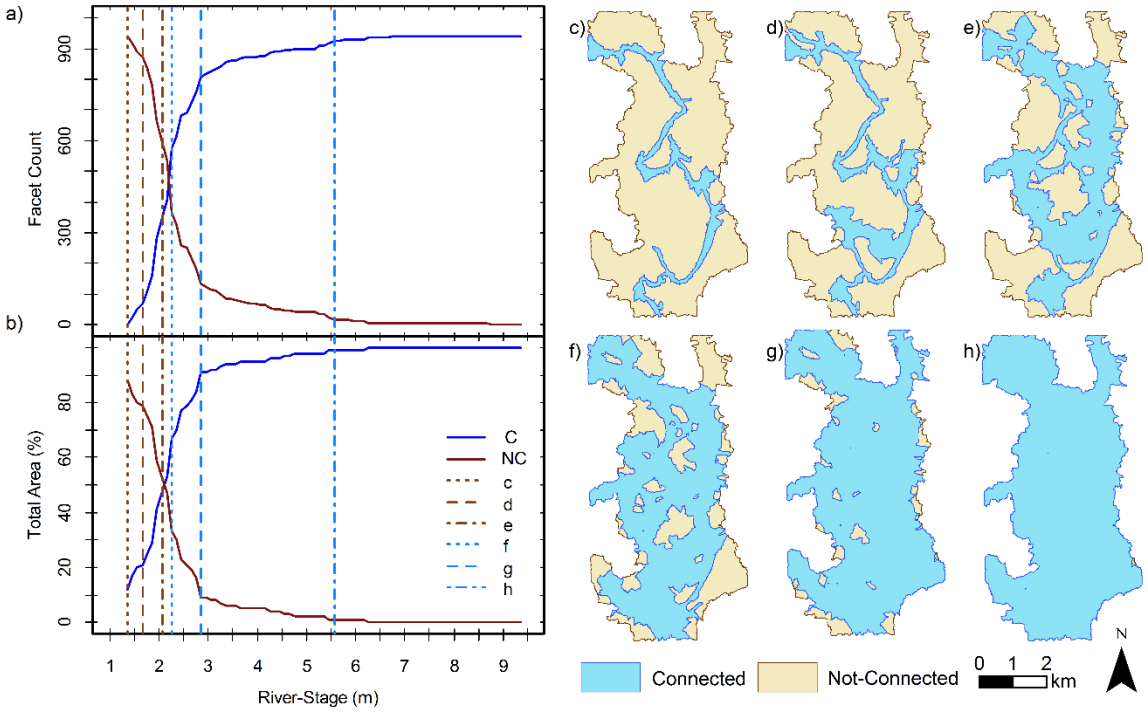

Figure II-5. Counts (a) of facets and percentage (b) of total study area classified as connected (C) or not-connected (NC) to the main channel for river-stage values from 0.81-11.61 m. Vertical lines in (a) and (b) indicate the river-stage values (0.81, 2.61, 4.21, 4.91, 5.81, and 8.21 m) depicted in (c), (d), I, (f), (g), and (h), respectively. The maroon vertical lines in (a) and (b) provide examples of streamflows where not-connected conditions dominate the floodplain (c, d, and e), while the light blue vertical lines highlight some streamflows where connected is dominant (f, g, and h).

In a spatial context, the classification of connected facets generally moves outwards/laterally from the main channel facet as river stage rises in a fashion similar to a flood pulse (Figures 5c-5h). Facets that contain low-lying features such as oxbow lakes and meander cutoffs are the first to become classified as connected. Facets that contain tributaries and secondary channels generally are the next ones to become connected and these features will ultimately be the conveyances of flood-waters throughout the floodplain using a backwater flooding mechanism. The influence from tributaries and

secondary channels also creates patterns that allow several "islands" to develop containing a number of facets. These island-facets are mostly associated with bluffs and natural levees and they provide locations within the floodplain that only become connected when flood-waters are significantly high and have the potential to create "refugia" for biota that are less flood-tolerant.

Quantification of Graph Connectivity

Graph order (*N)*, mean vertex degree ($\bar{d}$), and the gamma index (γ) show that connectivity among the facets for the connected class increase dramatically when river stage rises from 1.4 to 2.9 m (Figure 6). *N* exhibits a steady but modest increase until ~6.0 m and the latter two connectivity measures ($\bar{d}$ and γ*)* for the connected class remain fairly constant for higher river-stage values (Figure 6).

S(*g*) increases dramatically for the connected class at river-stage values from 1.4 to 2.9 m (Figure 6) and continues to increase from 2.9 to 6.1 m, but at a more modest rate. A small and sudden drop in *S(g)* values occurs at 6.2 m and then it remains constant for greater values. λ_1 is similar to the aforementioned measures with a dramatic increase river-stage values of 1.4 to 2.9 m and consistent values for higher values of river stage, but the values show more of an oscillatory behavior throughout the simulated stage values. $\lambda(A)_{N-1}$ exhibits the most different values amongst all the measures in that it initially increases dramatically, but then it drops quickly in an oscillatory fashion until it retains a constant value for river-stage values > 2.3 m (Figure 6).

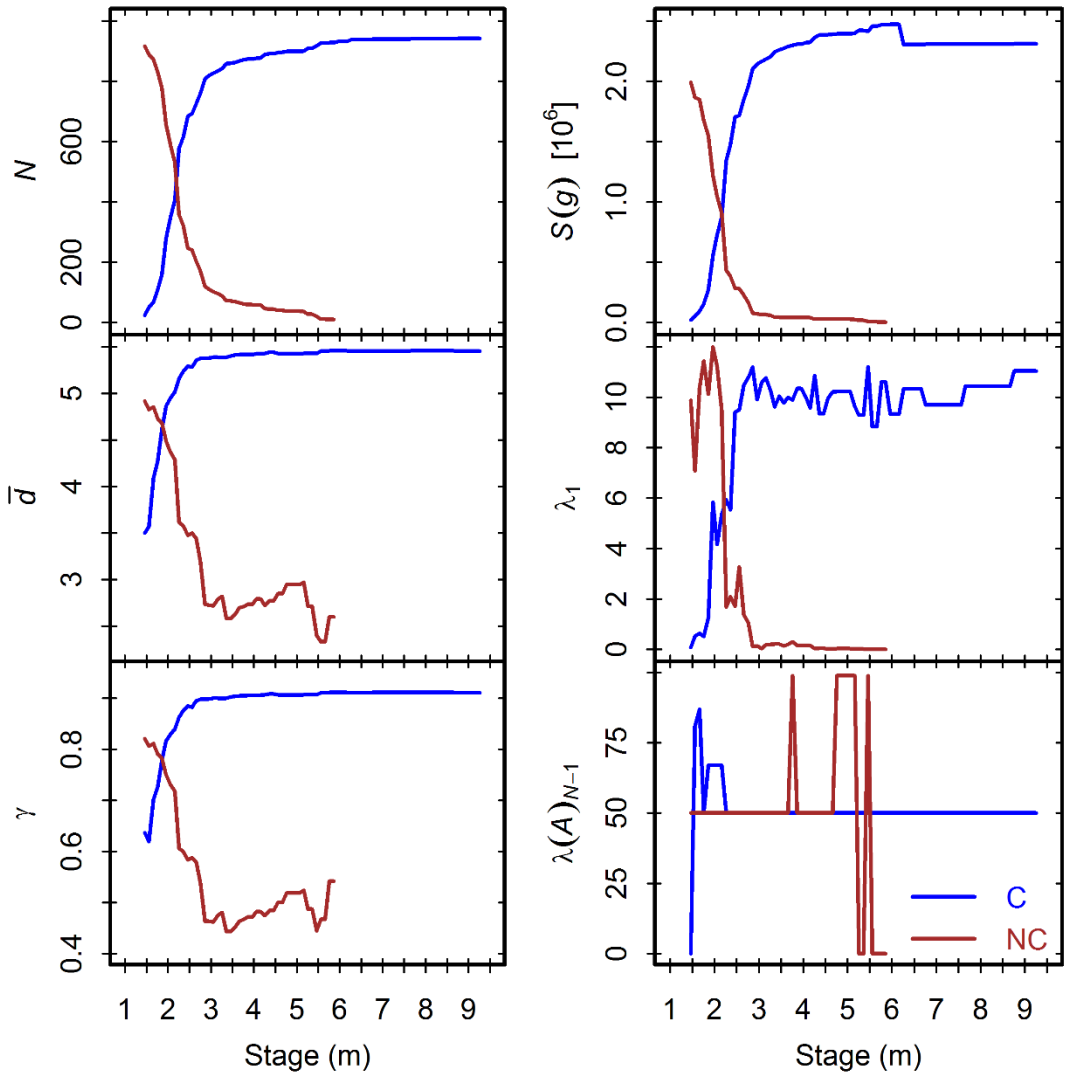

Figure II-6. Graph/network connectivity metrics for the connected (C) and not-connected (NC) digraphs plotted as a function of river-stage. *N* is the number of hydrologic facets (facets)/vertices within each network, $\overline{d}$ is the mean vertex degree for each of the networks, *γ* is the gamma-index for each network and it is similar to $\overline{d}$, *S(g)* is the S-metric that is used to describe hub-like connectivity within each network, λ_1 is the spectral radius of each network that is used to describe network level complexity, and $\lambda(A)_{N-1}$ is the algebraic connectivity of each network that is used to describe synchronization in the network.

As for the facets within the not-connected class, the six measures could only be computed for river-stage values from 1.4 to 5.9 m because the only remaining facets within the not-connected class are disconnected at greater river stages. This negates the

possibility of computing our chosen measures. Most of the trends roughly mirror the values from the facets within the connected class. For example, N, $\overline{d}$, and γ experience rapid declines in their values for river stages from 1.4 to 2.9 m. N continues the mirrored trend with a gradual decline until a river-stage of 5.9 m. $\overline{d}$ and γ exhibit more of an oscillatory behavior that tends to hover around the same value. Similar to N, the $S(g)$ curve also follows a mirrored trend. λ_1 also oscillates, but values are greater for river stages from 2.0 to 2.5 m than the initial values. The peak in λ_1 is followed by a sharp decline with some small oscillations that asymptotically approach zero. Once again, $\lambda(A)_{N-1}$ exhibits unique behavior because values are constant until a river-stage of 3.6 m where large oscillations occur that ultimately result in the values ending at zero.

Geometric Influence on Connectivity

We plot the mean vertex degree $\overline{d}$ for facets as a function of river stage with six geometric properties for the connected and not-connected classes (Figure 7). Larger areas tend to have higher connectivity scores than smaller areas for all of the simulated river-stage values regardless of the connectivity class (Figure 7a). This is to be expected because the more area that a facet occupies, the greater the opportunity for it to have neighbors for it to be connected with. Connectivity scores are similar amongst all quantile groupings and classes for $Axis_{min}/Axis_{maj}$ for river-stage values of < 2.0 m (Figure 7b). Facets that are very elongated in shape, as opposed to more circular or compact, exhibit higher connectivity for the connected class at river stages of > 2.0 m. Although this is probably due to the fact that the main channel facet, which has by far the highest vertex degree (d) value, is part of the most elongated grouping. Thus

elongation in facet shape may not have a very strong influence on connectivity because the scores for the other groupings are similar and there are no obvious spatial patterns in the distribution of quantile groups.

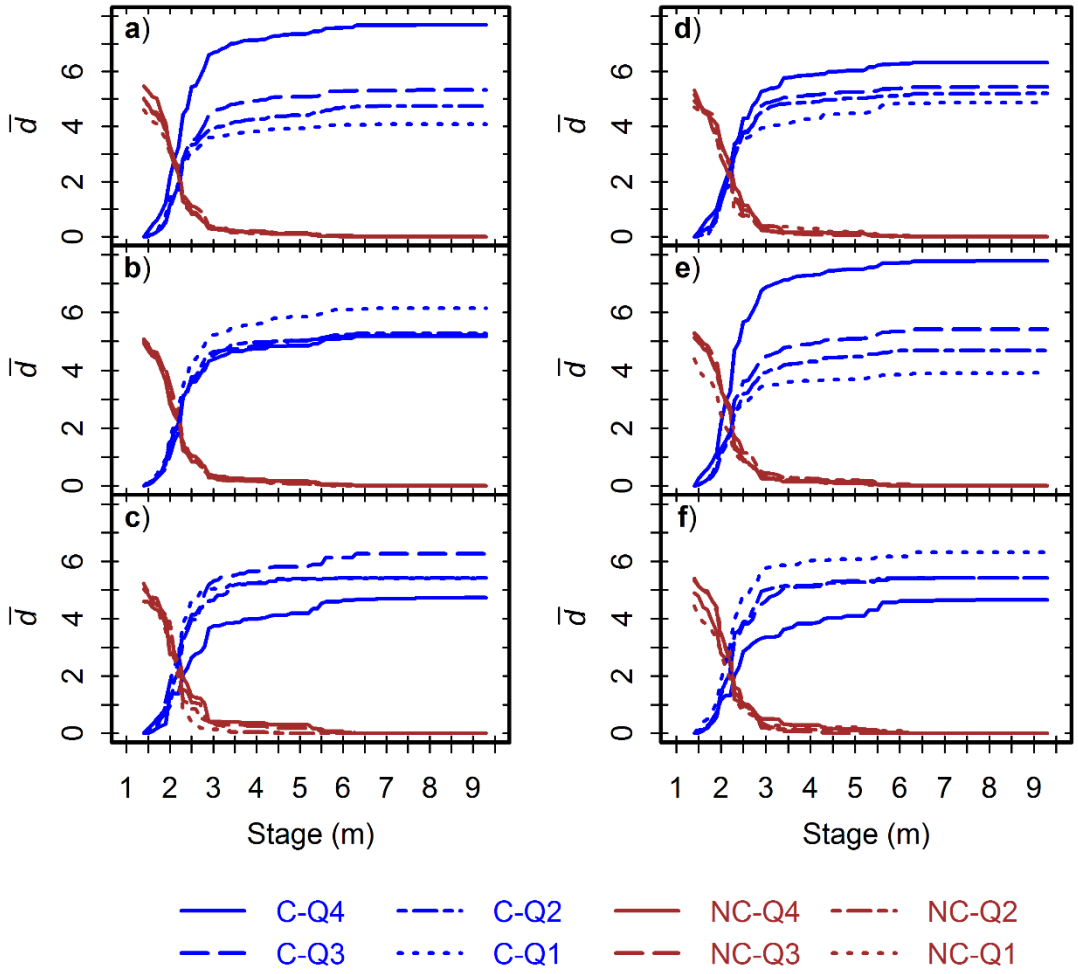

Figure II-7. Mean vertex degree for hydrologic facets (facets) plotted as a function of river stage with six geometric properties within and between facets for the connected (C) and not-connected (NC) classes. facets are divided into quantiles. The geometric properties include: a) facet area; b) ratio between minor and major axes ($Axis_{min}$ /$Axis_{maj}$) for the minimum bounding ellipse for each respective facet; c) mean distance from one facet to all others within a 3000 m buffer; d) mean facet slope; e) delineated channel length within each respective facet; f) minimum distance to the main channel facet.

Connectivity scores are similar amongst all groupings and classes for the mean distance between facet centroids for river-stage values of < 2.0 m (Figure II-7c). The

scores for the connected class are lowest for the quantile grouping with the greatest mean distance between facet centroids for river-stage values > 2.0 m. In a related fashion, this grouping maintains the highest connectivity scores for the not-connected class because these facets are generally found on the edges of the floodplain. The grouping with the second largest mean distances between facet centroids has the highest connectivity scores and this is because it includes the main channel facet and facets with other floodplain features that promote connectivity (tributaries, secondary channels, and oxbow lakes). The two other groupings (Q2 and Q3) have similar connectivity scores because they are found in the same portions of the floodplain and they contain a number of connectivity promoting floodplain features themselves.

Connectivity scores do not differ amongst the facet slope groupings within each class for river-stage values of < 2.5 m (Figure II-7d). The scores are similar for all river-stage values amongst the slope groupings for the not-connected class. For river-stage values > 2.5 m, facet groupings with the higher mean slope have higher connectivity scores in the connected class because the higher mean slopes indicate that the facets have floodplain features that promote connectivity. An example is the grouping with the highest mean slope because it contains the main channel and tributary facets.

Connectivity scores amongst the groupings within each class (connected and not-connected) for the delineated length of channel within each facet (Figure II-7e) are very similar to the scores from facet area (Figure II-7a). At river-stage values < 2.0 m, connectivity scores are similar amongst the distance to the main channel facet groupings for the connected class (Figure II-7f); while the connected class have higher connectivity

scores for groupings with greater distances to the main channel facet. $\bar{d}$ is similar amongst main channel distance groupings for not-connected at river-stage values > 2.0 m; while groupings of connected with shorter distances to the main channel facet having higher $\bar{d}$ values. This last portion is expected because water from a rising river stage will move from the river outward along the preferential flow path.

The dramatic initial increase in connectivity is mostly driven by the large size, positioning, and elongated shape of the main channel facet (longitudinally spans entire study area and centrally placed). These geometrical properties allow the main channel facet to have a much larger number of neighbors than any other facet and thus increase overall connectivity and complexity. Moreover, a positive relationship is found between and facet area, mean slope within facets, delineated channel length, and elongation (inverse of $Axis_{min}/Axis_{maj}$) (Figure II-7). This indicates that large facets that contain major components of the floodplain drainage system are significant with regard to connectivity within the floodplain. On the other hand, a negative relationship between and distance to the main channel facet is also found and indicates that the river is the dominant control of connectivity within the floodplain.

Discussion

Mapping of *HI* allows us to determine the spatial patterns of connectivity by systematically thresholding the DREM and comparing it to *HI* between facets. Thresholding algorithms that operate on DEMs and similar types of data provide an efficient means for characterizing inundation from flood events (Wang et al., 2002). Bankfull conditions for the 08189500 gaging station have been specified at a river-stage

of ~6 m, but the majority of the floodplain becomes connected to the river at river-stage values below 3 m. Notwithstanding issues concerning the application of gaging station data to other portions of a channel reach (Hudson et al. (2013); Tockner et al. (2000)), our results agree with previous work in that widespread floodplain inundation and connectivity occur below bankfull conditions for lowland riverine environments due to low spots along the channel banks, abandoned channels, and confluences with tributaries/secondary channels (Hudson et al., 2013, Kupfer et al., 2014, Meitzen et al., 2013, Tockner et al., 2000). These sub-bankfull flows have been termed "expansion processes" and they are critical components of river-floodplain systems (Tockner et al., 2000). Flows that initiate expansion processes occur more frequently than bankfull flows and this ultimately increases river-floodplain exchange opportunities.

The periodic connection between a river and floodplain features (e.g., oxbow lakes, backswamps, meander scars) is a major driver in nutrient dynamics (Schramm et al., 2009), riparian vegetation patterns (Bornette and Puijalon, 2011, Davis and Smith, 2013), fish food-web dynamics (Robertson et al., 2008), and inter-habitat mobility of fish and aquatic insects (Ishiyama et al., 2014). Importantly, habitat connectivity has been shown to be a key factor in ecosystem health (Urban et al., 2009). Connectivity amongst components of the system being studied is a core research theme that the fields of geomorphology and ecology hold in common (Wohl et al., 2014). Our results indicate that connectivity and complexity increase nonlinearly at the graph/landscape level (Figure 6). Similar results of nonlinear increases in surface-water connectivity with increasing streamflows have been reported in other lowland floodplain/wetland systems

(e.g., Bishop-Taylor et al. (2015); Ishiyama et al. (2014); Kupfer et al. (2014)). Therefore, surface-water connectivity can serve as a useful proxy for species richness within floodplain/wetland environments (Ishiyama et al., 2014).

Our graph representation of the river-floodplain system exhibits some of the characteristics of a scale-free graph/network. Among the properties of scale-free graphs, two can be related to our graphs: (1) a scale-free graph can be created or modified by any process, but preferential attachment to relatively high degree vertices is the dominant process; and (2) scale-free networks contain highly-connected vertices (i.e., hubs) that maintain graph-level connectivity, and this connectivity is resilient to most random disconnections amongst vertices, but also highly sensitive to disconnections of hub-like vertices (Li et al., 2005). The first property indicates that vertices (facets in our case) are more likely to become connected to vertices that are already connected to many other vertices. Under our framework, a large proportion of the increases in connectivity are due to an increasing number of connections with the facets containing the river and other low-lying floodplain features because of their high neighbor count. Thus these types of facets will ultimately be the drivers of increases in spatial connectivity. The second scale-free graph property indicates that overall system connectivity is robust because the majority of vertices are sparsely connected. This indicates that the odds of most of the graph becoming disconnected when a vertex is removed at random are low because there are relatively few hubs. However, graph-level connectivity is also vulnerable to disconnections of one or more hub-like vertices. For example, the construction of levees within the floodplain can disconnect the river from the remainder

of the floodplain and dramatically diminish the overall connectivity of the river-floodplain system. A rich and diverse theoretical basis for understanding interactions within natural and man-made systems through the use of scale-free graphs has been developed in recent decades (Li et al., 2005); and this knowledge-base can help further the basic understanding and management of lowland riverine environments. Therefore, we propose that more research is needed to determine to what extent the drainage patterns of lowland riverine floodplains can be described using a scale-free graph perspective.

Our measure of complexity (λ_1) experiences a dramatic initial increase for the connected class at river-stage values below 3 m and more "stable/plateaued" complexity at higher river stages. This is important because the level of sensitivity to external forcings is directly related to the river flows and the associated floodplain connectivity. For example, if a pollutant is introduced somewhere within the floodplain, its propagation will depend on the river stage that determines the surface-water connection and the hydrogeomorphic relationship of the point of introduction with other parts of the floodplain. λ_1 has also been shown to have a relationship with the onset of macro-level synchronization (Restrepo et al., 2006); which is a graph-level state that occurs when the components of a complex system are operating in unison (Mosekilde et al., 2002). When the vertices of a system are allowed to freely oscillate between states (connected and not-connected in our case), incoherent behavior occurs when numerous nodes are experiencing a phase transition that causes a lack of synchronization (Restrepo et al., 2006). Within our conceptualization, incoherent behavior will cause our measure of

synchronization ($\lambda(A)_{N-1}$) to oscillate; and this occurs for the connected class at river-stage values < 2.5 m (Figure 5). $\lambda(A)_{N-1}$ for the connected class does not oscillate at river-stage values of > 2.5 m and this is the point where λ_1 begins to level-off. Thus, we can assume that the connected components are in a coupled/coherent state. An understanding of when synchronization occurs can be useful in the control/management of complex systems (Kapitaniak, 1996, Restrepo et al., 2006). For example, there have been growing interests in deliberate reservoir releases that are designed to mimic flood pulses that establish ecologically significant river-floodplain connectivity (Galat and Lipkin, 2000, Poff, 2014, Richter and Thomas, 2007). Implications associated with hazards and water supplies can make these types of river management strategies contentious, but analyses of complexity and synchronization can help identify the minimum flow needed in order for the downstream river-floodplain system to reach the desired macro-level state of coherence. These types of analyses ultimately serve to maximize the benefits from these reservoir releases while also minimizing the costs (such as those due to flood damage and loss of water supplies).

Other types of management strategies and/or restoration for river-floodplain systems can be informed from analyses similar to ours. In fact, the establishment of protected areas that include river reaches is an important strategy for the conservation of freshwater biodiversity and resources (Dudgeon et al., 2006, Pringle, 2001, Saunders et al., 2002). Protecting the most critical locations with regard to the river-floodplain ecosystem from human-induced surface-water disconnection will be an important management objective for riverine management moving into the future (Tockner and

Stanford, 2002). On the other hand, a common restoration practice is reconnecting the main channel of a river with its floodplain by constructing side/secondary channels (Buijse et al., 2002, Tockner et al., 2010). An approach similar to the one we present here can help inform the locations already suited for the establishment of new channels that will promote the desired level of river-floodplain connectivity. For example, establishing a river connection with portions of the floodplain that were not previously connected essentially involves merging two drainage networks. A graph theoretical approach can be useful in finding optimum locations within an existing network that will promote the most efficient exchange of information (or energy, matter, and biota in this example) between the two networks in question (Taylor and Restrepo, 2011).

Our approach also highlights a number of local and regional implications for the Mission River. The composition of vegetation within the Mission River floodplain was investigated by Davis and Smith (2013). They found that mid- to late-successional species are the most dominant vegetation type within the floodplain community. This indicates that Mission River is characterized by an infrequent or low-magnitude flood regime and our results agree with their findings. Our approach is useful in finding the specific streamflows that control the composition and structure of the vegetation community. Moreover, it can guide predictions of how changes in the riparian vegetation community can affect water deliveries to the coast. This is significant because Mission River has a skewed streamflow distribution with > 66% of flows passing the 08189500 gage (the most downstream gage) being from direct runoff and flood pulses/events (baseflow separation conducted using the Web-based Hydrologic Assessment Tool from

Lim et al. (2005) and Lim et al. (2010)). Recommendations for freshwater deliveries to the coast from Mission River have been established (Chen, 2010), but the contribution and influence from flood pulses/events is not explicitly considered. We find this troubling because our analysis has shown that significant river-floodplain interaction is occurring at river-stage values > 3 m and this can affect the timing, quantity, and quality of water delivered to the coast. Mission River flows can be broken into three components: (1) flows unlikely to interact with the floodplain (stage < 3 m); (2) flows likely interacting with the floodplain (3 m < stage < 6 m); and (3) flows that are very likely interacting with the floodplain (stage > 6 m; i.e., above bankfull conditions). Analyzing mean daily stage and discharge records from the 08189500 gage for the time-period from 2006 through 2015, the components of total discharge are 40, 45, 15%, for the aforementioned components of streamflow, respectfully. The large quantities of water that are likely or very likely interacting with the floodplain will undoubtedly impact the timing, quantity, and quality of freshwater delivered to the Mission-Aransas estuary downstream.

There are a few limitations with our analysis that merit further discussion. First, we are unable to determine the exact collection date for the LiDAR data that we use to generate a DTM of the floodplain. River stage varied by 2.2 m during the known acquisition time-period and our use of a mean value (1.4 m) introduced uncertainty in the river-stage values that we used in our analysis. Second, the accuracy of our DREM is not analyzed, and it further adds uncertainty to our analysis. Third, our conceptualization of inundation within the floodplain does not consider hydrodynamics or influences from

groundwater. The inclusion of these factors would likely have yielded different inundation and connectivity patterns. Subsequent work that we have performed (Chapter III) has indicated that our morphometric approach used here tends to overestimate surface-water inundation. This is likely related to our aforementioned first and third limitations. In future work we will pursue using water-surface elevations from published Flood Insurance Studies in our generation of the DREM to determine if this yields better estimates of inundation. Forth, we only simulate a rising river stage. The de-watering of the floodplain represents other significant processes (e.g., ponding, infiltration, evapotranspiration, etc.) that also influence the structure and function of river-floodplain systems. Finally, our graph conceptualization of the river-floodplain drainage system indicates a hub-like structure that resembles scale-free graphs. However, our use of Drop analysis within TauDEM ensured that the delineated floodplain flow network followed "Horton's laws of drainage network composition". The Horton-Strahler drainage network classification scheme divides the network into a set of orders (or scales) that theoretically follow scale-free principles (Li et al., 2005). This begs the question of how much of the pattern we observe can be attributed to mathematical remnants of the delineation algorithm. Nonetheless, this work is a step towards better understanding river-floodplain interactions and implications associated with variations in the level of interaction. In our future work, we will compare the results from this study to those obtained from other methods for determining floodplain inundation and flow patterns. Furthermore, applications of our framework to other river-floodplain systems are needed

to determine to how broadly the relationships that we identified in this study between river stage and connectivity hold in these types of environments.

Conclusions

River-floodplain connectivity is a major factor in the health of riverine and riparian habitats, and understanding the processes involved is of critical importance (National Research Council, 2010). In this work, we use data on floodplain topography and streamflow in graph theoretical framework to characterize the differing levels of connectivity within a floodplain that are induced by variations in river stage (i.e., surface-water connectivity). We found that connectivity induced by surface water has a nonlinear relationship with river stage supporting earlier findings that widespread connectivity can occur below published bankfull conditions. We also found that connectivity is maintained by a hub-like structure. The physical locations of these hubs are critical components of the river-floodplain system and they should be preserved if river-floodplain connectivity is the management objective. Our analysis can be used to determine when the river-floodplain system is in a synchronized state of surface-water connectivity. This type of information can inform management and restoration strategies for riparian species that prefer specific levels of river-floodplain connectivity.

In this study, we adopted a simple morphometric approach for simulating flood inundation as predicted by the flood pulse concept; however, our proposed framework which relies on object-based and graph analysis also lends itself well to other river-floodplain connectivity analyses that use flood estimates from mechanistic inundation models. While more testing of our proposed framework is needed, we believe that our

approach is a step towards developing a robust methodology for quantifying the variability of surface-water connectivity within river-floodplain environments.

References

ALLAN, J. D. 2004. Landscapes and riverscapes: The influence of land use on stream ecosystems. Annual Review of Ecology, Evolution, and Systematics, 35, 257-284.

AMOROS, C. & ROUX, A. L. 1988. Interaction between water bodies within the floodplains of large rivers: function and development of connectivity. Münstersche Geographische Arbeiten,, 29, 125-130.

BIGGS, N. 1993. Algebraic graph theory, Cambridge : Cambridge University Press 1993. 2nd ed.

BISHOP-TAYLOR, R., TULBURE, M. G. & BROICH, M. 2015. Surface water network structure, landscape resistance to movement and flooding vital for maintaining ecological connectivity across Australia's largest river basin. Landscape Ecology, 30, 2045-2065.

BORNETTE, G. & PUIJALON, S. 2011. Response of aquatic plants to abiotic factors: A review. Aquatic Sciences, 73, 1-14.

BUIJSE, A. D., COOPS, H., STARAS, M., JANS, L. H., VAN GEEST, G. J., GRIFT, R. E., IBELINGS, B. W., OOSTERBERG, W. & ROOZEN, F. C. J. M. 2002. Restoration strategies for river floodplains along large lowland rivers in Europe. Freshwater Biology, 47, 889-907.

CANTWELL, M. D. & FORMAN, R. T. T. 1993. Landscape graphs: Ecological modeling with graph theory to detect configurations common to diverse landscapes. Landscape Ecology, 8, 239-255.

CHARTRAND, G. 1977. Introductory Graph Theory, New York, New York, Dover Publications, INC.

CHARTRAND, G. & LESNIAK, L. 1986. Graphs & Digraphs, Monterey, CA, Wadsworth & Brooks/Cole Advanced Books & Software.

CHEN, G. F. 2010. Freshwater Inflow Recommendations for the Mission-Aransas Estuarine System. Austin, TX: Texas Parks and Wildlife Department: Ecosystem Resources Program: Coastal Fisheries Division.

DAVIS, N. A. & SMITH, E. H. 2013. Dynamics of a community of dominant woody riparian species along a coastal river of Texas. Southwestern Naturalist, 58, 286-298.

DUAN, Z.-S., WANG, W.-X., LIU, C. & CHEN, G.-R. 2009. Are networks with more edges easier to synchronize, or not? Chinese Physics B, 18, 3122-3130.

DUDGEON, D., ARTHINGTON, A. H., GESSNER, M. O., KAWABATA, Z. I., KNOWLER, D. J., LÉVÊQUE, C., NAIMAN, R. J., PRIEUR-RICHARD, A. H., SOTO, D., STIASSNY, M. L. J. & SULLIVAN, C. A. 2006. Freshwater biodiversity: Importance, threats, status and conservation challenges. Biological Reviews of the Cambridge Philosophical Society, 81, 163-182.

FAGAN, W. F. 2002. Connectivity, fragmentation, and extinction risk in dendritic metapopulations. Ecology, 83, 3243-3249.

FERRARI, M. J., BANSAL, S., MEYERS, L. A. & BJØRNSTAD, O. N. 2006. Network frailty and the geometry of herd immunity. Proceedings of the Royal Society of London B: Biological Sciences, 273, 2743-2748.

FORMAN, R. T. T. 1995. Land mosaics: the ecology of landscapes and regions, Cambridge; New York: Cambridge University Press, 1995.

FULBRIGHT, T. E., DIAMOND, D. D., RAPPOLE, J. & NORWINE, J. 1990. The Coastal Sand Plain of Southern Texas. Rangelands, 12, 337-340.

GALAT, D. L. & LIPKIN, R. 2000. Restoring ecological integrity of great rivers: Historical hydrographs aid in defining reference conditions for the Missouri River. Hydrobiologia, 422-423, 29-48.

GASCUEL-ODOUX, C., AUROUSSEAU, P., DORAY, T., SQUIVIDANT, H., MACARY, F., UNY, D. & GRIMALDI, C. 2011. Incorporating landscape features to obtain an object-oriented landscape drainage network representing the connectivity of surface flow pathways over rural catchments. Hydrological Processes, 25, 3625-3636.

GUZZETTI, F., CARRARA, A., CARDINALI, M. & REICHENBACH, P. 1999. Landslide hazard evaluation: A review of current techniques and their application in a multi-scale study, Central Italy. Geomorphology, 31, 181-216.

HARARY, F. 1969. Graph Theory, Philipines, Addison-Wesley Publishing Company, Inc.

HARVEY, J. & GOOSEFF, M. 2015. River corridor science: Hydrologic exchange and ecological consequences from bedforms to basins. Water Resources Research, 51, 6893-6922.

HECKMANN, T., SCHWANGHART, W. & PHILLIPS, J. D. 2015. Graph theory-Recent developments of its application in geomorphology. Geomorphology, 243, 130-146.

HOMER, C., DEWITZ, J., YANG, L., JIN, S., DANIELSON, P., XIAN, G., COULSTON, J., HEROLD, N., WICKHAM, J. & MEGOWN, K. 2015. Completion of the 2011 national land cover database for the conterminous United States - Representing a decade of land cover change information. Photogrammetric Engineering & Remote Sensing, 81, 346-354.

HUDSON, P. F., SOUNNY-SLITTINE, M. A. & LAFEVOR, M. 2013. A new longitudinal approach to assess hydrologic connectivity: Embanked floodplain inundation along the lower Mississippi River. Hydrological Processes, 27, 2187-2196.

ISHIYAMA, N., AKASAKA, T. & NAKAMURA, F. 2014. Mobility-dependent response of aquatic animal species richness to a wetland network in an agricultural landscape. Aquatic Sciences, 76, 437-449.

JONES, K. L., POOLE, G. C., O'DANIEL, S. J., MERTES, L. A. K. & STANFORD, J. A. 2008. Surface hydrology of low-relief landscapes: Assessing surface water flow impedance using LIDAR-derived digital elevation models. Remote Sensing of Environment, 112, 4148-4158.

JORDÁN, F. 2001. Adding function to structure-comments on Palmarola landscape connectivity. Community Ecology, 2, 133-135.

JORDÁN, F., BÁLDI, A., ORCI, K. M., RÁCZ, I. & VARGA, Z. 2003. Characterizing the importance of habitat patches and corridors in maintaining the landscape connectivity of a Pholidoptera transsylvanica (Orthoptera) metapopulation. Landscape Ecology, 18, 83-92.

JUNK, W. J., BAYLEY, P. B. & SPARKS, E. 1989. The floodpulse concept in river-floodplain systems. Canadian Journal of Fisheries and Aquatic Sciences Special Publication, 110-127.

KAPITANIAK, T. 1996. Controlling chaos: theoretical and practical methods in non-linear dynamics, San Diego, CA, Academic Press Limited.

KONDOLF, G. M., BOULTON, A. J., O'DANIEL, S., POOLE, G. C., RAHEL, F. J., STANLEY, E. H., WOHL, E., BÅNG, A., CARLSTROM, J., CRISTONI, C.,

HUBER, H., KOLJONEN, S., LOUHI, P. & NAKAMURA, K. 2006. Process-based ecological river restoration: Visualizing three-dimensional connectivity and dynamic vectors to recover lost linkages. Ecology and Society, 11, 1-18.

KUPFER, J. A., MEITZEN, K. M. & GAO, P. 2014. Flooding and surface connectivity of Taxodium-Nyssa stands in a southern floodplain forest ecosystem. River Research and Applications, 1-12.

LI, L., ALDERSON, D., DOYLE, J. C. & WILLINGER, W. 2005. Towards a theory of scale-free graphs: Definition, properties, and implications. Internet Mathematics, 2, 431-523.

LIM, K. J., ENGEL, B. A., TANG, Z., CHOI, J., KIM, K. S., MUTHUKRISHNAN, S. & TRIPATHY, D. 2005. Automated Web GIS based hydrograph analysis tool, WHAT. Journal of the American Water Resources Association, 41, 1407-1416.

LIM, K. J., PARK, Y. S., KIM, J., SHIN, Y. C., KIM, N. W., KIM, S. J., JEON, J. H. & ENGEL, B. A. 2010. Development of genetic algorithm-based optimization module in WHAT system for hydrograph analysis and model application. Computers and Geosciences, 36, 936-944.

LOGOFET, D. O. 2013. Projection matrices in variable environments: λ1 in theory and practice. Ecological Modelling, 251, 307-311.

MARCOT, B. G. & CHINN, P. Z. Use of graph theory measures for assessing diversity of wildlife habitat. In: LAMBERSON, R., ed. First Pacific Coast Conference on Mathematical Models of Renewable Resources, 1982 Humbholt State University, Arcata, CA.

MEITZEN, K. M., DOYLE, M. W., THOMS, M. C. & BURNS, C. E. 2013. Geomorphology within the interdisciplinary science of environmental flows. Geomorphology, 200, 143-154.

MOSEKILDE, E., MAĬSTRENKO, I. U. L. & POSTNOV, D. 2002. Chaotic synchronization: applications to living systems, Singapore, World Scientific.

NATIONAL RESEARCH COUNCIL 2002. Riparian Areas: Functions and Strategies for Management, Washington, D.C., The National Academies Press.

NATIONAL RESEARCH COUNCIL 2010. Landscapes on the Edge: New Horizons for Research on Earth's Surface, Washington, DC, The National Academies Press.

NELSON, J. & TOLAN, J. 2008. Final Historical Data Review on Mission River and Aransas River Tidal. Austin, TX: Texas Parks and Wildlife Department.

NORWINE, J. & JOHN, K. 2007. The changing climate of South Texas, 1900-2100 : problems and prospects, impacts and implications, Kingsville, TX : CREST-RESSACA, Texas A & M University-Kingsville, 2007.

O'CALLAGHAN, J. F. & MARK, D. M. 1984. The extraction of drainage networks from digital elevation data. Computer Vision, Graphics, & Image Processing, 28, 323-344.

PEUCKER, T. K. & DOUGLAS, D. H. 1975. Detection of surface-specific points by local parallel processing of discrete terrain elevation data. Computer Graphics and image processing, 4, 375-387.

PHILLIPS, J. D. 2011. Predicting modes of spatial change from state-and-transition models. Ecological Modelling, 222, 475-484.

PHILLIPS, J. D. 2012. Synchronization and scale in geomorphic systems. Geomorphology, 137, 150-158.

PHILLIPS, J. D. 2014. State transitions in geomorphic responses to environmental change. Geomorphology, 204, 208-216.

PHILLIPS, J. D., SCHWANGHART, W. & HECKMANN, T. 2015. Graph theory in the geosciences. Earth-Science Reviews, 143, 147-160.

POFF, N. L. 2014. Rivers of the anthropocene? Frontiers in Ecology and the Environment, 12, 427.

POFF, N. L., ALLAN, J. D., BAIN, M. B., KARR, J. R., PRESTEGAARD, K. L., RICHTER, B. D., SPARKS, R. E. & STROMBERG, J. C. 1997. The natural flow regime: A paradigm for river conservation and restoration. BioScience, 47, 769-784.

POFF, N. L., BLEDSOE, B. P. & CUHACIYAN, C. O. 2006. Hydrologic variation with land use across the contiguous United States: Geomorphic and ecological consequences for stream ecosystems. Geomorphology, 79, 264-285.

POOLE, G. C., STANFORD, J. A., FRISSELL, C. A. & RUNNING, S. W. 2002. Three-dimensional mapping of geomorphic controls on flood-plain hydrology and connectivity from aerial photos. Geomorphology, 48, 329-347.

PRINGLE, C. 2003. The need for a more predictive understanding of hydrologic connectivity. Aquatic Conservation: Marine and Freshwater Ecosystems, 13, 467-471.

PRINGLE, C. M. 2001. Hydrologic connectivity and the management of biological reserves: A global perspective. Ecological Applications, 11, 981-998.

RAYFIELD, B., FORTIN, M. J. & FALL, A. 2011. Connectivity for conservation: A framework to classify network measures. Ecology, 92, 847-858.

RESTREPO, J. G., OTT, E. & HUNT, B. R. 2006. Emergence of synchronization in complex networks of interacting dynamical systems. Physica D: Nonlinear Phenomena, 224, 114-122.

RESTREPO, J. G., OTT, E. & HUNT, B. R. 2007. Approximating the largest eigenvalue of network adjacency matrices. Physical Review E, 76, 056119-1 - 056119-6.

RICHTER, B. D. & THOMAS, G. A. 2007. Restoring environmental flows by modifying dam operations. Ecology and Society, 12, 1-26.

RICOTTA, C., STANISCI, A., AVENA, G. C. & BLASI, C. 2000. Quantifying the network connectivity of landscape mosaics: a graph-theoretical approach. Community Ecology, 1, 89-94.

ROBERTSON, C. R., ZEUG, S. C. & WINEMILLER, K. O. 2008. Associations between hydrological connectivity and resource partitioning among sympatric gar species (Lepisosteidae) in a Texas river and associated oxbows. Ecology of Freshwater Fish, 17, 119-129.

SAUNDERS, D. L., MEEUWIG, J. J. & VINCENT, A. C. J. 2002. Freshwater protected areas: Strategies for conservation. Conservation Biology, 16, 30-41.

SCHOENBAECHLER, C. & GUTHRIE, C. G. 2011. Coastal Hydrology for the Mission-Aransas Estuary. Austin, TX, USA: Texas Water Development Board: Surface Water Resources Division - Bays and Estuaries Program.

SCHRAMM, H. L., COX, M. S., TIETJEN, T. E. & EZELL, A. W. 2009. Nutrient dynamics in the lower Mississippi river floodplain: Comparing present and historic hydrologic conditions. Wetlands, 29, 476-487.

SCHREIBER, M. A. & HASTINGS, H. M. 1995. Stability of random matrix models. Rocky Mountain Journal of Mathematics, 25, 471-478.

SPARKS, R. E. 1992. Risks of altering the hydrologic regime of large rivers. Advances in Modern Environmental Toxicology, 20, 119-152.

TARBOTON, D. G. & AMES, D. P. 2001. Advances in the mapping of flow networks from digital elevation data. Bridging the Gap: Meeting the World's Water and

Environmental Resources Challenges - Proceedings of the World Water and Environmental Resources Congress 2001.

TARBOTON, D. G. & MOHAMMED, I. N. 2013. TauDEM ArcGIS Toolbox. 5.1 ed. Logan, Utah, USA: Hydrology Research Group - Utah State University.

TAYLOR, D. & RESTREPO, J. G. 2011. Network connectivity during mergers and growth: Optimizing the addition of a module. Physical Review E - Statistical, Nonlinear, and Soft Matter Physics, 83.

TINKLER, K. J. 1972. The Physical Interpretation of Eigenfunctions of Dichotomous Matrices. Transactions of the Institute of British Geographers, 17-46.

TOCKNER, K., MALARD, F. & WARD, J. V. 2000. An extension of the flood pulse concept. Hydrological Processes, 14, 2861-2883.

TOCKNER, K., PUSCH, M., BORCHARDT, D. & LORANG, M. S. 2010. Multiple stressors in coupled river-floodplain ecosystems. Freshwater Biology, 55, 135-151.

TOCKNER, K. & STANFORD, J. A. 2002. Riverine flood plains: Present state and future trends. Environmental Conservation, 29, 308-330.

TREML, E. A., HALPIN, P. N., URBAN, D. L. & PRATSON, L. F. 2008. Modeling population connectivity by ocean currents, a graph-theoretic approach for marine conservation. Landscape Ecology, 23, 19-36.

URBAN, D. L., MINOR, E. S., TREML, E. A. & SCHICK, R. S. 2009. Graph models of habitat mosaics. Ecology Letters, 12, 260-273.

USGS 2016. National Water Information System data available on the World Wide Web (USGS Water Data for the Nation). In: U.S. GEOLOGICAL SURVEY (ed.). Available: https://waterdata.usgs.gov/nwis/inventory/?site_no=08189500&agency_cd=USGS.

WANG, Y., COLBY, J. D. & MULCAHY, K. A. 2002. An efficient method for mapping flood extent in a coastal floodplain using Landsat TM and DEM data. International Journal of Remote Sensing, 23, 3681-3696.

WOHL, E. 2017. Connectivity in rivers. Progress in Physical Geography, 41, 345-362.

WOHL, E., BRIERLEY, G., CADOL, D., COULTHARD, T. J., COVINO, T., FRYIRS, K. A., GRANT, G., HILTON, R. G., LANE, S. N., MAGILLIGAN, F. J., MEITZEN, K. M., PASSALACQUA, P., POEPPL, R. E., RATHBURN, S. L. &

SKLAR, L. S. 2018. Connectivity as an emergent property of geomorphic systems. Earth Surface Processes and Landforms, 44, 4-26.

WOHL, E., GERLAK, A. K., POFF, N. L. & CHIN, A. 2014. Common core themes in geomorphic, ecological, and social systems. Environmental Management, 53, 14-27.

YUAN, W.-J., LUO, X.-S., JIANG, P.-Q., WANG, B.-H. & FANG, J.-Q. 2008. Transition to chaos in small-world dynamical network. Chaos, Solitons & Fractals, 37, 799-806.

CHAPTER III

SCALE-FREE STRUCTURE OF SURFACE-WATER CONNECTIVITY IN A LOWLAND RIVER-FLOODPLAIN LANDSCAPE

Introduction

Connectivity between a river and its floodplain is a major driver of water, sediment, nutrient, and biotic exchanges within river-floodplain systems in lowland environments and it ultimately creates the heterogeneous pattern of habitats and landforms commonly found within these landscapes (Junk et al., 1989, Meitzen et al., 2013, Poff et al., 1997). Surface-water inundation from overbank river flows enable the largest and most abrupt exchanges between patches of the lowland river-floodplain landscape (Junk et al., 1989, Poff et al., 1997). However, widespread surface-water inundation throughout a lowland river-floodplain landscape can occur with river flows below published bankfull flow conditions (Czuba et al., 2019, Kupfer et al., 2014, Meitzen et al., 2013). The hydrologic connectivity concept – where water is considered the conduit through which matter, energy, biota, and information is transferred between elements of the Earth surface system (Pringle, 2001) – has been widely used to analyze river-floodplain processes that depend on surface-water inundation (Hudson et al., 2013). The connections between landscape patches induced by surface-water inundation within the lowland river-floodplain landscape creates a dynamic network whose size and configuration will depend on river flows. This type of conceptualization to a hydro-geomorphic system lends itself well to ideas and methods from graph and network

theory that relies on the structure of interaction between system elements to infer system behavior (Heckmann et al., 2015).

Complex networks theory has been widely applied to understand interactions in social, information, technological, biological, and Earth systems (Newman, 2003, Wang and Chen, 2003, Phillips et al., 2015, Heckmann et al., 2015, Broido and Clauset, 2019). Numerous universal network structures have been identified and the scale-free structure is one that has drawn considerable attention (Newman, 2003, Wang and Chen, 2003). However, there are debates in the literature over the universality of scale-free networks (Broido and Clauset, 2019, Holme, 2019). Nonetheless, scale-free networks have been found to exhibit some interesting properties – some examples include growth by preferential attachment (Barabási and Albert, 1999), efficiency in the transfer of information and materials (Crucitti et al., 2003, Pastor-Satorras and Vespignani, 2001), error tolerance (Albert et al., 2000), attack vulnerability (Holme et al., 2002), and emergent synchronization (Restrepo et al., 2006). These properties have found utility in disciplines that readily use network concepts and it merits investigating if they also apply to connectivity patterns in lowland river-floodplain landscapes. Here we present the first documented example of a (roughly) scale-free network structure that is induced by surface-water connections within a river-floodplain landscape. Surface-water connection can originate from surface- and ground-water processes (Junk et al., 1989, Tockner et al., 2000, Stanford and Ward, 1993, Poole, 2002), but here we investigate the topological pattern of connection from a strictly surface-water perspective.

Study Area and Approach

Our study area (A_s) is 46.3 km^2 of lowland floodplain and coastal plain that surrounds a 16 km reach of Mission River on the Coastal Bend of Texas (Figure III-1a, III-1b, and III-1c). We use a gridded lidar-based digital terrain model (DTM) to represent the topography (Figure III-1c) and two ecological land classifications – soil-based land classification (soil-patches, herein after) and vegetation-based land classification (vegetation-patches, herein after) – to represent landscape patches within the study area (see *Methods* and Tables B-1 and B-2 for descriptions of land classifications and how each dataset was developed). Both land classifications exhibit high variability in terms of their area (coefficient of variation is 3.07 and 4.23 for soil- and vegetation-patches, respectively). Tight sandy loam (TSL) and blackland prairie (B) are the soil-patches with the greatest proportion of A_s (26.7 and 17.1%, respectively), but loamy bottomland (LB) and clayey bottomland (CB) have the greatest proportion within the floodplain (13.9 and 13.7% of A_s, respectively; Figure III-1d; Table B-1). Upland prairie/grassland (UPG) and upland mesquite woodland/shrubland (UMW) are the vegetation-patches with the greatest proportion of A_s (25.7 and 16.8%, respectively), while floodplain/riparian hardwood forest (FHW) and floodplain/riparian grassland (FG) have the greatest proportions within the floodplain (13.6 and 5.5% of A_s, respectively; Figure III-1e; Table B-2).

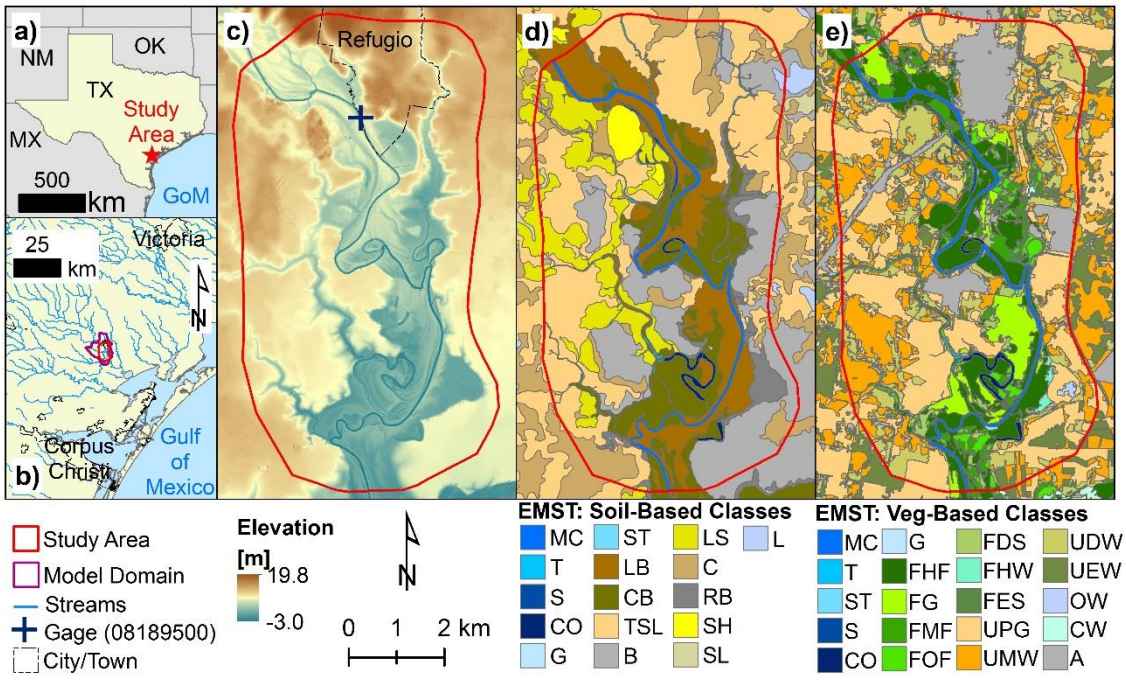

Figure III-1. Maps showing the location of the study area and the static spatial datasets used in the analysis. (a) Map showing where the study area lies on the Coastal Bend of Texas. (b) Regional map showing the study area and hydrodynamic model domain between the cities of Victoria and Corpus Christi. (c) Digital terrain model for the study area that includes parts of the Town of Refugio. The location of the 08189500 USGS gaging station is also shown. (d) Map of soil-patches used to establish the soil-network. Soil-patches have a mean area of 0.11 km2 and coefficient of variation of 3.07. (e) Map of vegetation-patches used to establish the vegetation-network. Vegetation-patches have a mean area of 0.02 km2 and coefficient of variation of 4.23. (Note: description of patch datasets can be found in Tables B-1 and B-2.)

Inundation from riverine surface water creates a continuous surface that connects inundated landscape patches and generates a dynamic network whose size, configuration, and function is dependent on river flow. Here we conduct two analyzes of the connections between inundated landscape patches – (1) soil-patches and (2) vegetation-patches – by simulating an ensemble of flood scenarios that span the historical flow record for Mission River (See *Methods* for description of flood model and Figure B-1 for historical flow records). Connectivity is quantified by conceptualizing two networks - (1) soil-network and (2) vegetation-network - where the vertices are

inundated portions of each patch and edges between vertices are established when the boundary between adjacent patches is breached by surface water (Figure III-2). We then analyze the topology and algebraic representation of both networks at each simulated flow to characterize the dynamic properties of surface-water connectivity within the landscape.

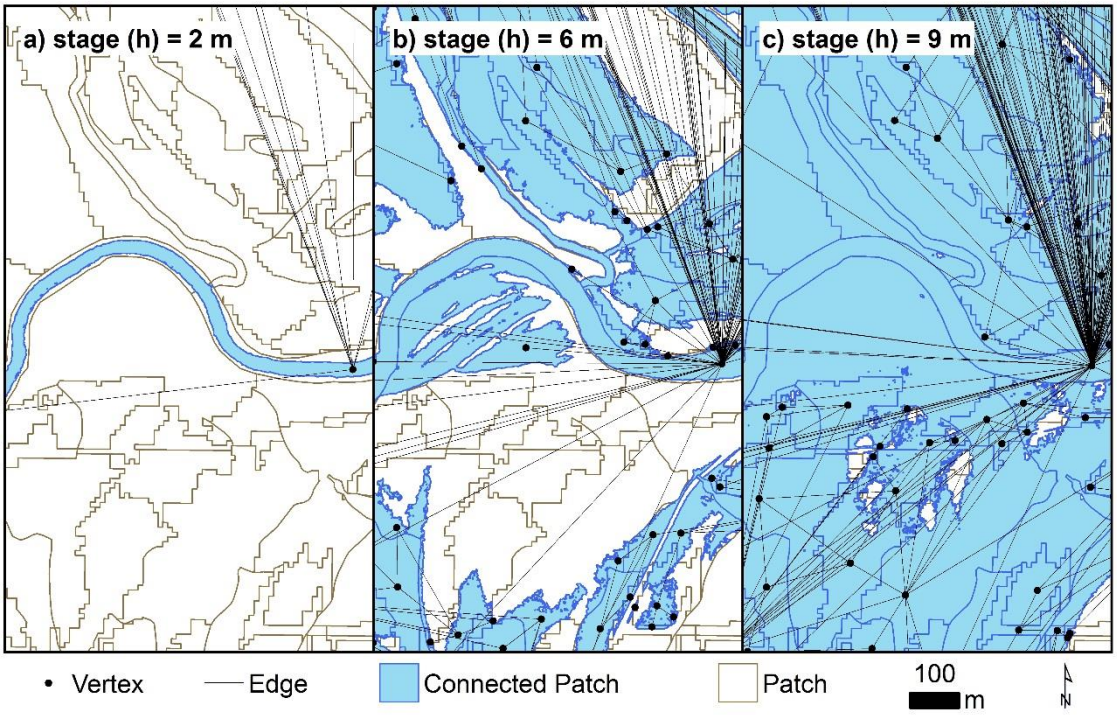

Figure III-2. Visual representation of the conceptualization used here to develop the state of a landscape network for each of the 23 simulated flows. A patch is considered connected when it becomes inundated in one of our simulations. As examples, zoomed-in views of the vegetation-network for the simulations with stage of (a) 2.00 m, (b) 6.00 m, and (c) 9.00 m are shown.

Methods

Data

We use daily streamflow records for the U.S. Geological Survey gaging station at Refugio, TX (Site Number: 08189500) from Jul-1939 through Dec-2018 to characterize the flow regime. Time-series plots of stage (h) and discharge (Q) for this time-period are

shown in Figures B-1a and B-1b. These flow records and the most recent version of the rating curve (stage and discharge relationship) for this station inform the development of our model and the flow scenarios (Figure B-1c) that we used in our analysis of surface-water connectivity. Streamflow records indicate that stage (h) has a mean of 0.9 m and range of 0.0 to 11.3 m. Discharge (Q) has a mean of 3.5 m^3/s and a range of 0.0 to 1902.9 m^3/s.

We represent the terrain with a gridded bare-earth digital terrain model (gDTM) at 1-m spatial resolution that was developed using two lidar-based gDTMs. Our primary gDTM dataset entirely contains our study area and it was developed by the National Center for Airborne Laser Mapping (NCALM) using lidar point clouds collected in Mar-2018 with a point-density of 10-20 points/m^2. This NCALM-gDTM was originally at a spatial resolution of 0.5-m, but we resampled it to a spatial resolution of 1-m using bilinear interpolation. The submerged topography for portions of the main channel were synthetically generated using channel bed elevations from a detailed Flood Insurance Study (FIS) conducted by FEMA (FEMA, 2014) and methods from Legleiter and Kyriakidis (2008). The accuracy of the submerged topography was assessed using bathymetric estimates from eight channel cross-sections determined using a Sontek M9 acoustic doppler current profiler (ADCP). Root mean squared deviations (RMSD) and mean absolute deviations (MAD) between the synthetic channel topographies and ADCP cross-sections is 76 and 62 cm, respectively, which outperforms the raw NCALM-DTM that has an RMSD and MAD of 250 and 220 cm. Portions of the landscape surface still included within the model domain but not captured by the NCALM-DTM are

represented by a gDTM that was collected by Sanborn Mapping under the auspices of the Federal Emergency Management Agency (FEMA) and the Texas Water Development Board (TWDB). This FEMA-TWDB-DTM was downloaded from the Texas Natural Resource Information System website (TNRIS.org) at a spatial resolution of 1.4-m and we resampled it to a spatial resolution of 1-m using bilinear interpolation. Both gDTMs were mosaicked/merged with a 0.5 km overlap. Elevation values for areas where both gDTMs overlapped where determined using a weighted average where locations closer to the geographic core of a respective gDTM received a higher weighting for that particular gDTM. The final gDTM has a mean elevation of 13.1 m and a range of -3.9 to 31.0 m.

We use two types of landscape patch – (1) soil- and (2) vegetation-patches – in our connectivity analysis that are based on combinations of digitized geomorphic features and composite land classifications from the Ecological Mapping Systems of Texas (EMST) dataset (Elliott et al., 2014). Our gDTM and aerial imagery from 2016 and 2018 were used to digitize/manually-delineate geomorphic features created by fluvial processes within the model domain. The features we digitized appear in both patch datasets and they include the main channel (MC), tributaries to MC (T), sloughs or slow channels (S), cutoffs and oxbow lakes (CO), gullies and hillslope drainages (G), and small tributaries that have confluences with T (ST). Areas that are not captured by the geomorphic delineation are assigned the composite EMST classifications. The EMST can be divided into a variety of categories and we use the soil- and vegetation-based ecological classifications. Some of the vegetation-based classes were similar and

these were combined to create composite classes. The final datasets of soil- and vegetation-patches have 16 and 20 classes and descriptions are shown in Tables B-1 and B-2. The soil-patches within the study area has 231 individual patches with a mean area of 0.11 km^2 and a coefficient of variation of 3.1. The vegetation-patches within the study area has 1860 individual patches with a mean area of 0.02 km^2 and coefficient of variation of 4.2.

Flood Model

We employ the two-dimensional (2D) flood modeling capabilities of the Hydrologic Engineering Center's - River Analysis System (HEC-RAS) (Brunner, 2016). We chose HEC-RAS for our flood modeling environment because it utilizes a finite volume numerical solver that allows sub-cell inundation that is informed by the underlying terrain (our gDTM) and creates within cell flow-paths. Our HEC-RAS model has a domain of 119 km^2 and a regularly spaced computational mesh with 527,505 computational cells that have a mean cell size of 15 by 15 m. We also have spatially varying Manning's roughness coefficient (n_{Mann}) values with a mean of 0.27 and range of 0.01 to 0.49. A Flow Hydrograph (time-series of Q) external boundary condition at the upstream-end of the main channel/floodplain for Mission River brings water into the model domain and Normal Depth (approximation of Manning's flow equation) external boundary conditions at the downstream-end of the main channel/floodplain and upstream-ends of tributaries remove water from the domain. Our model is calibrated to longitudinal water surface elevation (WSE) profiles from a recent detailed FEMA flood insurance study (FIS) for Refugio County (FEMA, 2014). These FIS-WSE profiles are

for four flow scenarios with varying chances of occurring in a given year (10% chance or 10-year return period, 2% chance or 50-year return period, 1% chance or 100-year return period, and 0.2% chance or 500-year return period). Our model has root mean squared deviation (RMSD), mean absolute deviation, and percent bias of 0.20 m, 0.16 m, and 0.30%, respectively, with the FIS values. A plot comparing our WSE values with those from the FIS is shown in Figure B-6.

We use our calibrated HEC-RAS model to simulate 23 steady flow scenarios (22 with stages (h) of 1.0-11.5 m that sequentially increased by 0.5 m and the flood of record that had an h of 11.63 m). 2D simulations within HEC-RAS are part of the unsteady simulations module that necessitates synthetic data that incrementally increases flow coming into the model domain until the flow of interest is attained. We use the most recent rating curve from the U.S. Geological Survey for the 08189500 gage to construct synthetic time-series' on a 15-minute interval. The time-series of flow data for each scenario is constructed in three general steps. First, the lowest non-zero value in the rating curve is repeated 192 times to create two-days of data within the time-series. Second, we append new values to the time-series that incrementally increase the flow by sampling the rating curve in ascending order with each data point in the curve being repeated four times (1-hour within the time-series) until the flow of interest is met. Third, 672 new values are appended to the time-series by repeating the flow value of interest to create one-week of data. The number of data points in the 23 steady flow scenarios ranges from 1010 to 4498 for the smallest and largest simulations, respectively. With the exception of the flow time-series coming into the model domain,

we identically simulate all flow scenarios using wave diffusion hydraulic equations and a 5-minute computational time-step.

The HEC-RAS outputs that we use in our connectivity analysis are spatially explicit raster datasets of inundation depth that are post-processed before they are used. The post-processing involves clipping the raster datasets to the study area boundary and we filter out any spurious inundation that is not part of the continuous water surface that corresponds to the main channel of the river. We also filter out inundated areas with a depth ≤0.2 m because our model has a RMSD of 0.2 m with the FIS scenarios to which our model is calibrated.

Network Conceptualization

Inundation from riverine surface water creates a continuous surface that connects inundated landscape patches and generates a dynamic network. Here we conceptualize two networks - (1) soil-network and (2) vegetation-network – because we use two landscape patch datasets with differing spatial properties (See Figures III-1d, III-1e, and Tables B-1 and B-2). Inundated portions of each patch become the vertices of the network and edges between vertices are established when the boundary between adjacent patches is breached by surface water. Each network is dynamic because the number of vertices and edges will depend on river flow conditions. Moreover, a single landscape patch can produce more than one vertex in the corresponding network when there are multiple inundated portions for a given river flow. These multiple vertices can merge to a single vertex when these portions become inundated for a different flow. These dynamics make for unique networks and we compare the soil- and vegetation-networks

to each other to determine if there are differences in the major differences in network properties and dynamics.

Analysis of Scale-Free Network Properties

We analyze the properties of the soil- and vegetation-networks to determine if they can be considered as scale-free using methods from Broido and Clauset (2019). The primary criterion of a scale-free network is a degree (k) distribution that follows a power-law with specific properties (size of network and power-law parameters). Broido and Clauset (2019) also put forth a classification scheme that categorized the degree to which a network can be considered scale-free. These categories include *super-weak* (no alternative-distribution fit outperforms the power-law fit for ≥50% of the network instances), *weakest* (the *p-value* ≥ 0.10 for the goodness-of-fit statistic of the power-law for ≥50% of network instances), *weak* (the requirements from *weakest* and the tail-end of the k distribution (n_{tail}) over which the power-law is fit has ≥50 vertices), *strong* (requirements of *weak*, *super-weak*, and the scaling index (exponent) from the power-law fit (α) has values of $2 \leq \alpha \leq 3$ for ≥50% of network instances), *strongest* (requirements of *strong* for ≥90% of network instances and requirements of *super-weak* for ≥95% of network instances), and *not scale-free* (network cannot be categorized as *super-weak* or *weak*).

We use codes provided by Broido and Clauset (2019) to analyze the state of the soil- and vegetation-network at each of the 23 simulations in order to determine their scale-free classification. The first aspect of the analysis is to fit a power-law to the k distribution and compare this fit to four other fits using tail-heavy distributions that

include exponential, log-normal, power-law with exponential cutoff (plwc), and Weibull. Sets of likelihood ratio tests (R) are used to compare the power-law fit to each of the other tail-heavy distribution fits. There can be three types of results using the parameterization used here; (1) a positive value for R indicates that the power-law fit outperforms the alternative-distribution fit; (2) a negative value for R indicates that the alternative-distribution fit is preferred over the power-law fit; and (3) a zero value for R indicates that the test is inconclusive and there is no clear favorite between the power-law fit and the alternative-distribution fit. R is subject to statistical uncertainty and a standard *p-value* is used to determine the reliability of R with a *p-value* ≤ 0.10 indicating that the value of R is reliable. The second aspect of the analysis is to determine the goodness-of-fit of the power-law to the k distribution. A test statistic with a standard *p-value* are generated that determines the plausibility of a power-law for the data and a *p-value* ≤ 0.10 indicates that a power-law is plausible for the k distribution. The third aspect of the analysis involves analyzing the properties of the fitted power-law. Scale-free networks tend to be relatively large and it is only appropriate to fit a power-law to the tail-end of the k distribution (Broido and Clauset, 2019, Clauset et al., 2009); thus, a $n_{tail} \geq 50$ is also needed. Moreover, scale-free distributions have an infinite second moment, but a finite first moment and an $2 \leq \alpha \leq 3$ for the power-law fit is also needed to meet this criterion.

Other Topological and Algebraic Network Metrics

Scale-free networks have some other properties not analyzed by Broido and Clauset (2019) and we compute nine sets of indicators for some these properties here.

The first three indicators are (or are similar to) simple, but standard metrics used to describe any graph or network. Indicators four, five, and six are standard metrics of the topological arrangement of the network. The last three metrics are commonly used for inferring some of the behavior/dynamics of complex networks.

Our first indicator is the number of vertices in a network (n) that can have values $0 < n \leq \infty$ is an important measure of network size. Moreover, how n varies with the processes that created the network can help determine changes to its structure and function. Our second indicator is the normalized edge count for the network ($m_{norm} = (m - m_{min}) / (m_{max} - m_{min})$; m is the edge count; m_{min} and m_{max} are the theoretical minimum and maximum for a given n using methods from Phillips (2012)) can have values of $0 \leq m_{norm} \leq 1$ with values closer to the endmembers indicating that the network is close to the theoretical bounds for a given n. m_{norm} provides a means to determine if the connectivity within the network is driven by a large value of m or if it is more concentrated to connections that are associated to a small number of key vertices. The third indicator is the mean vertex degree ($\bar{k}$) that can have values of $0 < \bar{k} \leq \infty$. $\bar{k}$ is an important measure of the overall connectivity in a network and it has also been used as an indicator of the mean accessibility of vertices (or patches in this case) in the network (Rayfield et al., 2011).

Our fourth indicator is the mean geodesic (shortest) distance (l) between any two vertices in the network and it can have values of $1 \leq l < m$. The geodesic distance between any two vertices is the number of edges needed in order to traverse from one to the other. l is the mean for all vertex pairs in the network and it is commonly used as a

measure of the small-world effect (most vertex pairs are connected through a small number of popular paths) in the connectivity of a network (Newman, 2003). Our fifth indicator is the clustering coefficient (C) for the network that can have values of $0 \leq C \leq 1$ with values closer to 1 indicating more clustering. *C* is a measure of the fraction of connected triples of vertices with a third edge in order to complete a triangle (connected triples are sets of three vertices that are connected by at least two edges); and it has been used to infer the small-world and hub-like effects in a network (Newman, 2003). Our sixth indicator is the normalized network-level betweenness centrality (C_{btw}; also known as the centralization index) that can have values of $0 \leq C_{btw} \leq 1$ with values closer to one indicating that the network is closer to the theoretical maximum centralization for a given *n*. Values closer to the one indicate that the network has a small number of highly central vertices that are important to the overall connectivity of the network. This not because these vertices have a high degree (although they can), but it is because they lie between major clusters of vertices or they are positioned within "bottlenecks" of the network. C_{btw} can be used to conduct analyzes of "betweenness" that has commonly been used to understand the resilience of network connectivity (Holme et al., 2002, Newman, 2003).

Our seventh indicator is the largest eigenvalue of the network adjacency matrix (λ_1; also known as the spectral radius) that has been used to infer network complexity and the critical coupling strength needed for the onset of network synchronization (Phillips, 2012, Phillips et al., 2015). Here we compare λ_1 to the theoretical maximum for a given *n* (λ_{max}) and the theoretical upper bound for a given *n* and *m* (λ_{upper}) by

dividing λ_1 with these theoretical values (See Phillips (2012) for methods to calculate λ_{max} and λ_{upper}). The λ_1/λ_{max} and $\lambda_1/\lambda_{upper}$ ratios determine how much the structure of the network has reduced the overall λ_1. To further decompose the aspects of the network structure that are reducing λ_1, we also calculated our eighth set of indicators that are the relative contributions (ξ) to λ_1 from the number of connections/edges in the network (ξ_{conn}) and the pattern/wiring of these connections/edges between vertices ($\xi_{wir;}$ See Phillips (2012) for methods to calculate ξ_{conn} and ξ_{wir}). Our ninth indicator is the second smallest eigenvalue of the network Laplacian matrix ($\lambda(A)_{N-1}$; also known as the algebraic connectivity) that is commonly used to measure network synchronization that occurs when the elements of the system are operating in unison or in a predictable sequence. Here we normalize $\lambda(A)_{N-1}$ using the theoretical values for a given *n* that include the maximum ($\kappa(A)$; known as the vertex connectivity) and minimum ($4/nD$; where *D* is the network diameter) that gives it a range of $0 \leq \lambda(A)_{N-1,norm} \leq 1$. The use of these ratios (λ_1/λ_{max} and $\lambda_1/\lambda_{upper}$), relative contributions (ξ_{conn} and ξ_{wir}), and normalized values ($\lambda(A)_{N-1,norm}$) allow us to compare our behavioral metrics between our soil- and vegetation-metrics; as well as other complex networks reported in the literature.

Results

Flooding Patterns and Patch Inundation

We generated 23 steady simulations of river flow (22 with stages (*h*) of 1.0-11.5 m that sequentially increased by 0.5 m and the flood of record that had an *h* of 11.63 m). Inundated area (A_I) increases nonlinearly and here we describe flood dynamics using

three general phases of the river-floodplain inundation process. The first phase (channel-inundation) is for simulations with $h \leq 2.5$ m where the spatial extent of inundation is mostly limited to the main channel (MC) and tributary (T) patches for both land classifications (Figures III-2a, III-2b and Figure B-1). A_I increases from 0.7 to 1.4% of A_s with MC and T collectively composing >98% of the inundation for all channel-inundation simulations (MC decreases from 99.5 to 89.4% of A_I).

The second phase (some-floodplain-inundation) is for simulations with $3.0 \leq h \leq 8.0$ m and this corresponds to when there is some inundation within the floodplain, but it is not necessarily from overbank flows (Figures III-2a, III-2b, and Figure B-1). There is a relatively large range of flows in this phase because the floodplain morphology differs between upstream and downstream portions of the study area (upstream parts are an incised terrace system and downstream parts are a meandering alluvial system). The downstream parts experience some flooding within the floodplain starting at the simulation with $h = 3.0$ m and most of the inundation occurs in cutoff/oxbow (CO) patches and other patches that surround these areas. For simulations with $3.0 \leq h \leq 5.0$ m, A_I increases from 1.8 to 7.8% of A_s (MC ranges from 73.1 to 22.2% in its contribution to A_I for both networks). Starting at $h = 5.0$ m, patches that are not floodplain channels/landforms become the largest contributors to A_I with clayey bottomland (CB) being the dominant type of soil-patch (3.4% of A_I) and floodplain/riparian hardwood forest (FHF) being the dominant type of vegetation-patch (2.1% of A_I). Considerable inundation within upstream parts of the floodplain starts occurring at the simulation with $h = 5.5$ m and this is largely driven by inundation in slough (S) and tributary (T)

channels (Figure B-2). For simulations with $5.5 \leq h \leq 8.0$ m, A_I increases from 13.1 to 26.3% of A_s. CB and FHF continue being the largest contributors to A_I for their respective land classifications as they compose 11.1 and 9.6% of A_I for the simulation with $h = 8.0$ m.

The third phase (overbank-inundation) of the inundation process represents overbank flows because these flows are at or above the break in the rating curve (Figure B-1c). Here this represents simulations with $8.5 \leq h \leq 11.63$ m where A_I increase from 29.7 to 48.9% of A_s. The patch types from the land classifications with largest contribution to A_I are CB (decreases from 40.4 to 28% of A_I) and FHF (decreases from 36.1 to 27.7% of A_I). For simulations with $h \geq 10.5$ m, flood inundation becomes a continuous water surface within the floodplain and water begins to spill onto upland parts of the coastal plain (Figure B-2). All land classifications shown in Figures III-2a and III-2b experience inundation for the largest flow simulation ($h = 11.63$ m). The upland patches with the greatest contribution to A_I for the largest flow simulation tight sandy loam (TSL; 10.9% of A_I) for the soil-patches and upland prairie/grassland (UPG; 11.1% of A_I).

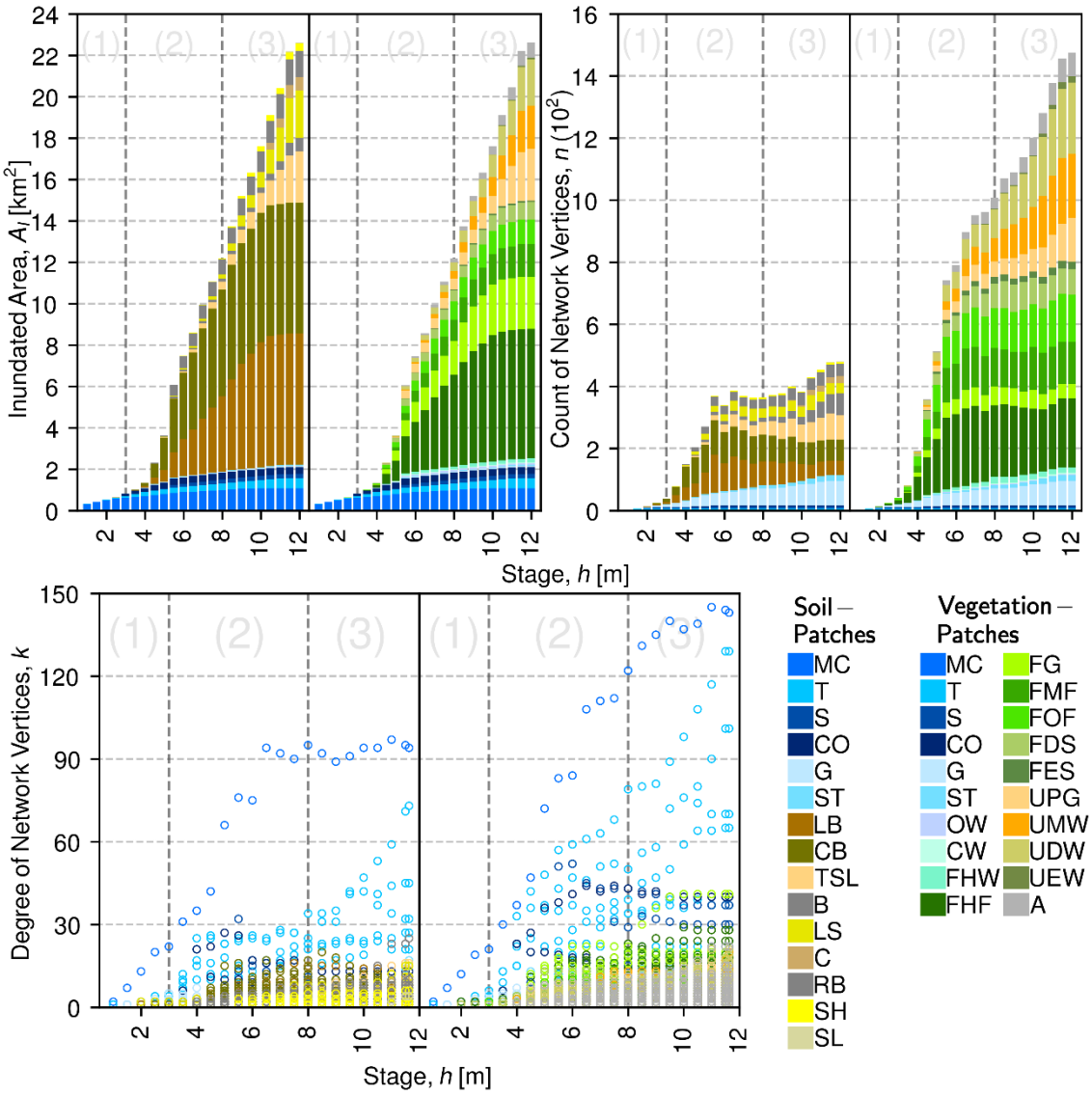

Figure III-3. The contribution to inundated area (A_I) by the (a) soil- and (b) vegetation-patches for each of the 23 hydrodynamic simulations (the h of the flow for each simulation is the x-axis). The inundated portions of patches become vertices in the landscape network and contribution to the number of vertices (n) for the (c) soil- and (d) vegetation-network for each simulated flow is also shown. The number of other vertices that each vertex is connected to (degree (k)) for the (e) soil- and (f) vegetation-network for each of the simulated flows is also shown. (Note: color of data points in the scatter plot is the same as the colors used in the bar charts) See Tables B-1 and B-2 for a description of land classifications.

Analysis of Scale-Free Network Properties

The configuration of the two inundation-induced landscape networks for each of the 23 flow simulations are shown in Figures B-3 (soil-network) and B-4 (vegetation-network). Network size (number of vertices (*n*) and edges (*m*)) increases with the size of the flow being simulated. The number of vertices (*n*) ranges from 3 to 480 for the soil-network and 3 to 1478 for the vegetation-network (Figures III-3c and III-3d). This difference is because the soil-network is based on a land classification that has a mean patch area that is 4.3 times larger than the vegetation land classification (Tables B-1 and B-2). There are three vertices (one that pertains to the single MC patch and two that pertain to two of the six T patches) appear in every network state and these vertices are among the most important drivers of connectivity for all network states. This is because these patches and other floodplain channel/landform patches have lower relative elevations and elongated shapes that allow them to connect to a large number of neighbors and thus have large vertex degree (*k*; Figures III-2e and III-2f).

With regard to the phases of the river-floodplain inundation process, the T patch type is the greatest contributor of vertices to *n* for both networks in the channel-inundation phase (*n* from T decreases from 66.7 to 24.0% with increasing *h*; Figures III-2c and III-2d). In terms of *k*, the sole vertex that pertains to the MC patch for both networks dominates with values that are as much as 7 times greater than the next highest *k* for all vertices in the same network state (Figures III-2e and III-2f). In the some-floodplain-inundation phase, the soil-patches with the greatest contribution to the *n* for each network state are CB and LB with ranges of 23.3 to 44.7% and 17.9 to 33.3%,

respectively. For the vegetation-network, the greatest contribution to *n* is from FHF patches with a range of 22.8 to 39.5% of the *n* for the network. The sole MC vertex continues to have the highest *k* in both networks, but the difference with the next highest *k* for a given network generally declines with increasing *h* (*k* for vertex that pertains to MC is 2.8 and 1.5 times greater than the next highest *k* for the networks at $h = 8.0$ m). In the overbank-inundation phase, CB is the patch type that has the greatest contribution to *n* of the soil-network for simulations where inundation is mostly restricted to the floodplain ($8.5 \leq h \leq 10.0$ m) and it has a range of 18.5 to 22.0%. FHF contributes the most vertices to *n* for the vegetation-network during these same flows with a range of 17.4 to 21.8%. Upland patch types are the greatest contributors to *n* for their respective networks for simulations with $h \geq 10.5$ m with TSL and upland deciduous woods (UDW) providing 16.7 and 15.5% of the vertices in *n* for the simulation with $h = 11.63$ m. The pattern of *k* is similar to what is exhibited in the some-floodplain-inundation phase with the MC vertex being the largest contributor and it has a value that is 1.3 and 1.1 times greater than the vertex with the next highest *k* for the simulation with $h = 11.63$ m.

We analyzed the distribution of *k* for both networks at each simulation using empirical methods from Broido and Clauset (2019) to determine if the network can be considered to be scale-free. A *k* distribution that follows a power-law is the primary criteria and we fit power-laws to both networks at every state and compared them to fits using four other tail-heavy distributions that include exponential, log-normal, power-law with exponential cutoff (plwc), and Weibull. Likelihood ratio tests (*R*) that directly

compare the power-law fit to one of the other fits indicate that the power-law fit outperforms the other distributions for ≥41% of the network states with the plwc and log-normal fits being the most serious competitors to the power-law (Figures III-4a and III-4f). There is a stochastic nature to *R* and a *p-value* is computed to determine the reliability of these tests. *R* comparing the power-law fits to exponential and Weibull fits are reliable for ≥77% of both network states (Figures III-4b and III-4g), but none of the tests are reliable for the plwc comparisons and ≤23% of the tests for log-normal are considered reliable. A goodness-of-fit test with an associated *p-value* that determines the plausibility of a power-law for the *k* distribution is also used and the plausibility of a power-law for *k* cannot be rejected for ≥73% of all network states (Figures III-4c and III-4h). The secondary part of the Broido and Clauset (2019) analysis involves analyzing the properties of the power-law fit. Scale-free networks tend to be relatively large and the number of vertices on the tail-end of the *k* distribution (n_{tail}) over which the power-law is fit needs to be ≥50 and this occurs for 82% of the network states (Figures III-4d and III-4i). An exponent parameter (α) between 2 and 3 for the power-law fit is also needed for the network to be considered scale-free and this occurs for ≥50% of all network states. The results from this analysis and a classification scheme proposed by Broido and Clauset (2019) indicate that the dynamic soil- and vegetation-networks can be considered as weakly to strongly scale-free. The lack of reliability in *R* for the log-normal and plwc comparisons is the reason for the range in the scale-free classification.

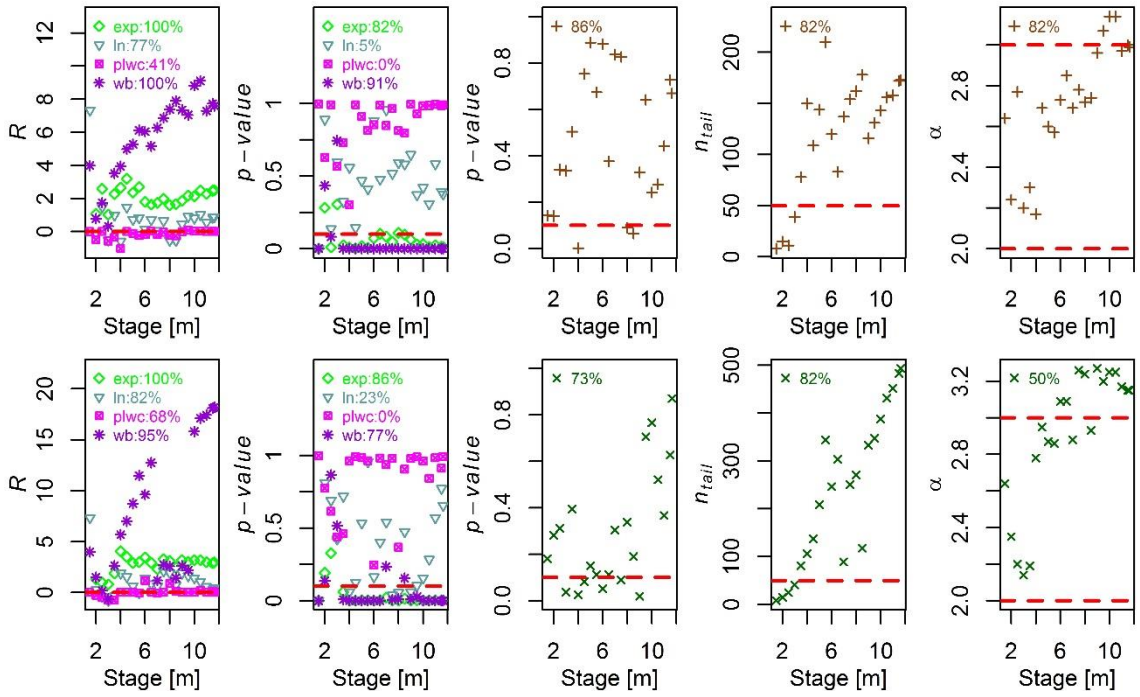

Figure III-4. Empirical analysis determining if the soil- (a-e) and vegetation-networks (f-j) can be considered scale-free using methods from Broido and Clauset (2019). Indicators are calculated for both networks at each that is associated with the 23 flow simulations. a,f) Likelihood ratio test (R) between the fitted power-law distribution and four other tail-heavy distribution (exponential (exp; green diamonds); lognormal (ln; light blue triangles); power-law with exponential cutoff (plwc; magenta squares with x's); and Weibull (wb; purple stars). b,g) P-values for the likelihood ratio tests in (a) and (f). c,h) P-values for goodness-of-fit tests determining the plausibility whether the degree distribution for each of the 23 simulations can come from a power-law distribution. d,i) The number of network vertices in the tail-end/power-law portion of the degree distribution (n_{tail}). ≥ 50 is needed for the network to be considered to come from a scale-free network. e,j) The alpha parameter (α) for the fitted power-law to the network. $2 \leq \alpha \leq 3$ is needed for the network to be considered scale-free. (Note: Percentage values in the legend indicate the fraction of the 23 network states that meet the criteria proposed by Broido and Clauset (2019) in order to be considered scale-free.)

Discussion

Lowland rivers can cause surface-water inundation within their floodplains for a wide range of river flows without most of the main channel banks being overtopped (Tockner et al., 2000, Czuba et al., 2019, Meitzen et al., 2013, Hudson et al., 2013, Phillips, 2013). Mission River is no different and here we describe surface-water inundation in three phases – (1) channel-inundation, (2) some-floodplain-inundation, and

(3) overbank-inundation – with the greatest increases in inundated area (A_I) occurring during the latter half of the some-floodplain-inundation phase (See Figure III-2a). The spatial pattern of surface-water inundation for river flows with stage (h) $\leq$ 4.0 m facilitates these increases in A_I during the some-floodplain-inundation phase because it is driven by surface water backing into the floodplain through tributaries, oxbows/cutoffs, small connector channels, and scroll bars (See Figure B-2).

The pattern of surface-water connections between landscape patches induced by river flows also creates a dynamic network whose growth is largely driven by preferential attachment where newly connected patches tend to become connected to patches that are already connected to a relatively large number of other patches. Growth and generation by preferential attachment is one of the fundamental properties of scale-free graphs/networks (Li et al., 2005, Barabási and Albert, 1999), and in total we found that the our landscape networks exhibit five of the six fundamental properties of scale-free networks described by Li et al. (2005). The second scale-free property we found is that both of our landscape networks exhibit a power-law degree (k) distribution and the fitted power-laws meet some of the more stringent criteria outlined by Broido and Clauset (2019) in order for the networks to be labeled as weakly-to-strongly scale-free with regard to the distribution of k. Third, our landscape networks also contain patches that pertain to the active (main channel and tributaries), semi-active (slow and connector channels), and abandoned channels (cutoffs and oxbows) that act as highly-connected hubs that maintain network-level connectivity. This connectivity is resilient to most random disconnections amongst patches (most patches are not hubs), but also highly

sensitive to disconnections of hub-like patches (disconnecting these patches would also disconnect patches within the floodplain that surround these hubs). Forth, the topological structure of our networks is driven by the distribution of k for the connected patches and not the particular pattern depicting which patches connect to which. This is shown in Figure B-5h where the contribution to the spectral radius (λ_1; the largest eigenvalue of the network adjacency/connectivity matrix) from the distribution of k (ξ_{conn}) is much greater (≥80%) than the contribution from the pattern/wiring of connections (ξ_{wir}) for river flows with $h \geq 3.0$ m. Fifth, our networks of surface-water connections are self-similar in that the topological structure of the networks for patches surrounding channels and other low-lying features is similar with a highly-connected hub driving most of the connectivity (See Figures B-3 and B-4). Moreover, while both the soil- and vegetation-networks are related in their geography and the processes that created them, both networks are distinct (See Figures B-3c - B3f). Nonetheless, both networks exhibited power-law distributions for k and the dynamics of the network properties shown in Figure B-5 are similar.

The sixth fundamental property of scale-free graphs/networks described by Li et al. (2005) is universality in that scale-free networks of surface-water connections should also exist in other lowland river-floodplain landscapes. We cannot make that claim here because our analysis only focused on the lowland river-floodplain landscape of Mission River. On the other hand, similar patterns of riverine surface-water inundation have been documented on the lower Sabine River (Texas/Louisiana border) (Phillips, 2013), lower Brazos River in Texas (Phillips, 2015), and the Guadalupe River in Texas (Hudson et al.,

2012). We propose that more research is needed to determine if scale-free networks of surface-water connections can be found within these types of landscapes.

Some of the most celebrated properties of scale-free networks include growth by preferential attachment (Barabási and Albert, 1999), efficiency in the transfer of information and materials (Crucitti et al., 2003, Pastor-Satorras and Vespignani, 2001), error tolerance (Albert et al., 2000), attack vulnerability (Holme et al., 2002), and emergent synchronization (Restrepo et al., 2006); and four examples below outline how they can be useful in understanding and managing lowland river-floodplain landscapes. First, the type of detailed terrain and hydrodynamic models that we use here are not available for all lowland rivers but knowledge that these types of landscapes can have surface-water connections with scale-free structure can help determine which areas are more susceptible to flooding. This is because some information regarding the surface-water connections for a given river flow will help determine which patches are most likely to become connected for a higher river flow by applying the concept of preferential attachment that dictates newly connected patches are most likely to connect to patches that are already have a relatively large number of connections. Second, ecosystems within river-floodplain landscapes are some of the most threatened on Earth with the rapid invasion and spread of non-native species being one of the dominant factors (Tockner et al., 2010). This has not been aided by the efficiency of transfer noted for scale-free networks, but this type of spreading within scale-free networks has been well-studied (e.g., Pastor-Satorras and Vespignani (2001)) and this knowledge-base can help manage the spread of problematic species. Third, losses in hydrologic connectivity

between a river and its floodplain due to the construction of flow/flood control structures such as levees has been widely documented for these landscapes around the world (e.g., (Poff et al., 1997, Tockner et al., 2000, Tockner et al., 2010)). This has negatively affected the health of river-floodplain ecosystems and it highlights the error tolerance, but targeted attack vulnerability of the scale-free nature of surface-water connections within these landscapes. Landscape-level connectivity from surface-water connections is robust to most random disconnections of patches, but is highly vulnerable to disconnections of one of the hub-like landscape patches (e.g., main and semi-active channels). Forth, the concept of bankfull discharge has traditionally been used differentiate between strictly in-channel and floodplain processes. Bankfull concepts have been questioned recently because hydraulic and geomorphic conditions can vary longitudinally that complicates that application of more localized flow properties to other portion of the floodplain (Hudson et al., 2013, Tockner et al., 2000). Scale-free networks have been found to exhibit emergent synchronization where the elements of a system are operating in unison (Restrepo et al., 2006). The networks from surface-water connections discussed here operate in unison when the landscape can be considered in a state of surface-water connection and this occurs for Mission River at stages ≥4.0 m. The concept of synchronization in surface-water connection within a lowland river-floodplain landscape can be used in-place of the bankfull concept because it more of a landscape/reach level estimate and not a locale estimate applied to a river reach/landscape.

Power/scaling-laws have been widely used within the fields of hydrology and fluvial geomorphology to understand in-channel hydraulic geometry (Leopold and Maddock, 1953), hydrologic responses at the watershed-level to intense rainfall events (Gupta et al., 2010, Mantilla et al., 2006, Furey and Gupta, 2007), patterns of dendritic drainage networks (Rodriguez-Iturbe et al., 1992, Rinaldo et al., 2006, Rinaldo et al., 1992, Rodríguez-Iturbe et al., 1992), and the pattern of topologic depressions within floodplains and wetlands (Le and Kumar, 2014, Bertassello et al., 2018). These power/scaling relationships describe pattern and process in fluvial landscapes and here we contribute to this list of scaling relationships by proposing that the interaction of surface-water with the landscape patches of lowland river-floodplain landscapes can also be described using scaling relationships.

References

ALBERT, R., JEONG, H. & BARABÁSI, A. L. 2000. Error and attack tolerance of complex networks. Nature, 406, 378-382.

BARABÁSI, A. L. & ALBERT, R. 1999. Emergence of scaling in random networks. Science, 286, 509-512.

BERTASSELLO, L. E., RAO, P. S. C., JAWITZ, J. W., BOTTER, G., LE, P. V. V., KUMAR, P. & AUBENEAU, A. F. 2018. Wetlandscape Fractal Topography. Geophysical Research Letters, 45, 6983-6991.

BROIDO, A. D. & CLAUSET, A. 2019. Scale-free networks are rare. Nature Communications, 10, 1-10.

BRUNNER, G. W. 2016. HEC-RAS: River Analysis System, 2D Modeling User's Manual Version 5.0. Davis, CA: Hydrologic Engineering Center - U.S. Army Corp of Engineers.

CLAUSET, A., SHALIZI, C. R. & NEWMAN, M. E. J. 2009. Power-law distributions in empirical data. SIAM Review, 51, 661-703.

CRUCITTI, P., LATORA, V., MARCHIORI, M. & RAPISARDA, A. 2003. Efficiency of scale-free networks: Error and attack tolerance. Physica A: Statistical Mechanics and its Applications, 320, 622-642.

CZUBA, J. A., DAVID, S. R., EDMONDS, D. A. & WARD, A. S. 2019. Dynamics of Surface-Water Connectivity in a Low-Gradient Meandering River Floodplain. Water Resources Research, 55, 1849-1870.

ELLIOTT, L. F., TREUER-KUEHN, A., BLODGETT, C. F., TRUE, C. D., GERMAN, D. & DIAMOND, D. D. 2014. Ecological System of Texas: 391 Mapped Types. In: TEXAS PARKS AND WILDLIFE DEPARTMENT & TEXAS WATER DEVELOPMENT BOARD (eds.). Austin, TX.

FEMA 2014. Flood Insurance Study: Refugio County, Texas and Incorporated Areas. Flood Insurance Studies. Denton, TX: Federal Emergency Management Agency.

FUREY, P. R. & GUPTA, V. K. 2007. Diagnosing peak-discharge power laws observed in rainfall-runoff events in Goodwin Creek experimental watershed. Advances in Water Resources, 30, 2387-2399.

GUPTA, V. K., MANTILLA, R., TROUTMAN, B. M., DAWDY, D. & KRAJEWSKI, W. F. 2010. Generalizing a nonlinear geophysical flood theory to medium-sized river networks. Geophysical Research Letters, 37, 1-6.

HECKMANN, T., SCHWANGHART, W. & PHILLIPS, J. D. 2015. Graph theory-Recent developments of its application in geomorphology. Geomorphology, 243, 130-146.

HOLME, P. 2019. Rare and everywhere: Perspectives on scale-free networks. Nature Communications, 10, 1-3.

HOLME, P., KIM, B. J., YOON, C. N. & HAN, S. K. 2002. Attack vulnerability of complex networks. Physical Review E - Statistical, Nonlinear, and Soft Matter Physics, 65, 056109/1-056109/14.

HUDSON, P. F., HEITMULLER, F. T. & LEITCH, M. B. 2012. Hydrologic connectivity of oxbow lakes along the lower Guadalupe River, Texas: The influence of geomorphic and climatic controls on the " flood pulse concept". Journal of Hydrology, 414-415, 174-183.

HUDSON, P. F., SOUNNY-SLITTINE, M. A. & LAFEVOR, M. 2013. A new longitudinal approach to assess hydrologic connectivity: Embanked floodplain inundation along the lower Mississippi River. Hydrological Processes, 27, 2187-2196.

JUNK, W. J., BAYLEY, P. B. & SPARKS, E. 1989. The floodpulse concept in river-floodplain systems. Canadian Journal of Fisheries and Aquatic Sciences Special Publication, 110-127.

KUPFER, J. A., MEITZEN, K. M. & GAO, P. 2014. Flooding and surface connectivity of Taxodium-Nyssa stands in a southern floodplain forest ecosystem. River Research and Applications, 1-12.

LE, P. V. V. & KUMAR, P. 2014. Power law scaling of topographic depressions and their hydrologic connectivity. Geophysical Research Letters, 41, 1553-1559.

LEGLEITER, C. J. & KYRIAKIDIS, P. C. 2008. Spatial prediction of river channel topography by kriging. Earth Surface Processes and Landforms, 33, 841-867.

LEOPOLD, L. B. & MADDOCK, T. 1953. The Hydraulic Geometry of Stream Channels and Some Physiographic Implications. Geological Survey Professional Paper, 1-64.

LI, L., ALDERSON, D., DOYLE, J. C. & WILLINGER, W. 2005. Towards a theory of scale-free graphs: Definition, properties, and implications. Internet Mathematics, 2, 431-523.

MANTILLA, R., GUPTA, V. K. & J. MESA, O. 2006. Role of coupled flow dynamics and real network structures on Hortonian scaling of peak flows. Journal of Hydrology, 322, 155-167.

MEITZEN, K. M., DOYLE, M. W., THOMS, M. C. & BURNS, C. E. 2013. Geomorphology within the interdisciplinary science of environmental flows. Geomorphology, 200, 143-154.

NEWMAN, M. E. J. 2003. The structure and function of complex networks. SIAM Review, 45, 167-256.

PASTOR-SATORRAS, R. & VESPIGNANI, A. 2001. Epidemic spreading in scale-free networks. Physical Review Letters, 86, 3200-3203.

PHILLIPS, J. D. 2012. Synchronization and scale in geomorphic systems. Geomorphology, 137, 150-158.

PHILLIPS, J. D. 2013. Hydrological connectivity of abandoned channel water bodies on a coastal plain river. River Research and Applications, 29, 149-160.

PHILLIPS, J. D. 2015. Hydrologic and geomorphic flow thresholds in the Lower Brazos River, Texas, USA. Hydrological Sciences Journal, 60, 1631-1648.

PHILLIPS, J. D., SCHWANGHART, W. & HECKMANN, T. 2015. Graph theory in the geosciences. Earth-Science Reviews, 143, 147-160.

POFF, N. L., ALLAN, J. D., BAIN, M. B., KARR, J. R., PRESTEGAARD, K. L., RICHTER, B. D., SPARKS, R. E. & STROMBERG, J. C. 1997. The natural flow regime: A paradigm for river conservation and restoration. BioScience, 47, 769-784.

POOLE, G. C. 2002. Fluvial landscape ecology: Addressing uniqueness within the river discontinuum. Freshwater Biology, 47, 641-660.

PRINGLE, C. M. 2001. Hydrologic connectivity and the management of biological reserves: A global perspective. Ecological Applications, 11, 981-998.

RAYFIELD, B., FORTIN, M. J. & FALL, A. 2011. Connectivity for conservation: A framework to classify network measures. Ecology, 92, 847-858.

RESTREPO, J. G., OTT, E. & HUNT, B. R. 2006. Emergence of synchronization in complex networks of interacting dynamical systems. Physica D: Nonlinear Phenomena, 224, 114-122.

RINALDO, A., BANAVAR, J. R. & MARITAN, A. 2006. Trees, networks, and hydrology. Water Resources Research, 42, 1-19.

RINALDO, A., RODRIGUEZ-ITURBE, I., RIGON, R., BRAS, R. L., IJJASZ-VASQUEZ, E. & MARANI, A. 1992. Minimum energy and fractal structures of drainage networks. Water Resources Research, 28, 2183-2195.

RODRÍGUEZ-ITURBE, I., IJJÁSZ-VÁSQUEZ, E. J., BRAS, R. L. & TARBOTON, D. G. 1992. Power law distributions of discharge mass and energy in river basins. Water Resources Research, 28, 1089-1093.

RODRIGUEZ-ITURBE, I., RINALDO, A., RIGON, R., BRAS, R. L., IJJASZ-VASQUEZ, E. & MARANI, A. 1992. Fractal structures as least energy patterns: The case of river networks. Geophysical Research Letters, 19, 889-892.

STANFORD, J. A. & WARD, J. V. 1993. An Ecosystem Perspective of Alluvial Rivers: Connectivity and the Hyporheic Corridor. Journal of the North American Benthological Society, 12, 48-60.

TOCKNER, K., MALARD, F. & WARD, J. V. 2000. An extension of the flood pulse concept. Hydrological Processes, 14, 2861-2883.

TOCKNER, K., PUSCH, M., BORCHARDT, D. & LORANG, M. S. 2010. Multiple stressors in coupled river-floodplain ecosystems. Freshwater Biology, 55, 135-151.

WANG, X. F. & CHEN, G. 2003. Complex networks: Small-world, scale-free and beyond. IEEE Circuits and Systems Magazine, 3, 6-20.

CHAPTER IV

MONITORING SURFACE-WATER CONNECTIVITY DYNAMICS IN A COASTAL LOWLAND RIVER USING FIELD-BASED DATA LOGGERS

Introduction

Hydrologic and geomorphic interactions between a river and the landscape through which it flows will vary with the hydrologic regime (climate, groundwater exchange, antecedent moisture conditions, anthropogenic water-use), the regional morphology (geological template, base-level, flow control structures), the localized morphology (planform and cross-section profile of the channel-floodplain system, soil properties, land cover), and other place-specific factors that can influence flow conditions (e.g., tides and storm-surge for coastal rivers). These interactions are often analyzed using the hydrologic connectivity concept – the water mediated transfer of energy, matter, biota, and information between the riverine landscape (Amoros and Roux, 1988, Wohl, 2017) – that is generally applied over one or more of the dimensions generally used in river science that include time and the spatial dimensions of longitudinal (upstream-downstream), lateral (orthogonal to the trend of the thalweg or valley), and vertical (height above and/or below the channel bed). While these concepts have been used across the spectrum of river-types (Wohl, 2017, Wohl et al., 2018), hydrologic connectivity has particularly been an important contribution to the understanding of hydrologic, geomorphic, and ecological processes within lowland rivers (Hudson et al., 2013). This is why hydrologic connectivity between a lowland

river and the surrounding landscape has commonly been used as an indicator of habitat health (Ishiyama et al., 2014) and is often a consideration in environmental flow policies and management schemes (Hudson et al., 2013, Meitzen et al., 2013, Wohl, 2017).

Connectivity within the context of river science has been determined within the literature using measurements (direct and remote) and inferences that are established using a variety of methods (Wohl, 2017). Among field-based methods, inferences of the presence/absence (or intermittence) of water that rely on records from field-deployed data loggers that measure ambient environmental variables have been gaining interest within the literature (Chapin et al., 2014). Data loggers that record *in-situ* measurements of ambient temperature and/or electrical resistance within riverine and wetland environments being the most widely used (Chapin et al., 2014). Water temperature and electrical conductivity (inverse of electrical resistance) are widely used ecological indicators (Chapin et al., 2014, Poole, 2002); and they can be useful in determining the source of the inundating surface-waters (e.g., groundwater, glacial/snow melt, or rainfall were found to be the stream water sources in Paillex et al. (2019)), the duration of inundation (e.g., the duration of inundation for various peatlands was determined by Goulsbra et al. (2009)), the suitability of channel reaches as habitat for specific species (e.g., Jaeger and Olden (2012) determined the prevalence of refuge habitats within a set of ephemeral channels) and how the inferred flow intermittency affects aquatic food webs (Siebers et al. (2019) analyzed how changing flow intermittency in alpine streams has affected aquatic trophic levels and biodiversity).

Analyses of flow intermittence and how it relates to changes in hydrologic connectivity over time with field-based data loggers have been conducted in a variety of physiographic environments. Point-based studies have used field-based data loggers to quantify hydrologic connectivity at a point within ephemeral channels in montane regions of the southwestern U.S. with arid (Blasch et al., 2002) and semi-arid (Chapin et al., 2014) climates; as well as in the Canadian High Arctic (Gillman et al., 2017). Vertical hydrologic connectivity at a point within the hyporheic zone of a channel stream bed has also been quantified in an ephemeral stream of southern Arizona using field-based data loggers (Blasch et al., 2004). While estimates at a single point in space have been useful in better understanding process in ephemeral stream channels, the true power in using field-based data loggers is when several data loggers that are deployed at multiple locations are used in conjunction to analyze a channel reach or set of reaches. Longitudinal analyses with data loggers deployed upstream and downstream of each other are what appear most often within the literature where they have been applied within ephemeral channels in the southwestern U.S. in arid-to-semiarid environments of New Mexico and Nevada (Constantz et al., 2001), Arizona (Jaeger and Olden, 2012); environments with temperate climate in the U.S. Appalachians (Jensen et al., 2019) and Europe that include a montane catchment in Luxenberg (Kaplan et al., 2019) and a peatland catchment in the United Kingdom (Goulsbra et al., 2009); and in gullies and ephemeral channels within the relatively flat agricultural regions of southwestern Ontario (Bhamjee and Lindsay, 2011). Researchers have found utility in the use of field-based data loggers, but there are numerous research gaps in their use that are yet to be

explored. In particular, flow intermittency using low-cost data loggers in lowland and coastal streams has not been pursued in the literature. Furthermore, the use of data loggers along the vertical and lateral dimensions has not been fully explored. Along the vertical dimension, some studies have been performed that analyze hydrologic connections between the channel bed surface and hyporheic water that is below the stream bed, but no studies have been performed that analyze connectivity for portions of a channel above the bed surface that experience inundation more intermittently than the bed. For the lateral dimension, no studies have explicitly used data loggers to analyze how flow widths vary along one or more portions of a channel reach.

In this work, we develop multiple Stream Temperature, Intermittency, and Conductivity loggers (STICLs) proposed by Chapin et al. (2014) and deploy them in the field to analyze temporal changes to hydrologic connectivity induced by surface water (surface-water connectivity, hereafter) in the longitudinal, lateral, and vertical dimensions for the channel and floodplain surrounding the lowland Mission River on the Coastal Bend of Texas. We have two main objectives and they include (1) determining the efficacy with which STICLs can be used to monitor surface-water connectivity in portions of a channel and floodplain that experience intermittent inundation for a coastal lowland river; and (2) determine how differences in the hydrologic regime and morphology affect the variations in surface-water connectivity for these areas that experience intermittent inundation. We address these objectives by developing and deploying sets of STICLs in the field and analyzing flow intermittence within five distinct time-periods (TPs).

Study Area

Our study focuses on a 15 km stretch of the Mission River and its lowland floodplain near the Town of Refugio (Refugio, hereafter) on the Coastal Bend of Texas (Figure IV-1). The lowland floodplain lies within the flat coastal plain with the most downstream portions of the study area being ~22 river-km upstream from the outlet at Mission Bay. Two perennial tributaries (Dry and La Rosa creeks) have their confluence with the main channel along our study reach. Floodplain hardwood forest, floodplain Live Oak forest, and floodplain scrub/shrubs are the dominant vegetation communities adjacent to the active channels with sandy loam and clayey loam being the dominant soil types (Elliott et al., 2014). Elevation within the study area ranges from -3 to 17 m (North American Vertical Datum of 1988, NAVD88) with the lowest elevations found within active channels and the highest elevations found in bluffs around Refugio (Figure IV-1d). The main channel of Mission River has a meandering planform with increasing sinuosity in the downstream direction and a longitudinal bed slope of 0.23 mm/m for the entire study reach. Although, the river flows through two distinct geologic units with upstream portions of the floodplain being Pleistocene fluviatile terraces and downstream portions being Holocene alluvium (USGS-TWSC, 2014). The differing geologic controls make for markedly different longitudinal bed slopes with the fluviatile terrace and alluvium portions having bed slopes of 0.39 and 0.16 mm/m, respectively.

The region containing the study reach has a subhumid-to-semiarid subtropical climate with extreme variability in precipitation (Davis and Smith, 2013, Fulbright et al., 1990, Norwine and John, 2007). Mean annual precipitation is 1016 mm with most

precipitation generally occurring in the early-Fall and late-Spring that are caused by large thunderstorm cells. Although, the region is occasionally affected by tropical cyclones that produce large amounts of rainfall with the most recent of which being Hurricane Harvey. With regard to streamflows, mean daily discharge (Q) at the U.S. Geological Survey (USGS) gaging station at Refugio (Gage ID: 08189500; see Figure IV-1) ranged from 0 to 1903 m^3/s with a mean of 3.4 m^3/s (USGS, 2016). The distribution for annual peak *Q* is also extremely skewed (Schoenbaechler and Guthrie, 2011), with a range of 1 to 2237 m^3/s. Similarly, the distribution of stage (*h*) is skewed with a range of 0.8 to 10.2 m and 1 to 12 m for mean daily and annual peak *h*, respectively (USGS, 2016). Portions of the floodplain begin to experience flood inundation at a *Q* of 30 m^3/s due to backwater flooding into tributaries, sloughs, and swales within meander scroll-bars (Castillo et al., In-Preperation). Most of the main channel banks and natural levees get overtopped at a $Q \geq 285$ m^3/s with the entire floodplain becoming a continuous water-surface at a $Q \geq 1169$ m^3/s (Castillo et al., In-Preperation). Moreover, the lower half of the study reach is influenced by tidal processes and storm surge (Davis and Smith, 2013, Nelson and Tolan, 2008, FEMA, 2014), that can also experience significant inundation during tropical storms/cyclones with Hurricane Harvey being no exception.

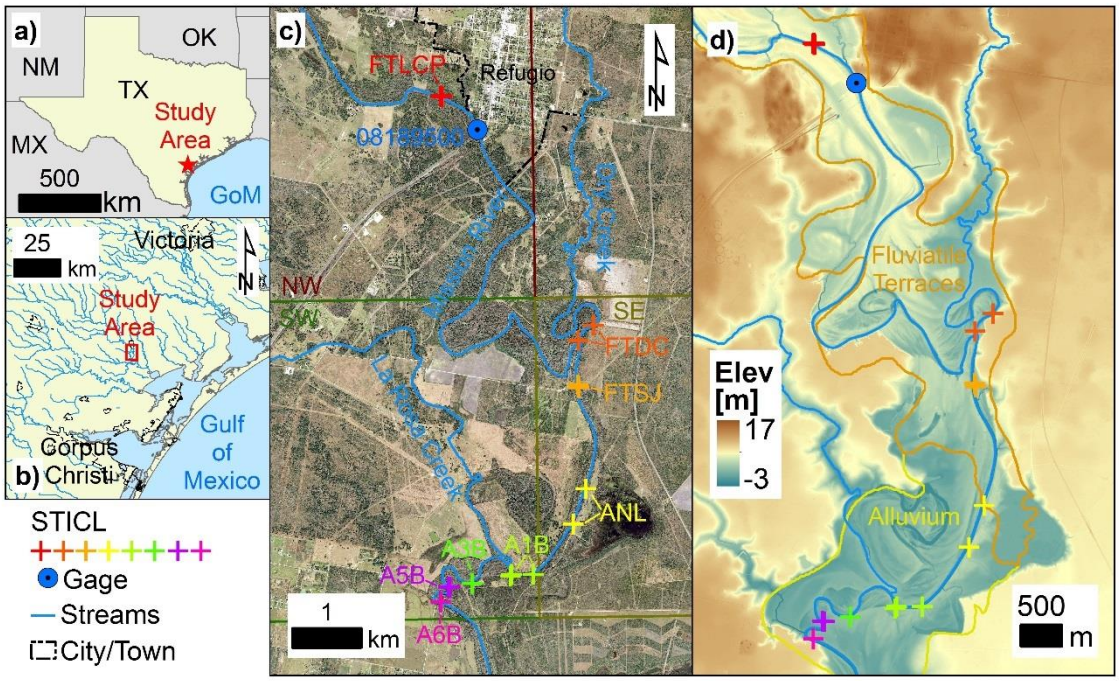

Figure IV-1. a) Map showing where the study area lies within the State of Texas. b) Regional map showing where the study area lies within the Coastal Bend Region of Texas. c) Map showing the study reach of Mission River and its floodplain. The eight locations where Stream Temperature, Intermittency, and Conductivity loggers (STICLs) were installed are shown (colored +) along with the location of the 08189500 U.S. Geological Survey gaging station (blue bulls-eye) and the three Parameter-elevation Regressions on independent Slopes Model (PRISM) grid cells (colored borders). Aerial imagery is a mosaic of StratMap imagery collected in late-March of 2016 (SARA, 2016). d) Map showing the lidar-derived digital terrain model at 1-m spatial resolution of the study area/reach and the geologic units within the floodplain. Geologic units were extracted from the Geologic Database of Texas (USGS-TWSC, 2014). (Note: FTLCP = fluviatile terraces-Lions City Park; FTDC = fluviatile terraces-Dry Creek; FTSJ = fluviatile terraces-Saint John; ANL = alluvium-natural levee; A1B = alluvium-first bend; A3B = alluvium-third bend; A5B = alluvium-fifth bend; A6B = alluvium-sixth bend; NW = Northwest PRISM grid cell; SW = Southwest PRISM grid cell; and SE = Southeast PRISM grid cell)

The STICLs we use in our analysis are installed in eight different locations along the eastern banks of Mission River and lower portions of Dry Creek where we were provided access by local landowners (Figures IV-1 and IV-2). Our three most upstream locations lie within the Pleistocene fluviatile terraces portion of the floodplain and they are fluviatile terraces-Lions City Park (FTLCP), fluviatile terraces-Dry Creek (FTDC), and fluviatile terraces-Saint John's (FTSJ). FTLCP is within a floodplain hardwood

forest portion of Lions City Park of Refugio on a steep portion of the eastern bank of the main channel (Figure IV-2b). Soils are a loamy sand and this portion of the main channel reach has an alternating bar morphology with a low sinuosity planform. FTDC is two locations within the Fennessey Ranch portion of the Mission Aransas National Estuarine Research Reserve on the eastern banks of Dry Creek just upstream of its confluence with Mission River (Figures IV-2c and IV-2d). These portions of the floodplain regularly experience backwater flooding from Mission River (Castillo et al., In-Preperation, FEMA, 2014). The most upstream FTDC location is ~500 m upstream of the Mission River-Dry Creek confluence near the valley wall with the vertical profile containing a relatively shallow channel and bench within a mixed floodplain hardwood-Live Oak forest land cover. The downstream FTDC location is on a small point-bar that is ~100 m upstream of the Mission River-Dry Creek confluence in a location farther from the valley wall with a floodplain Live Oak forest land cover. Soils for both FTDC locations are clayey loam and the planforms for both Dry Creek and Mission River are confined meanders due to the proximity with the valley wall. FTSJ is two locations within and just south of the Saint John's gas pipeline river crossing in Fennessey Ranch (Figure IV-2e). The most upstream FTSJ location is within the linear clearing of the pipeline crossing in a steep portion of the eastern bank of Mission River with a floodplain grassland landcover. The other FTSJ location is ~50 m downstream on the floodplain of the main channel with a mixed landcover that contains both floodplain shrub/scrub and hardwood forest. Soils at both FTSJ locations are sandy loam with a low

sinuosity planform for the main channel and a morphology that has been modified by the pipeline crossing and cattle grazing that occurs at both locations.

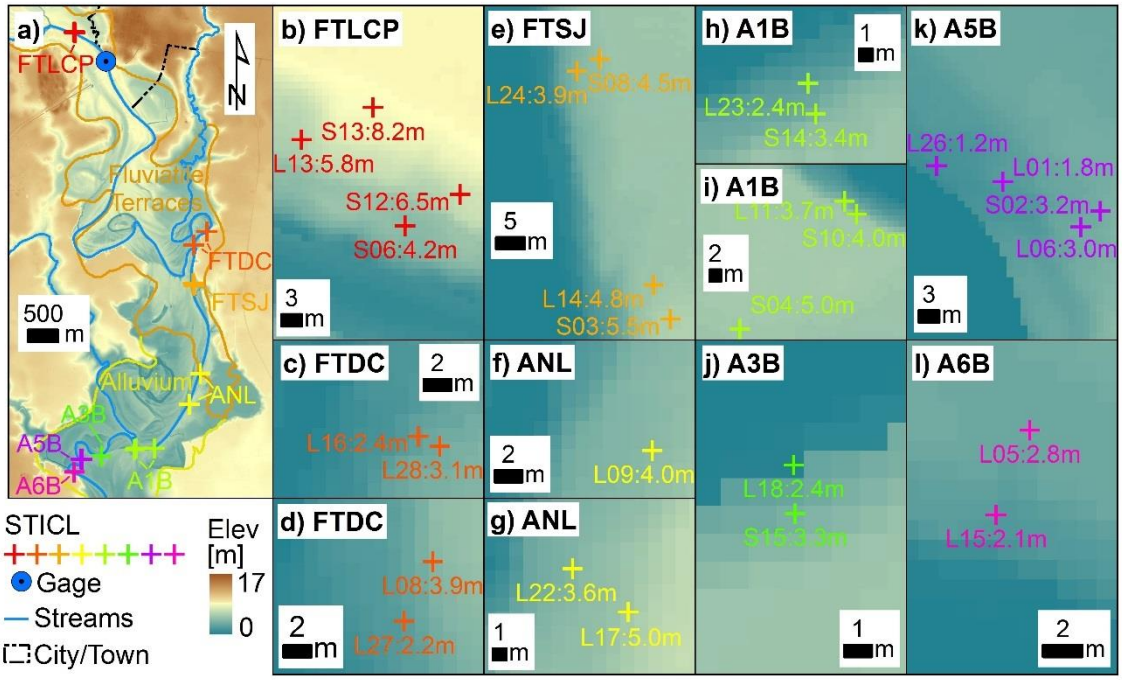

Figure IV-2. Terrain for the locations at which the STICLs were deployed. Terrain data was collected as part of a RAPID-NSF project and prepared as part of the analysis performed in Castillo et al. (In-Preperation). a) Map showing the terrain and floodplain geology for our eight locations at which STICLs were installed (labeling for each location has distinct colors). b) Terrain where the four STICLs were deployed at the fluviatile terrace-Lions City Park (FTLCP) location. c) Terrain where the two STICLs were deployed at the upstream fluviatile terrace-Dry Creek (FTDC) location. d) Terrain where the two STICLs were deployed at the downstream FTDC location. e) Terrain where the four STICLs deployed at the fluviatile terrace-Saint John's (FTSJ) location. f) Terrain where the STICL deployed at the upstream alluvium-natural levee (ANL) location. g) Terrain where the two STICLs were deployed at the downstream ANL location. h) Terrain where the two STICLs were deployed at the upstream alluvium-first bend (A1B) location. i) Terrain where the three STICLs were deployed at the downstream A1B location. j) Terrain where the two STICLs were deployed at the alluvium-third bend (A3B) location. k) Terrain where the four STICLs were deployed at the alluvium-fifth bend (A5B) location. k) Terrain where the two STICLs were deployed at the alluvium-sixth bend (A6B) location. (Note: the ID for each logger is followed by the elevation at which each STICL was installed using NAVD88).

Our five downstream locations lie within Fennessey Ranch in the Holocene alluvium portion of the floodplain (Figures IV-1 and IV-2) and they are alluvium-natural levee (ANL), alluvium-first bend (A1B), alluvium-third bend (A3B), alluvium-fifth bend

(A5B), and alluvium-sixth bend (A6B). ANL is a prominent natural levee within Fennessey Ranch with a floodplain hardwood forest landcover. We have two ANL locations with the most upstream location being a portion where the natural levee has an undulating vertical profile (i.e., multiple ridges) with our STICL positioned on a relatively flat portion of the levee just east of the active channel (Figure IV-2f). Our second ANL location is ~600 m downstream on a steeper portion of the natural levee where the vertical profile only has a single ridge (Figure IV-2g). Soils at both ANL locations are a sandy loam with the main channel planform exhibiting a low sinuosity bend. A1B is a cut bank with a floodplain hardwood forest and floodplain grassland landcover on the first of a set of bends in the downstream portions of our study area. We have two A1B locations with the most upstream location being upstream of the bend apex on the linear clearing of a gas pipeline crossing where the profile of the cut bank is steep but not completely vertical (Figure IV-2h). Our second A1B location is ~300 m downstream of the other A1B location on a portion of the cut bank with a cliff-like vertical profile that lies downstream of the bend apex (Figure IV-2i). This portion of the cut bank is adjacent to an unpaved road. Soils at both A1B locations are sandy loam and the planform for the main channel exhibits an intermediate sinuosity. A3B is on the third of a set of bends in downstream portions of the study area (Figure IV-2j). The A3B location is near the apex of the bend with an almost cliff-like vertical profile and a floodplain hardwood forest landcover. Soils are a sandy loam and the main channel has a planform with symmetrical bend sinuosity. A5B is a location just upstream of the cut bank for the fifth (and smallest) of a set of bends in downstream portions of the study

area (Figure IV-2k). The A5B location has a vertical profile with a moderate slope and the landcover is floodplain hardwood forest. Soils are sandy loam and the planform of the main channel is a symmetrical bend sinuosity. A6B is on the downstream end of the point-bar of the sixth bend in the aforementioned set of bends. A6B is also the most downstream location within our study area (Figure IV-2l) and it has a floodplain hardwood forest landcover. Loggers were installed on a relatively flat portion of the floodplain adjacent to the channel. Soils are sandy loam and the planform of the main channel has a skewed sinuosity due to the west bank at the A6B location being along the valley wall.

Data and Methods

Data

Our primary dataset is a set of time-series with readings offloaded from our 28 STICLs deployed in the field at the eight locations described in Study Area and Figure IV-2. The number of operational STICLs deployed at each location differs by time-period (TP). The STICLs and locations included in each TP is shown in Table IV-1. Our STICLs were set to record readings on a 15-minute interval that allows them to be compared to instantaneous streamflow data. Data on ambient temperature and calibrated electrical conductivity (EC; See Logger Calibration) are recorded by each logger, but we only use the EC here.

Table IV-1. Descriptions of the five time-periods (TP) included in our analysis. The locations and maximum number of data points ($n_{log,max}$) a STICL can provide during this TP are also shown; as well as the precipitation (PPT) stations that pertain to each location and STICL preparations phase area also shown. (Note: FTLCP = fluviatile terraces-Lions City Park; FTDC = fluviatile terraces-Dry Creek; FTSJ = fluviatile terraces-Saint John; ANL = alluvium-natural levee; A1B = alluvium-first bend; A3B = alluvium-third bend; A5B = alluvium-fifth bend; A6B = alluvium-sixth bend).

TP	Dates	$n_{log,max}$	Location	PPT Station	STICL Prep Phase	Data Logger IDs
TP1	2016-05-25 to 2016-08-23	8,736	FTLCP	NW	1	S06, S12, and S13
			FTSJ	SE	1	S08 and S03
			A1B	SW	1	S14, S10, and S04
			A5B	SW	1	S02
TP2	2016-08-25 to 2017-03-17	19,688	FTLCP	NW	1	S06, S12, and S13
			FTSJ	SE	1	S08 and S03
			A1B	SW	1	S04
TP3	2017-03-19 to 2017-07-13	11,232	FTLCP	NW	1	S06 and S13
			FTSJ	SE	1	S08 and S03
			A1B	SW	1	S04
TP4	2017-07-14 to 2018-02-20	21,324	FTLCP	NW	1 and 2	S06, L13, and S13
			FTDC	SE	2	L27, L16, L28, and L08
			FTSJ	SE	2	L24, L14, S08, and S03
			ANL	SE	2	L22, L09, and L17
			A1B	NW	2	L23 and L11
			A3B	NW	2	L18 and S15
			A5B	NW	2	L26, L01, and L06
			A6B	NW	2	L15 and L05
TP5	2018-02-21 to 2018-12-31	30,048	FTDC	SE	2	L08
			FTSJ	SE	1 and 2	S08, L14, and S03
			A1B	SW	1	S04
			A6B	SW	2	L15 and L05

We use daily precipitation (*PPT*) accumulations from the Parameter-elevation Regressions on independent Slopes Model (PRISM) dataset (PRISM Climate Group) to represent the hydrometeorological regime in our analysis. The PRISM data is in gridded format with grid cells having a spatial resolution of ~4 km and three grid cells overly the locations at which our sets of STICLs were deployed (Figure IV-1). We treat each of these three grid cells as a *PPT* station and label them as the northwest (NW), southeast

(SE), and southwest (SW) stations. We generated a time-series of *PPT* for each station by creating an image stack for all dates considered here. We divide the three daily *PPT* time-series into five datasets (Table IV-2) that coincide with the five sets of data recorded by our STICLs. TP1 received the least amount of *PPT* with most occurring in June and August (Figure IV-3). TP2 received the second most amount of *PPT* with one storm in early-December being the largest *PPT* event (Figure IV-4). TP3 received the second least amount of *PPT* with most *PPT* occurring in June (Figure IV-5). TP4 is the third wettest period being considered with the vast majority of *PPT* occurring during Hurricane Harvey that passed through the study area in late-August (Figure IV-6). TP5 is the wettest period being considered with more than two times the total *PPT* than TP2 with most *PPT* occurring during a very large event in June and a string of events that occurred in the Fall months (Figure IV-7).

We use instantaneous streamflow records (15-minute sampling interval) for the 08189500 USGS gaging station at Refugio, TX from May-2016 through Dec-2018 to represent the streamflow regime in our analysis. Following the approach used for the time-series from our STICLs and precipitation, we divide the streamflows from this time-period into five datasets (Table IV-3) that coincide with the five sets of data recorded by our STICLs. These TPs vary with regard to their length and hydrologic conditions (Table IV-3). TP1 is the period with the third lowest variance for the set of streamflows with one relatively large streamflow in early-June where discharge (Q) peaked at 69 m^3/s (Figure IV-3). TP2 is the period with the second lowest variance for the set of streamflows with two modest flow pulses and the larger one in late-February

reaching a peak *Q* of 29 m^3/s (Figure IV-4). TP3 is the period with the lowest variance for the set of streamflows with only one small flow pulse with a peak *Q* of 7.7 m^3/s (Figure IV-5). TP4 is the period with the second highest variance for the set of streamflows with one large streamflow event that resulted from Hurricane Harvey in late-August with a peak *Q* of 130 m^3/s (Figure IV-6). TP5 is the period with the highest variance for the set of streamflows with one very large streamflow event with a peak *Q* of 295 m^3/s in late-June and four other notable streamflow events in the Fall months (Figure IV-7).

Table IV-2. Descriptive statistics of daily PRISM precipitation (PPT) accumulations for the five time-periods (TP) organized by the three precipitation stations (northwest grid cell (NW), southeast grid cell (SE), southwest grid cell (SW)). The statistics are for PPT days which are for days within the TP where precipitation is greater than zero. (Note: n = sample size or number of days in TP; n_{ppt} = count of days in TP with precipitation; Min_{ppt} = is the minimum amount of precipitation for days that had precipitation; Max_{ppt} = is the maximum amount of precipitation for days that had precipitation; μ_{ppt} = is the mean precipitation for days estimated to have precipitation; σ_{ppt} = is the standard deviation of precipitation for days estimated to have precipitation; and Total = is the total amount of precipitation within the grid cell for the TP).

TP	Dates	n	Station	PPT Days (accumulations in mm)					
				n_{ppt}	Min_{ppt}	Max_{ppt}	μ_{ppt}	σ_{ppt}	*Total*
TP1	2016-05-25 to 2016-08-23	91	NW	32	0.01	37.21	10.04	11.48	301.27
			SE	34	0.00	30.92	6.98	7.99	237.36
			SW	32	0.00	35.61	8.36	9.80	267.63
TP2	2016-08-25 to 2017-03-17	205	NW	71	0.01	65.15	7.03	11.13	492.22
			SE	74	0.01	62.19	7.00	11.10	518.36
			SW	71	0.00	65.89	7.18	11.47	510.00
TP3	2017-03-19 to 2017-07-13	117	NW	30	0.01	32.16	9.25	10.51	277.44
			SE	28	0.01	32.16	9.52	10.09	266.47
			SW	30	0.00	30.34	9.24	9.87	277.18
TP4	2017-07-14 to 2018-02-20	222	NW	75	0.00	156.89	6.45	18.99	483.81
			SE	76	0.00	159.49	6.69	18.95	508.36
			SW	75	0.00	149.19	6.38	17.91	478.54
TP5	2018-02-21 to 2018-12-31	314	NW	110	0.00	193.43	11.28	24.34	1263.85
			SE	112	0.01	98.41	9.81	17.85	1099.00
			SW	110	0.01	151.00	11.01	21.95	1210.74

Table IV-3. Descriptive statistics of the instantaneous stage (*h*) and discharge (*Q*) at the 08189500 USGS gaging station that represent the streamflows included in each time-period (TP). (Note: n = sample size streamflows for the TP; Min = minimum value in the sample; Q1 = first quantile for the sample; Q2 = second quantile for the sample; Q3 = third quantile for the sample; Max = maximum value for the sample; μ = mean value for the sample, σ = standard deviation for the sample)

TP	Dates	*n*	Variable	*Min*	*Q1*	*Q2*	*Q3*	*Max*	μ	σ
TP1	2016-05-25 to 2016-08-23	8,736	*h* [m]	0.63	0.67	0.70	0.80	4.92	0.88	0.58
			Q [m^3/s]	0.03	0.13	0.25	0.75	69.09	2.47	8.42
TP2	2016-08-25 to 2017-03-17	19,688	*h* [m]	0.61	0.64	0.67	0.71	2.94	0.72	0.24
			Q [m^3/s]	0.02	0.07	0.15	0.29	29.45	0.68	2.74
TP3	2017-03-19 to 2017-07-13	11,232	*h* [m]	0.55	0.61	0.64	0.66	1.46	0.64	0.08
			Q [m^3/s]	0.00	0.03	0.07	0.15	7.56	0.17	0.52
TP4	2017-07-14 to 2018-02-20	21,324	*h* [m]	0.52	0.70	0.71	0.77	7.75	0.90	0.94
			Q [m^3/s]	0.00	0.13	0.16	0.58	129.7	2.87	13.59
TP5	2018-02-21 to 2018-12-31	30,048	*h* [m]	0.59	0.68	0.77	1.02	8.55	1.26	1.35
			Q [m^3/s]	0.00	0.14	0.45	2.45	294.5	8.08	27.59

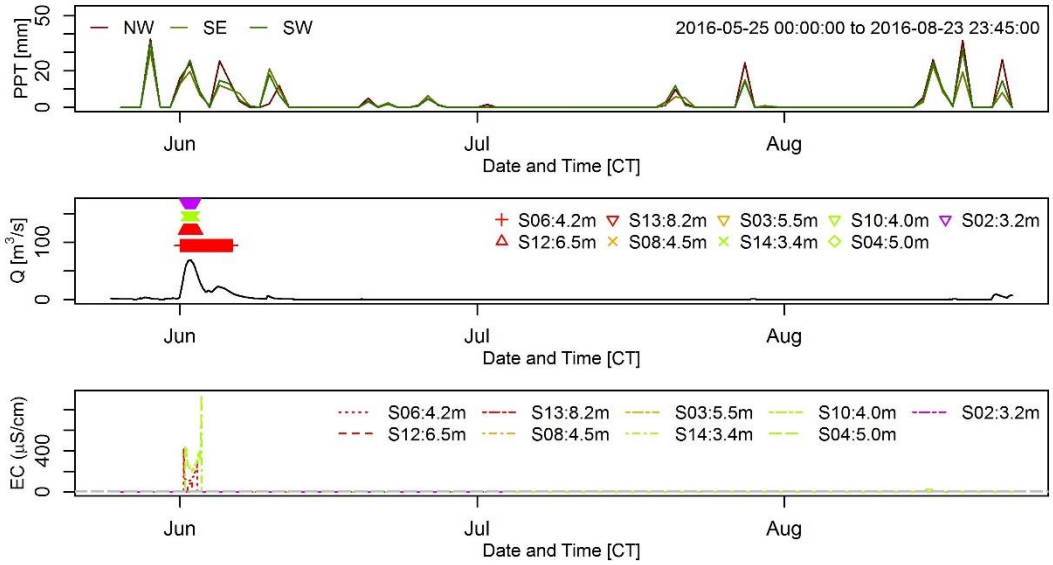

Figure IV-3. Time-series of precipitation (PPT), discharge (Q), and electrical conductivity (EC) for time-period 1 (TP1) that includes the dates 2016-05-25 to 2016-08-23. The colors of the lines and points being plotted coordinate with the colors being used in Figures IV-1 and IV-2 for the PPT stations and STICL locations. (Note: dashed grey lines define the bounds for the EC values expected for rainfall and riverine inundation; the ID for each STICL is followed by the elevation at which each STICL was installed using NAVD88; CT = Central Time).

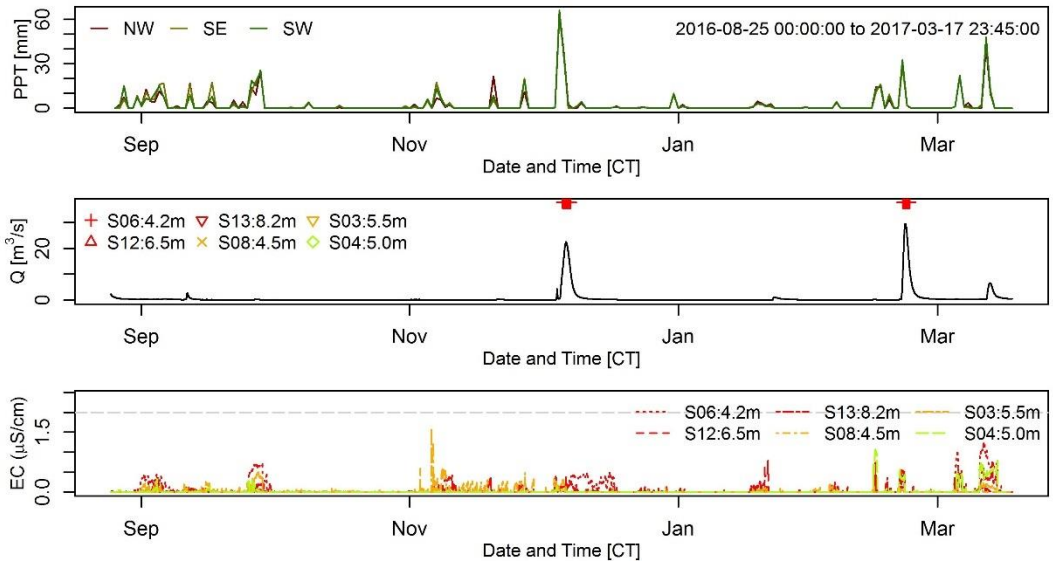

Figure IV-4. Time-series of precipitation (PPT), discharge (Q), and electrical conductivity (EC) for time-period 2 (TP2) that includes the dates 2016-08-25 to 2017-03-17. The colors of the lines and points being plotted coordinate with the colors being used in Figures IV-1 and IV-2 for the PPT stations and STICL locations. (Note: dashed grey lines define the bounds for the EC values expected for rainfall and riverine inundation; the ID for each STICL is followed by the elevation at which each STICL was installed using NAVD88; CT = Central Time).

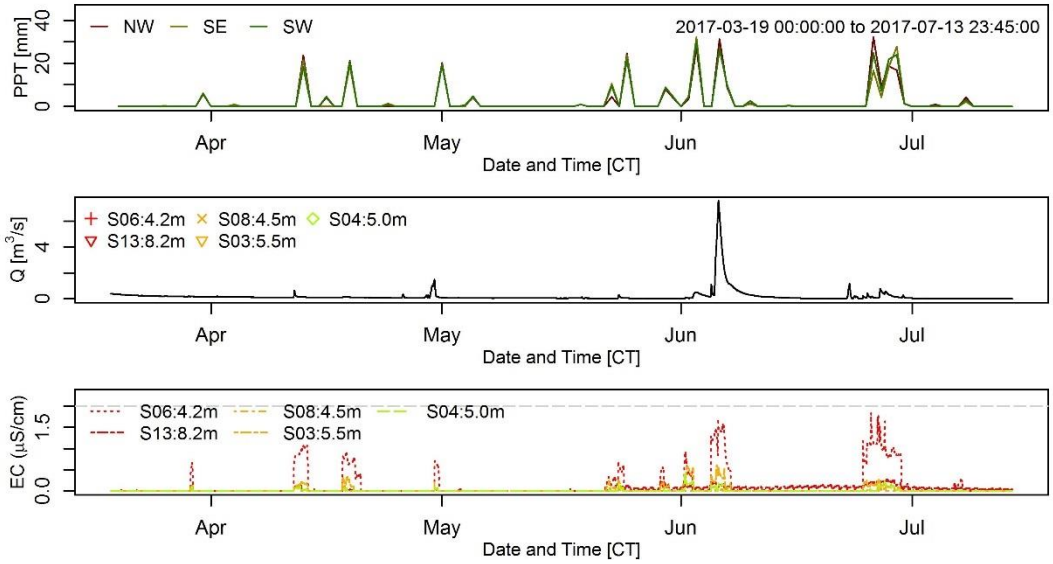

Figure IV-5. Time-series of precipitation (PPT), discharge (Q), and electrical conductivity (EC) for time-period 3 (TP3) that includes the dates 2017-03-19 to 2017-07-13. The colors of the lines and points being plotted coordinate with the colors being used in Figures IV-1 and IV-2 for the PPT stations and STICL locations. (Note: dashed grey lines define the bounds for the EC values expected for rainfall and riverine inundation; the ID for each STICL is followed by the elevation at which each STICL was installed using NAVD88; CT = Central Time).

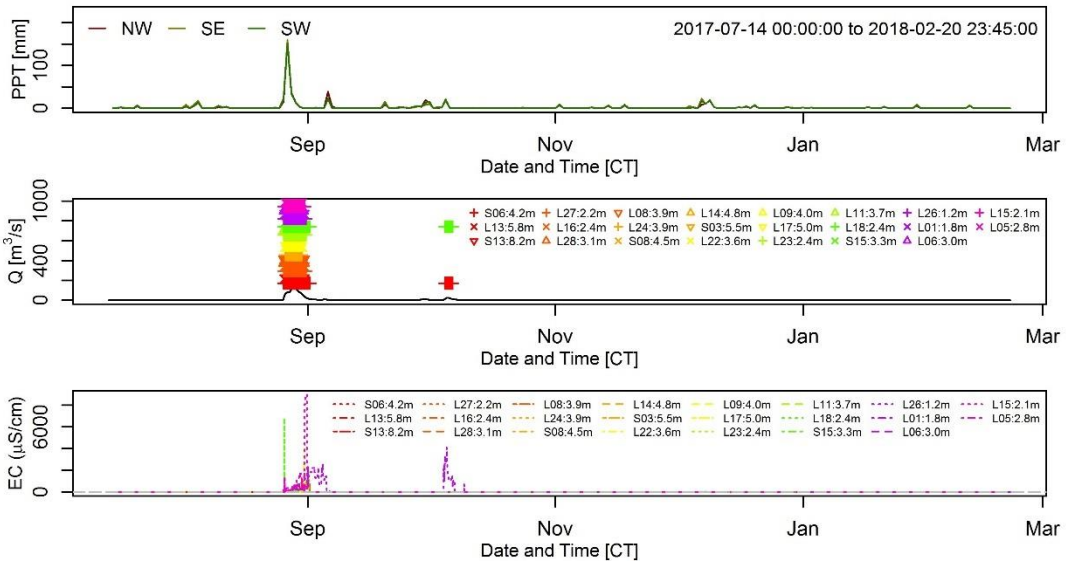

Figure IV-6. Time-series' of precipitation (PPT), discharge (Q), and electrical conductivity (EC) for time-period 4 (TP4) that includes the dates 2017-07-14 to 2018-02-20. The colors of the lines and points being plotted coordinate with the colors being used in Figures IV-1 and IV-2 for the PPT stations and STICL locations. (Note: dashed grey lines define the bounds for the EC values expected for rainfall and riverine inundation; the ID for each STICL is followed by the elevation at which each STICL was installed using NAVD88; times are in Central Time).

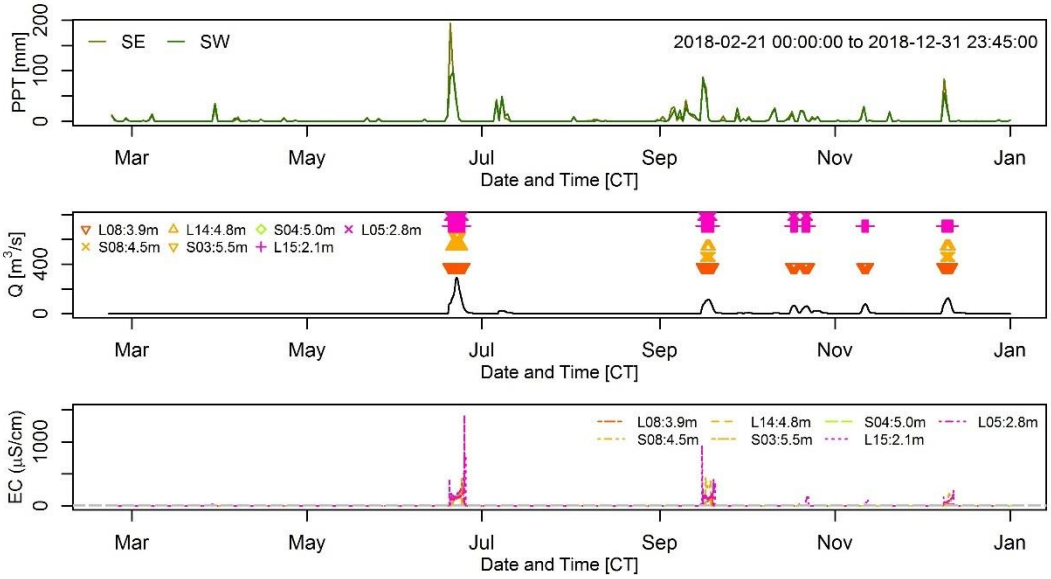

Figure IV-7. Time-series' of precipitation (PPT), discharge (Q), and electrical conductivity (EC) for time-period 5 (TP5) that includes the dates 2018-02-21 to 2018-12-30. The colors of the lines and points being plotted coordinate with the colors being used in Figures IV-1 and IV-2 for the PPT stations and STICL locations. (Note: dashed grey lines define the bounds for the EC values expected for rainfall and riverine inundation; the ID for each STICL is followed by the elevation at which each STICL was installed using NAVD88; times are in Central Time).

We represent the terrain with a gridded bare-earth digital terrain model (DTM) at 1-m spatial resolution that was developed using two lidar-based DTMs as part of the analysis used in (Castillo et al., In-Preperation). The locations where our data loggers were deployed fall within the portion of our DTM that was developed by the National Center for Airborne Laser Mapping (NCALM) using lidar point clouds collected in Mar-2018. The DTM was originally at a spatial resolution of 0.5-m, but we resampled it to a spatial resolution of 1-m using bilinear interpolation. The non-submerged portions of the terrain have a vertical error of 0.031 m. The submerged topography for portions of the main channel were synthetically generated using channel bed elevations from a detailed Flood Insurance Study (FIS) conducted by FEMA (FEMA, 2014) and methods from Legleiter and Kyriakidis (2008). The submerged portions of the terrain have an error of 0.76 m.

Outputs of flood inundation depth from steady two-dimensional hydrodynamic model simulations from Castillo et al. (In-Preperation) are used to estimate the streamflow conditions needed for inundation to occur at the location at which each STICL is installed. These simulated inundation depths are in gridded format with a spatial resolution of 1-m and each grid cell estimates the depth of flood inundation for the underlying area under the *Q* for Mission River being simulated. Our hydrodynamic model was assessed against FIS estimates of the longitudinal water-surface profile of four idealized flow conditions (streamflows with 10-year, 50-year, 100-year, and 500-year return periods) and we determined that our model deviates from these estimates by

0.2 m (Castillo et al., In-Preperation). A total of 23 simulations that span the historical streamflow record of the 08189500 USGS gaging station are considered here.

Field-based measurements of specific conductance (electrical conductivity at 25° C) for Mission River at the site of the 08189500 gaging station are used to determine the range of electrical conductivity values that a supposedly non-tidal portion of the river has experienced. These data (Reach ID: 2002; Station ID: 12944; Parameter Code: 00094) were collected by the Nueces River Authority (NRA) two or more times a year from 1972 through 2018 with 222 total measurements (Nueces River Authority, 2019). Specific conductance at this site has a range of 10 to 17500 µS/cm with a mean of 2157 µS/cm.

STICL Modifications

We use modified Onset HOBO Pendant waterproof temperature and light data loggers in our analysis that were modified using materials and methods described in Chapin et al. (2014) and Gillman et al. (2017); with the exception of the epoxy because we used Loctite ProLine Marine Adhesive Sealant. These methods involve removing the photodiode leads that estimates light intensity from the logger circuit chip and replacing them with a pair of electrodes that protrude externally from the water-proof housing caps (see Figure IV-1 of Gillman et al. (2017) for diagram of modifications). The modifications allow the *EC* of the medium that completes the circuit between the external electrodes to be estimated that are recorded as digital numbers at a 10-bit resolution and converted to light intensity units of lux (Lumens/m^2) or Lumens/ft^2 using algorithms in the HOBOware software (Version 3.7.17). Air is a very poor conductor of

electricity and the *EC* across the electrodes when exposed to only air should be zero. Water, on the other hand, can conduct electricity when it has some solutes and the *EC* increases with increasing solute concentrations. The modifications for estimating *EC* do not affect the temperature components of the STICL or how the recorded data is offloaded thus no additional modifications are needed to the STICL or the HOBOware software (Chapin et al., 2014, Gillman et al., 2017).

Our STICLs were acquired and modified in two phases. Our first set/phase of STICLs that were acquired and modified in early-Spring of 2016 included 14 STICLs, but only 10 remained operational through at least one TP and we only report the findings from these 10 STICLs. Our second set/phase of STICLs were acquired in early-summer of 2017 and it included 28 STICLs, but only 18 STICLs remained operable through at least one TP and we only report the findings from these 18 STICLs.

STICL Calibrations

We calibrate our STICL readings for *EC* in the lab using sets of calibration standards that allow the STICL readings to be used to estimate the *EC* of the inundating waters. We use a wide range of EC values in the calibration process because our study site can experience flood inundation from a variety of sources that include streamflows, intense rainfall-downpours, and surge from tropical storms/cyclones. Our first phase of STICLs was calibrated using standards with five *EC* values that include 0 (distilled water), 84, 1413, 2070, and 8974 μS/cm. Each STICL in the first phase of preparations was submerged in each standard for one hour on a one-second logging interval for a total of 3600 data points per calibration-trial (submersion of STICL in the calibration

standard). Our second phase of STICLs was calibrated using six *EC* standards with values that include 23, 84, 447, 1413, 2764, and 8974 µS/cm. Each STICL of the second phase of preparations was submerged in each standard for one hour on a three-second logging interval for a total of 1200 data points per calibration-trial.

The readings from each calibration-trial was offloaded from each STICL using the Optic USB base station and the HOBOware software. The STICL readings on the light intensity channel are then converted to the lux unit that has a range from 0 to 330,000. The sensitivity in the electrical conductance that each modified STICL can detect varies on a case-by-case basis, but we limited our calibrations to the range of 0-8974 µS/cm. Although, there is one STICL (S15) that was only calibrated using an *EC* range of 0-2764 µS/cm. The range of standards that was used for each STICL is shown in Tables C-1 and C-2 for the first and second phase of STICL preparations. Linear spline regressions were fitted to the set of calibration-trials for each STICL where the regressions took the generalized form of Eq. IV-1.

$$R_{ls}(x) = \begin{cases} p_0(x_0) = 0, & x = x_0 = 0, \\ p_1(x) = p_0(x_0) + \beta_1 x, & x \in [x_0, x_1), \\ p_2(x) = p_1(x_1) + \beta_2 x, & x \in [x_1, x_2), \\ \vdots & \\ p_n(x) = p_{n-1}(x_{n-1}) + \beta_n x, & x \in [x_{n-1}, x_n], \end{cases} \qquad \textit{(Eq. IV-1)}$$

where $R_{ls}(x)$ is the fitted linear spline regression for a set of calibration-trials, $p_n(x)$ is the fitted piece-wise linear function (linear spline with degree of 1) that corresponds to a given x-value ("light intensity" from a data logger in this case), x_n is the x-value that corresponds with the knots in the fitted linear spline, and β_n is the slope of the line that connects the knots of the linear spline. The regression is forced to start at the origin with

linear fits representing the regression between the knots of the spline. The mean "light intensity" values for each calibration-trial are used as the knots in the fitted linear spline models. There are some cases where STICLs and their associated linear spline regressions are able to achieve values >8974 μS/cm, but we limit all *EC* values to a range of 0-8974 μS/cm.

STICL Deployments

Our 28 STICLs were deployed at the eight locations shown in Figure 2, but their operational deployments only coincided with the descriptions shown in Table IV-1. STICLs were deployed on days where streamflows were at baseflow values and placed within un-submerged portions of the banks of the active channel or on the adjacent floodplain. Moreover, STICLs were also positioned in a manner where each STICL within a location had a distinct elevation that allowed them to capture the vertical and lateral surface-water connectivity for a variety of streamflows. The spatial positioning of our STICLs is determined using a Trimble R8-2 Global Navigation Satellite System (GNSS) unit with a range in the horizontal spatial error of 0.73 to 2.22 m for all STICL positions. We use our DTM to determine the elevation (in NAVD88) at which each STICL is deployed.

Records from our deployed STICLs are offloaded using the HOBO base-station and the Hoboware software. We then use the fitted linear spline model for each data logger from the calibration to estimate the *EC* experienced by the STICLs in the field during the five TPs considered here. STICL inundation can occur from a variety of individual or combined sources that include intense rainfall, riverine flooding, and

marine processes (tides and storm-surge). *EC* readings from our STICLs need a value of ≥2 μS/cm to be considered inundated from rainfall (melted snow typically ranges from 2 to 42 μS/cm (CSWRCB, 2004) and we assume that rainfall has similar *EC* values). We use the specific conductance range (10-17500 μS/cm) from the NRA field-measurements to define the bounds for the *EC* values that will be considered riverine as the source of inundation. Our STICLs are limited to a value of 8974 μS/cm that falls within the riverine range; thus we generally do not classify any of our loggers readings as inundated by marine water, but there is an event in TP4 where we feel it is more appropriate to label some of the *EC* readings as inundation caused by marine processes (See *Time-Series Comparisons* in **Results** section).

Estimates of Streamflow Needed for STICL Inundation

We use the spatial (horizontal and vertical) positioning of each STICL to estimate the values of *Q* for Mission River that would result in a STICL being inundated by streamflows. A Geographic Information Systems (GIS) overlay operation with the STICL positions and the 23 gridded inundation depth estimates are used to identify the minimum simulated *Q* that would result in a data logger being inundated. There is uncertainty in the spatial positioning of each STICL and the water-surface elevation of our model estimates. We incorporate these uncertainties into our estimates of the minimum *Q* (Q_{min}) needed for a STICL needed to be considered inundated in four (4) steps. First (1), the horizontal spatial error of each STICL position is accounted for by generating circular buffers around each STICL position with a radius that is equal to the horizontal error recorded at each STICL position by the GNSS. We use these buffers in

the overlay GIS operation with the set of simulated inundation depths to identify the minimum of the simulated *Q*s that intersect a given buffer. Second (2), the vertical spatial error in the DTM (error is 0.031 m in un-submerged portions of the terrain) is identified and recorded. Third (3), the vertical uncertainty in our hydrodynamic model is identified (error in water-surface elevation is 0.20 m) and accounted for by adding it to the DTM error identified in (2). Fourth (4), the most recent rating curve for the 08189500 USGS gaging station is used to determine a range of streamflows that could result in a given STICL becoming inundated by using the relationship that *h* has with *Q* in the rating curve. The corresponding *Q* identified in (1) has an associated *h* within the rating curve. We add and subtract the total vertical error calculated in (3) to calculate a range of possible *h* values and extract the *Q* values associated with this range. Here we assume that the Q_{min} identified in (4) for each data logger position is the streamflow needed for the respective STICL to be inundated (Figure IV-8).

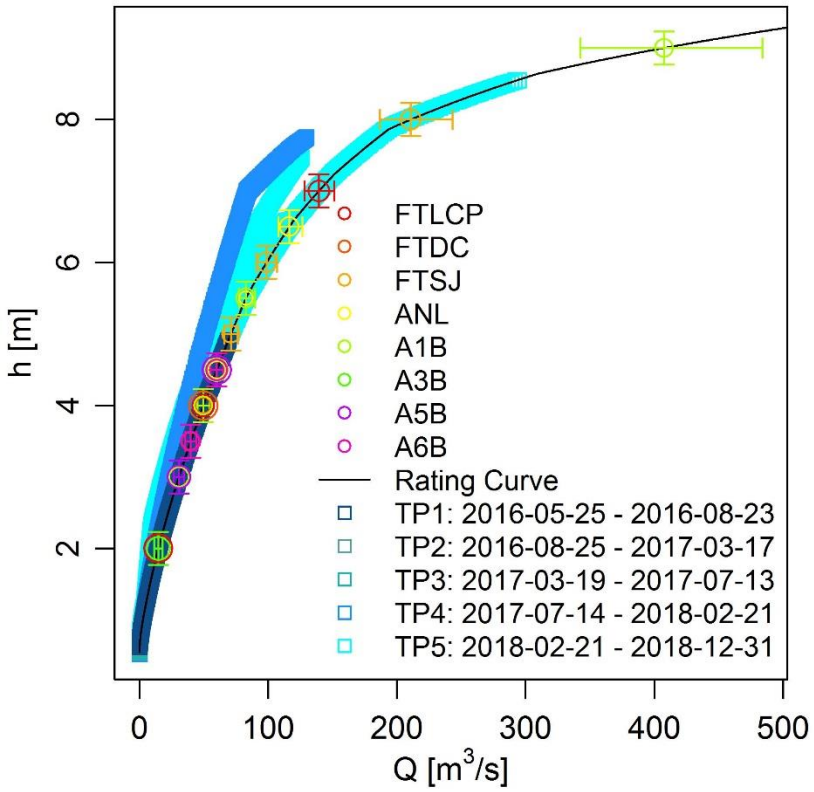

Figure IV-8. Estimates of the discharge (Q) and stage (h) needed for our STICLs to be inundated. STICLs are labeled in accordance with their respective deployment location described in Table 1 and Figure 2. The size of the circle that represents each STICL is proportional to the horizontal spatial uncertainty of a STICL position with larger circles indicating more horizontal uncertainty. Error bars are used to illustrate the range of streamflows that are estimated to cause a STICL to be inundated. The minimum Q (Qmin) identified for each STICL (left-edge of error bars) is used here to identify the streamflow records in the period of interest that potentially cause the STICLs to be inundated. The rating curve for the 08189500 USGS gaging station and the instantaneous streamflows (15-minute sampling interval) for the five time-periods considered (See Table 1) here are also shown.

Time-Series Comparisons

The three types of data that we consider here (*PPT*, *Q*, and *EC*) are recorded in time-series format. We plot the time-series of these variables for each of our time-periods of interest and compare the trends. In particular, we examine the oscillations in *EC* to determine if the peaks and plateaus in the signal coincide with *PPT* and increased-

Q events. We also analyze if our estimates of the streamflows that result in the STICLs being inundated coincide with the STICL records. Moreover, a variety of flood-water sources can inundate our STICLs (e.g., riverine, meteorological, marine, and groundwater) and we use the *EC* values to decipher the flood-water sources for the signals recorded in our STICLs.

Results

STICL Calibrations

Linear spline regressions were fit to the data from the laboratory calibrations for *EC*. The first phase of the STICL preparations included 10 STICLs that were subjected to five calibration trials (0, 84, 1413, 2070, and 8974 μS/cm; Table C-1). All fitted linear spline models and their coefficients (slopes in the linear splines) from the first phase of STICL preparations are statistically significant at the $\alpha = 0.05$ level. The standard error for the fitted models (SE_{mod}) ranges from 16 to 422 μS/cm with a mean SE_{mod} of 200 μS/cm. The fit for S10 is worst for the data loggers in the first phase of data logger preparations but all fits are considered suitable with a SE_{mod} that is ≤5% of the calibration range.

The second phase of the STICL preparations included 18 STICLs that were subjected to six calibration-trials (23, 84, 447, 1413, 2764, and 8974 μS/cm; Table C-2). All fitted linear spline models and their coefficients from the second phase of STICL preparations are statistically significant at the $\alpha = 0.05$ level. The standard error for the fitted models (SE_{mod}) ranged from 7 to 1162 μS/cm with a mean SE_{mod} of 421 μS/cm. The fit for L15 is the worst for the STICL in the second phase of STICL preparations

and it skews the distribution of SE_{mod} for this phase, but the fits for the remaining models are considered reasonable. Eight of the 19 fitted models for the second phase of STICL preparations have SE_{mod} values ≥5% of the calibration range, but nonetheless, all models are considered reasonable for our purposes.

STICL Deployments

TP1 is the TP from 2016-05-25 to 2016-08-23 that spans 91 days and the STICLs that were deployed and operational throughout TP1 were able to record 8,736 data points (Table C-1). Nine STICLs deployed at four locations were recording data on a 15-minute interval. With the exception of S10 and S02 that have temporal coverages of 91 and 45%, respectively; all other STICLs in Figure 3 have 100% temporal coverage during TP1. In terms of logged readings, all STICLs readings remain at zero until early June when two STICLs at FTLCP (S12 and S06) and S14 at A1B increase to an *EC* >84 μS/cm (S06 and S14 reach *EC* values of 422 and 949 μS/cm, respectively) then decline after a few days. S14 and S06 in particular have two peaks in their response at either end of this event. Amongst the three STICLs that responded during this early-June event, the STICLs placed at a lower elevation retained these increased values longer indicating that the STICLs at lower elevations were inundated for a longer duration of time. Moreover, there is a small lag in terms of the signal response at the downstream A1B location compared to the upstream FTLCP location. There are only very minor events throughout the remaining TP1. Moreover, the readings from S02 at A5B stop in early-July. In terms of the source of the inundation that is the causing the larger STICL responses, four of the STICLs (S06, S12, S14, and S10) exhibited *EC* values that can be classified as being

inundated by riverine water. The duration of inundation for these STICLs has a range from 0.5 to 1.8% of TP1 (Table IV-4). For STICLs deployed within the same location, the STICLs with a lower elevation are inundated for a higher duration.

TP2 is the TP from 2016-08-25 to 2017-03-17 that spans 205 days and the STICLs that were deployed and operational throughout TP2 were able to record 19,688 data points (Table IV-1). Six STICLs deployed at three locations were recording data on a 15-minute interval. All STICLs deployed during TP2 have 100% temporal coverage (Figure IV-4). In terms of logged readings, all STICLs exhibit *EC* values <2 μS/cm with all six STICLs responding collectively to five groups of events. S08 and S06 tend to have the largest responses for their respective locations for each of these events, but there is no obvious trend for the STICL responses amongst the event groups. None of the STICLs that exhibited responses to the *PPT* and *Q* events had *EC* values high enough to be classified as being inundated by any of the water sources considered here and thus the duration of inundated was not determined (Table IV-4).

TP3 is the TP from 2017-03-19 to 2017-07-13 that spans 117 days and the STICLs that were deployed and operational through TP3 were able to record 11,232 data points (Table IV-1). Five STICLs deployed at three locations were recording data on a 15-minute interval. All five STICLs deployed during TP3 had 100% temporal coverage (Figure IV-5). In terms of logged readings, there are nine groups of events with the most obvious events occurring from late-May through mid-July. S06 at the FTLCP location had the responses with the greatest magnitude for each of the nine events with a maximum *EC* value of 1.8 μS/cm. The other STICLs also respond during the nine

events, but not to same degree as S06. None of the STICLs that exhibited responses to the *PPT* and *Q* events had *EC* values high enough to be classified as being inundated by any of the water sources considered here and thus the duration of inundated was not determined (Table IV-4).

TP4 is the TP from 2017-07-14 to 2018-02-20 that spans 222 days and the STICLs that were deployed and operational through TP4 were able to record 21,324 data points (Table IV-1). Twenty-three STICLs deployed at eight locations were recording data on a 15-minute interval. All 23 STICLs deployed during TP4 had 100% temporal coverage (Figure IV-6). In terms of logged readings, with the exception of S03 that had a negligible response, all other STICLs recorded a large event at the end of August around the time Hurricane Harvey progressed through the study area. The max readings for all STICLs that responded to Hurricane Harvey reached *EC* values ≥157 μS/cm, but 17 of the STICLs logged *EC* values >500 μS/cm. Moreover, eight of the STICLs had readings >1500 μS/cm that exceeds the typical *EC* values found within freshwater systems. With the exception of L26 at A5B that exhibits another event after Hurricane Harvey with several *EC* values >100 μS/cm, no other STICLs exhibit obvious event responses through the rest of TP4. In terms of the source of the inundation that is the causing the larger STICL responses, 22 of the STICLs exhibited *EC* values that can be classified as being inundated by riverine water. The duration of inundation for these STICLs has a range from 0.2 to 7.8% of TP4 (Table IV-4). STICLs with a relatively low elevation compared to other STICLs deployed at the same location tend to be inundated for a

longer duration, but this is not always the case and STICLs at FTDC are a prime example.

TP5 is the TP from 2018-02-21 to 2019-12-31 that spans 314 days and the STICLs that were deployed and operational through TP5 were able to record 30,048 data points (Table IV-1). Seven STICLs deployed at four locations were recording data on a 15-minute interval. With the exception of L05 that has a temporal coverage of 79%, all other STICL have a temporal coverage of ≥94% for TP5 (Figure IV-7). In terms of logged readings, two prominent events are exhibited in June and September where L08 at FTDC, L14 at FTSJ, and both STICLs at A6B (L05 and L15) all logged *EC* values >300 μS/cm. Similar to what was exhibited in TP1, peaks in STICL readings occur at either side of the two prominent events. There are three other minor events in the Fall months (one per month in October, November, and December) where the four aforementioned STICLs also logged readings with *EC* > 100 μS/cm. In terms of the source of the inundation that is causing the larger STICL responses, five of the STICLs (L08, S08, L14, L15, and L05) exhibited *EC* values that can be classified as being inundated by riverine water. The duration of inundation for these STICLs has a range from 1.0 to 5.5% of TP5 (Table IV-4). STICLs with a lower elevation than other STICLs deployed at the same location tend to be inundated for a longer duration, but this is not always the case as S08 and L14 have the same duration of inundation.

Estimates of Streamflow Needed for STICL Inundation

We estimated the minimum *Q* (Q_{min}) needed for each STICL to be inundated by streamflows and used these estimates to predict how often a STICL should be inundated

for a given TP (Table IV-4). The STICLs of FTLCP are in close proximity to each other and the range of elevations at which they were deployed ranges from 4.2 to 8.2 m. The STICLs at FTLCP lie within the Mission River main channel and there is a percent difference of 1023% for the Q_{min} between the STICLs at the lowest and highest elevations (S06 and S13, respectively). There is no TP where all four of the STICLs deployed at FTLCP are collectively operational, but there are combinations of three STICLs operating for the first four TPs (TP1-TP4). STICLs at lower elevations are always predicted to be inundated for a longer duration in each TP. The four STICLs at FTLCP are estimated to be inundated an average of 2.78 (S06), 2.28 (L13), 0.48 (S12), and 0.03 (S13) percent of the time during the first four TPs with a percent difference in the average duration of inundation of 9176% between STICLs S06 and S13.

FTDC STICLs are deployed in two locations along Dry Creek with differing channel and floodplain dimensions in areas that are influenced by backwater flooding from Mission River. STICLs at both locations are deployed with one being deployed within the channel while the other is deployed on the adjacent floodplain. The ranges in the deployment elevations for the STICLs at both FTDC locations is 2.4 to 3.1 m and 2.2 to 3.9 m (Table IV-4), respectively, while the percent difference in Q_{min} between STICLs at both locations are 29% and 67%. All STICLs at FTDC were only collectively operational during TP4 (L08 was also operational during TP5). Between the in-channel STICLs (L27 and L16), L27 is predicted to be inundated for 6.6% more of TP4 because it has a lower elevation and it is closer to the Dry Creek-Mission River confluence. This differs for L28 and L08 that are deployed on the floodplain at different elevations and

longitudinal positions, but both are predicted to be inundated for the same amount of time for TP4. This prediction is likely due to L08 lying more downstream (Figure IV-2) where it more readily experiences backwater flooding from Mission River.

FTSJ STICLs are deployed in two locations with one location being within the main channel of Mission River in a gas pipeline clearing and the other being on a forested portion of the floodplain adjacent to the pipeline clearing. The ranges in deployment elevations for the STICLs at both FTSJ locations is 3.9 (L24) to 4.5 m (S08) and 4.8 (L14) to 5.5 m (S03), respectively (Table IV-4), while the percent difference in Q_{min} between the STICLs at both locations is 38 and 72%. The elevation difference between both FTSJ locations is almost equal, but the Q_{min} difference for the floodplain STICLs is almost twice that of the in-channel STICLs because flood waters spread over a much larger area when they are in the floodplain and this requires a larger Q in order to increase the water-surface elevation an equal amount. All STICLs at FTSJ are only collectively operational during TP4 where STICLs deployed at lower elevations are always predicted to be inundated for a longer duration (S03 was predicted to not experience inundation). For TP4, L24 is predicted to be inundated 103% more often than S08 that is in-channel and 209% more often than L14 that lies on the forested floodplain.

Table IV-4. The elevation (in NAVD88) and the estimate of the minimum discharge (Q_{min}) that results in each STICL being inundated by streamflows. The percentage of each time-period (TP) that each STICL is predicted to be inundated (left of the "/") and the percentage of the time that it is predicted to be inundated in accordance to the estimated electrical conductivity (*EC*) values (right of the "/") are also shown. The number of *Q* data points sampled on a 15-minute interval are below each TP label (Note: STICL = Stream Temperature, Intermittence, and Conductivity logger; na = the STICL was not deployed or operational during this TP; see Study Area and Figure IV-2 for descriptions of where STICLs were deployed; see Table IV-1 for descriptions of each TP).

Location	STICL	Elevation [m]	Q_{min} [m^3/s]	Estimated Percentage of TP Inundated [%]				
				TP1 (8,736)	TP2 (19,688)	TP3 (11,232)	TP4 (21,324)	TP5 (30,048)
FTLCP	S06	4.2	11.4	5.7/1.5	1.7/0.0	0.0/0.0	3.8/3.7	na
	L13	5.8	35.4	na	na	na	2.3/1.5	na
	S12	6.5	44.9	1.4/0.5	0.0/0.0	0.0/0.0	na	na
	S13	8.2	128.1	0.0/0.0	0.0/0.0	0.0/0.0	0.1/0.2	na
FTDC	L27	2.2	26.6	na	na	na	2.4/2.8	na
	L16	2.4	35.4	na	na	na	2.3/2.9	na
	L28	3.1	44.9	na	na	na	2.1/1.7	na
	L08	3.9	44.9	na	na	na	2.1/2.0	5.8/3.4
FTSJ	L24	3.9	65.9	na	na	na	1.8/2.2	na
	S08	4.5	91.0	0.0/0.0	0.0/0.0	0.0/0.0	0.9/1.7	2.6/1.0
	L14	4.8	108.1	na	na	na	0.6/1.3	1.9/1.0
	S03	5.5	186.9	0.0/0.0	0.0/0.0	0.0/0.0	0.0/0.0	0.6/0.0
ANL	L22	3.6	55.1	na	na	na	2.0/2.0	na
	L09	4.0	77.2	na	na	na	1.4/1.3	na
	L17	5.0	108.1	na	na	na	0.6/0.8	na
A1B	L23	2.4	26.6	na	na	na	2.4/2.4	na
	S14	3.4	55.1	1.1/1.8	na	na	na	na
	L11	3.7	44.9	na	na	na	2.1/1.3	na
	S10	4.0	77.2	0.0/0.8	0.0/0.0	na	na	na
	S04	5.0	342.5	0.0/0.0	0.0/0.0	0.0/0.0	na	0.0/0.0
A3B	L18	2.4	11.4	na	na	na	3.8/2.1	na
	S15	3.3	55.1	na	na	na	2.0/1.9	na
A5B	L26	1.2	26.6	na	na	na	2.4/7.8	na
	L01	1.8	35.4	na	na	na	2.3/2.5	na
	L06	3.0	55.1	na	na	na	2.0/1.6	na
	S02	3.2	55.1	1.1/0.0	na	na	na	na
A6B	L15	2.1	35.4	na	na	na	2.3/2.5	6.4/5.5
	L05	2.8	55.1	na	na	na	2.0/2.4	5.1/4.1

ANL STICLs are deployed in two locations along the channel-face of a natural levee with one lying on a shallower part of the natural levee while the other two are on a steeper part. The ranges in deployment elevations for data loggers at ANL are 3.6 to 5.0 m (Table IV-4), while the percent difference in Q_{min} between L17 and the other two STICLs (L09 and L22) is 40 and 96%, respectively. This difference in Q_{min} is partially due to the elevation differences, but is also due to L22 being in a less steep portion of the natural levee that allows the main channel of Mission River to be wider. All STICLs at ANL were only operational during TP4 where the percent difference in the duration of inundation between the L17 and the other STICLs (L09 and L22) is 43 and 240%, respectively. Again, the STICLs at a lower elevation are predicted to be inundated for a much longer duration due to the differences in Q_{min}.

A1B STICLs are deployed at two locations along the cut bank of the first meander bend in the downstream portions of the study reach. Both STICLs at the upstream A1B location (L23 and S14) are placed within the main channel with the lowest elevations for A1B of 2.4 and 3.4 m, respectively (Table IV-4). The predicted Q_{min} for S14 is 107% greater than the Q_{min} for L23. Two of the three STICLs at the downstream A1B location lie within the main channel with elevations of 3.7 (L11) and 4.0 m (S10); and the third (S04) is deployed on the adjacent floodplain with an elevation of 5.0 m. Despite the modest elevation difference between the in-channel STICLs at the downstream A1B location, the Q_{min} for S10 is 72% greater than for L11 and this is because both data loggers are placed near the top of the channel banks. S04 is deployed on the floodplain with an elevation that is 1 m higher than S10, but S04 has a Q_{min} that is

344% greater than the Q_{min} for S10. The five STICLs are operational sporadically throughout the five TPs, but the data loggers deployed at a lower elevation are predicted to be inundated for a longer duration than those at a lower elevation. For example, L23 and L11 are both operational during TP4 and L23 is predicted to be inundated for 14% more of the time than L11 that is at a higher elevation.

A3B STICLs are deployed on the cut bank near the apex of the third meander bend of the Mission River main channel in downstream portions of the study reach. Both A3B STICLs are deployed within the main channel at elevations of 2.4 (L18) and 3.3 m (S15; Table IV-4). Despite an elevation difference of >1 m, the Q_{min} for S15 is 383% greater than that for L18. Both STICLs are only operational during TP4 where L18 is predicted to be inundated for a duration that is 91% greater than the duration predicted for S15.

A5B STICLs are deployed just upstream of the cut bank on the fifth bend of the main channel for Mission River. The four STICLs are deployed on a low-spot that slopes upwards as the lateral distance from the channel increases. Elevations of the four A5B STICLs are 1.2 (L26), 1.8 (L01), 3.0 (L06), and 3.2 m (S02) with a Q_{min} that increases with elevation with the exception of L06 and S02 that have an equal Q_{min} (Table IV-4). The percent difference in Q_{min} between the lowest and highest STICLs is 106%. STICLs at A5B are only operational during TP1 and TP4 with TP4 being the TP with the most operational STICLs. The duration of inundation for L26 is 23% greater than that of L06 during TP4 and this difference is mostly due to the elevation differences.

A6B STICLs are deployed on the floodplain of the downstream end of the sixth meander bend in the most downstream portion of our study reach. The two STICLs are deployed on a relatively flat floodplain with L15 being close to the channel edge and at a lower elevation. L15 is at an elevation of 2.1m and L05 is at 2.8 m with L05 having a Q_{min} that is 56% greater than that of L15. Both STICLs are operational during TP4 and TP5 with a predicted average inundation duration of 4.35 and 2.78% for both TPs. The average duration for L15 is 56% greater and this is mostly due to the proximity to the main channel and the elevation differences.

Time-Series Comparisons

We compare our three types of time-series (*PPT*, *Q*, and *EC*) in order to determine if the trend of *EC* values that we observe for each TP coincide with the respective trends in *PPT* and *Q*. For TP1, there is one prominent event for *EC* in early-June (Figure IV-3). S06, S12, and S14 all have a large multimodal rise in their *EC* values that rise to values that fall within the range of 50-2000 μS/cm that is typical for rivers in the United States (U.S. Environmental Protection Agency, 2012, CSWRCB, 2004). These increases in *EC* coincide with a multimodal rise in *Q* and several peaks in *PPT*. Four STICLs (S06, S12, S14, and S02) are predicted to be inundated at about the same time as when the events in *EC* occur, but the *EC* of S02 does not respond as predicted and the duration of inundation is generally overpredicted for the other three STICLs. The rough agreement with the predictions of riverine inundation duration, the relatively high *EC* values reported by the STICLs that had events of increased *EC*, and the roughly

equal magnitude between all *PPT* peaks in TP1 (ones that coincide with *EC* events and those that don't) all suggest that the *EC* events were spurred by riverine inundation.

The time-series from our six operational STICLs in TP2 (S06, S12, S13, S08, S03, and S04) are all noisy with some clusters of relatively higher *EC* values that coincide with some of the *PPT* peaks (Figure IV-4). S06 is predicted to experience some brief riverine inundation during two peaks in *Q* that occurred in December and February, but S06 only exhibits low *EC* values with no trend that resembles these peaks in *Q*. The disagreement with the predictions of riverine inundation duration, the low *EC* values reported by all the data loggers, and the noisy trends in the *EC* trends that tend to have their highest values for TP2 when there are *PPT* events all suggest that the *EC* patterns exhibited were spurred by wetting from rainfall.

For TP3, the time-series of *EC* from our five operational STICLs (S06, S13, S08, S03, and S04) is somewhat noisy, but there are some prominent events with increases in *EC* that coincide with *PPT* events littered throughout TP3 (Figure IV-5). *Q* is very low throughout TP3 and none of the STICLs are predicted to experience inundation, but some of the STICLs (S06, S03, and S04) do exhibit relative increases in *EC* values where *Q* peaks that also coincide with *PPT* events. The *EC* values are too low to be resemble what would be expected from streamflows and the duration of the events exhibited by all STICLs align well with the duration of the *PPT* events. The lack of predictions from riverine inundation, the low EC values reported by all the STICLs, and the trends in the *EC* values that tend to have their highest values for TP3 when there are

PPT events all suggest that the *EC* patterns exhibited were spurred by wetting from rainfall events.

With the exception of the time-series for S03, the time-series of *EC* from our 22 other STICLs that were operational during TP4 exhibit large increases in late-August to early-September that coincide with Hurricane Harvey progressing over the study reach (Figure IV-6). In particular, there are two distinct peaks in the *EC* time-series with some STICLs having a large peak when the hurricane was over the study reach and the other shortly after the hurricane moved on. L26 also had another considerable event in early-October. *Q* has one prominent event that peaks shortly after Hurricane Harvey progressed through the area and another minor event in late-September – early-October. In terms of our predictions for when a STICL would be inundated from streamflows, 21 are predicted to experience inundation during the rise in *Q* from Hurricane Harvey and two STICLs are predicted to be inundated for the minor event in early-October. Data loggers with relatively lower elevations are predicted to experience inundation for longer durations in general. *PPT* has one prominent event that occurs during Hurricane Harvey and several much smaller events that occur throughout the TP. We attribute the first large peak in *EC* from some of our low-lying STICLs to coastal storm surge that traveled up the Mission River main channel because the *EC* values are too high to be from rainfall and *Q* is not high enough for these STICLs to be inundated from streamflow. The second set of high *EC* events occurs during the peak in *Q* that occurred during and shortly after Hurricane Harvey progressed through the study area. With the exception of some anomalously high *EC* values exhibited by L15 and L26, all other elevated *EC*

values are within the range that can be expected of streamflows during a storm event and we attribute these responses to the elevated streamflows. S06 and L18 are predicted to be inundated during the minor event for *Q* in early-October, but there is no response from these STICLs during this event. However, L26 is not predicted to respond during this event, but it has an anomalously high response for such a small *Q* event. Nonetheless, the duration of the *EC* event for L26 aligns well with the *Q* event and we attribute the L26 response to streamflows.

Five of the seven STICLs (L08, S08, L14, L15, and L05) that were operational during TP5 exhibit two large responses and one smaller response in their *EC* values from our set of data loggers in late-June, mid-September, and early-December (Figure IV-7). L15 also exhibits two smaller responses in late-October and early-November. *Q* has one very large event in late-June and five other large events in late-September through early-December. In terms of our predictions for when data loggers will be inundated, five STICLs (L08, L14, S03, L15, and L05) are predicted to be inundated and all except for S03 exhibit *EC* values indicative of riverine inundation. Five STICLs are predicted to be inundated for the late-September *Q* event, but only four (L08, S08, L15, and L05) exhibit *EC* values indicative of inundation. Three STICLs are predicted to experience inundation for the two events in mid-October, but L15 is the only STICL with a minor response in its *EC* values. Two STICLs are predicted to experience inundation during the early-November event, but again L15 is the only one to exhibit a small response. Four STICLs are predicted to experience inundation for the early-December event, but only three (L08, S08, and L15) exhibit *EC* values indicative of inundation. In terms of

PPT, TP5 exhibited numerous considerable events in the summer and fall months. An increase in *Q* tends to correspond with the larger *PPT* events, but all seven STICLs exhibit modest responses from *PPT* events even when they are not inundated from streamflow events. We attribute the relatively large increases in the *EC* values that we see in Figure 7 to inundation from streamflows with the larger values corresponding to larger *Q* events that can transport more sediment and dissolved solids that increase the *EC* of the inundating waters.

Discussion

We modified and calibrated sets of data loggers that can record temperature and *EC* in the field (i.e., STICLs) using similar methods to those employed by Chapin et al. (2014) and Gillman et al. (2017). Although, our methods differ in two ways with the first being the range in *EC* values that we use in the calibration of our STICLs have a maximum *EC* of 8974 μS/cm while the maximum reported in the literature is 2746 μS/cm that was used by Chapin et al. (2014) and Jensen et al. (2019). We use a maximum *EC* calibration value that is 227% greater because the reach of Mission River where we deployed our STICLs can be impacted by tidal processes and storm surge that have electrical conductivity values that can be well above the range of 50-2000 μS/cm that is typical for freshwater streams in the U.S. (CSWRCB, 2004, U.S. Environmental Protection Agency, 2012). Second, we fit linear splines to the calibration data instead of polynomial curves that were employed by Chapin et al. (2014) and Gillman et al. (2017). This is because the linear splines allow us to customize the function for each calibration trial (spline knot) if needed and avoid overfitting problems that can occur when using

polynomials. That being said, the standard error in our fits ranges from 7 to 1162 μS/cm with most of the error typically being in the region that includes the two highest knots of the spline (the STICL "light intensity" values for *EC* values of 2746 and 8974 μS/cm; see Supplementary Tables 1 and 2). While the uncertainty in the *EC* readings for some of our STICLs is greater than what is typically reported in the literature, there is far less uncertainty at the lower range of the *EC* predictions and this allows us to more reliably decipher between rainfall and streamflow as the source of inundation for lower, but non-zero, data logger readings of *EC*. Hence, we use our fitted linear splines for each STICL to estimate the occurrence, duration, and source of inundation that a data logger experienced during each TP for the location at which they are deployed in the field.

With regard to the inundation experienced by our STICLs, we consider three potential sources of flood inundation and they include precipitation, riverine, and marine; but we are particularly interested in the inundation and associated surface-water connectivity produced by riverine sources. We use the STICL positions in the field and steady hydrodynamic simulations to estimate the Q_{min} that would result in a data logger becoming inundated. Q_{min} ranges from 11 to 343 m^3/s for all STICLs and these values were used to estimate the duration of inundation for the set of river flows that occurred during each TP. These durations are readily comparable with those generated using the field-based records from our STICLs and we compare both sets of durations (Table 4). For TP1, the Q_{min} estimates an average of 230% greater than the STICL-based estimates of inundation duration for the fluviatile terrace portion of the reach, while the Q_{min} estimates are an average of 69% less than those from the STICL-based estimates for the

alluvium portions of the reach. Only one STICL (S06) has a Q_{min} estimate of inundation duration of 1.7% of TP2, but there is no STICL-based inundation estimate for S06 (or any of the other active STICLs in TP2). No Q_{min} or STICL-based estimates of inundation are predicted for any of the active STICLs during TP3. For TP4, predictions of STICL inundation using the Q_{min} method were determined with ten STICLs within the fluviatile terrace locations and they have an average duration that is 12% lower than the average inundation durations from the STICL-based estimates. The inundation durations from the Q_{min} estimates for ten STICLs in the alluvium locations are predicted to occur an average of 5% greater than those determined using the *EC* values from these STICLs. Three active STICLs in the fluviatile terrace locations have Q_{min} inundation duration estimates that are an average of 107% greater than the respective STICL-based estimates for TP5. On the other hand, Q_{min} estimates of STICL inundation duration are an average of 20% greater than the STICL-based estimates for the two STICLs that had predictions within the alluvium locations.

The differences between our Q_{min} and STICL-based estimates of the duration of riverine inundation can vary somewhat dramatically and there are two reasons that we attribute for these differences. First, the *EC* values that we use to determine if a STICL was inundated were estimated using the raw "light intensity" values alone. The electrical conductivity of water will vary by ~2%/°C with higher temperatures having a higher electrical conductance (Chapin et al., 2014, Gillman et al., 2017). We strictly apply a rule-based classification where *EC* values need to fall within the specific conductance range of 10-17500 µS/cm that is reported by NRA records in order for them to be

considered as riverine inundation. Our approach could be improved by using both the "light intensity" and temperature data from the STICLs to convert our calibration and field-based *EC* data to specific conductance. This will allow for a more direct comparison between our STICL records and those from the NRA and it is something that we will consider in the future. Second, the Q_{min} estimates were established using the STICL positions and steady hydrodynamic simulations. There is some uncertainty in the spatial position of the STICLs and while we use some aspects of the uncertainty to determine candidate values that should be associated with Q_{min}, there is more that we can do to stochastically determine the most appropriate STICL positions. This will allow our comparisons with the hydrodynamic simulations to be more informed by the STICL positions so that the most appropriate Q_{min} value for each respective STICL is determined. Although, our simulations assume steady flow conditions, but the flow records that we apply them towards are hydrologic events that rarely have the same inundation amount of inundation as a steady simulation. This is an issue that is difficult to address in our analysis, but it is another layer of uncertainty that we will try to account for in the future.

The literature has shown that data loggers that are installed on a channel bed and record ambient temperature and/or electrical conductivity can be valuable tools in analyses of ephemeral streams that focus on surface-water connectivity along the longitudinal dimensions of a channel reach (e.g., Bhamjee and Lindsay (2011)) or drainage network (e.g., Arismendi et al. (2017)). While we are also interested in surface-water connectivity, our analysis differs in that we analyze a perennial lowland river with

a focus on portions of the channel and floodplain that experience inundation intermittently. Our first objective was to determine the efficacy with which our STICLs can be employed to analyze surface-water connectivity in not only the longitudinal dimension, but also along the lateral and vertical dimensions. Comparisons between the data logger records and those of *Q* and *PPT* reveal that the STICLs respond well to hydrologic events that they experience in the field. We think that our STICLs perform adequately in allowing us to infer surface-water connectivity across the three fluvial dimensions, but our predictions could be improved if we better account for the uncertainty in the STICL predictions so that they can be included in our determinations of the durations of inundation and the associated temporal variations to surface-water connectivity. Our second objective was to determine the hydrologic and morphological factors that influence the observed differences in surface-water connectivity. Hydrologically, the most obvious difference across the five TPs is the amount of rainfall the area received and the associated rise in *Q*. While *PPT* needs to occur in bunches so *Q* rises enough to inundate the elevated portions of the channel where our data loggers are installed, the duration of the surface-water connectivity in higher portions of the channel and within the floodplain will be greater if the *PPT* does not occur in a brief/flashy event. Moreover, the duration of inundation for TP4 was greater because of the storm-surge that coincided with the progression of Hurricane Harvey and this highlights the need of considering these types of processes when studying surface-water connectivity in coastal environments. Morphologically, our study reach of Mission River flows through two distinct geologic units with upstream portions being Pleistocene fluviatile

terrace and the downstream portions being Holocene alluvium. There are several STICLs with the same estimate of Q_{min}, but lie within different geologic units and they provide a means for analyzing if the geologic template plays a role in the duration of inundation reported by our STICLs. TP4 is where most of our STICLs are active and we use readings from this TP as the basis for the comparisons between STICLs with the same Q_{min} but that lie within different geologic units. For STICLs with a Q_{min} that has inundation largely contained within the main channel ($Q_{min} \leq 35.4$ m^3/s), the mean inundation duration for alluvium STICLs 27% greater than that for the fluviatile terrace STICLs. The same cannot be said for STICLs with a Q_{min} that is associated with some floodplain inundation but not overbank inundation for the reach ($44.9 \leq Q_{min}$ 108.1 m^3/s). STICLs within the fluviatile terrace portion of the reach have an average inundation duration that is 59% greater than that of the alluvium STICLs with the same Q_{min}. There is no consistent pattern that can be used to infer if differences in the geologic units has an affect on the duration of surface-water connectivity and this is further highlighted by four STICLs within the alluvium portion that each have a Q_{min} of 55.1 m^3/s but they all have somewhat different inundation durations. We propose that more research is needed to determine if morphological differences result in temporal differences to surface-water connectivity for locations in a channel-floodplain system that are inundated with streamflows of the same magnitude.

Low-cost data loggers that can record ambient temperature and *EC* have found utility within the literature when the intermittence of stream or wetland water at a point or channel reach is the interest. The STICL designs provided by Chapin et al. (2014) are

well suited for these types of analyses in that they are relatively affordable and easy to develop; they can record measurements at a high radiometric resolution and allow the use of a wide variety of temporal resolutions; and they have a high storage potential with the ability to store ~300 days of readings at a 15-minute logging interval. While they have been readily used in montane environments with semi-arid (e.g., Chapin et al. (2014)) and temperate (e.g., Kaplan et al. (2019) and Paillex et al. (2019)) climates; as well as in the arctic (e.g., Gillman et al. (2017)), we present the first case-study of their use within a coastal lowland riverine environment with very turbid flows that can be affected by coastal processes, a climate with very high humidity and temperatures in the summer months, and an extreme variability in precipitation that can produce large floods. Between both phases of data loggers that we deployed, we are only able to report findings from 2/3 of our data loggers because the other 1/3 of our data loggers were washed away during high flow events or damaged due to failure of electronic components or vandalism from people and/or animals. With these issues in mind, below we provide some "lessons learned" with regard to using these types of STICLs in lowland coastal environments.

1. Exploit existing water quality records for your study site to determine the appropriate calibration range of electrical conductivity values for your data loggers. The U.S. Geological Survey, U.S. Environmental Protection Agency, state environmental/resource agencies, local/regional water resource managers, and the grey literature are good places to search for these types of data.

2. The types of data loggers that we use here require modifications that involve making holes in the water-proofing cap. When deploying in lowland coastal environments, the choice of epoxy that is used to re-seal the cap after adding the protruding probes should be rated for fresh and marine water. The epoxy should also be capable of withstanding high heat and humidity that can occur during the summer months. Moreover, the high humidity and clay content in the soils allows flood waters to sit on the landscape for an extended amount of time and the epoxy seal should also be rated for continuous inundation.
3. The precipitation patterns and morphology allow lowland coastal rivers to experience large floods with a high degree of stream power. Moreover, the channel bed and banks are generally composed of unconsolidated sediments that are constantly being reworked during high flow events. This creates a high potential for data loggers to be washed away if they are not secured properly. Data loggers should be secured properly with stakes that are at least 46 cm (18 in) long and a tether with sufficient strength to hold the STICL and housing. The materials that the stake and tether are made of should also be able to sustain the wear of extended inundation and exposure to constant sunlight, humidity, and soils with high clay and organic content.
4. Vandalism of data loggers by people and animals can be problematic. While properly labeling data logger housings can help prevent some vandalism, deploying STICLs in locations that are not frequented by people is a good practice. Moreover, large livestock such as cattle and horses can damage STICLs and/or their housing by

trampling; thus STICLs should also be deployed in locations that are also not frequented by large animals if possible.

Conclusions

Analyses that utilize concepts of surface-water connectivity have been important in advancing the understanding of physical, chemical, and biological process of lowland rivers (Hudson et al., 2013). Field-based data loggers that can be used to infer flow intermittency and the associated surface-water connectivity have found utility in studies of ephemeral channels (Chapin et al., 2014), but no previous studies have been performed that utilize data loggers to analyze data loggers in portions of perennial channels and floodplains that experience inundation intermittently and that is what we have performed here. To accomplish this task we developed and calibrated STICLs as proposed by Chapin et al. (2014) and deployed them along a reach of the coastal lowland Mission River. This allowed us to determine if they can be used to monitor surface-water connectivity in portions of the main channel and floodplain that experience inundation and streamflow intermittently. Our results show that the *EC* records from our STICLs can capture flood inundation dynamics and how it affects surface-water connectivity. Although, our estimates of surface-water connectivity dynamics can be improved if we better account for how *EC* can vary with temperature and by handling the uncertainty in our STICLs readings in a more explicit manner. This is something that we will pursue in the future and it will allow us to more confidently determine if hydrologic and morphologic factors can influence the dynamics of surface-water connectivity.

We found STICLs as a useful tool in monitoring surface-water connectivity along our study reach and it will provide a means for better understanding the duration of time that the perennial main channel interacts with other portions of the riverine landscape. Moreover, STICLs and other data logger designs that are aimed at monitoring the intermittency of water can be useful in validating hydrodynamic models and datasets of flood inundation. Also, our STICLs also responded well to precipitation events and they can potentially be used to validate precipitation datasets over an area. Further, environmental flow policies and management schemes often call for increasing hydrologic connectivity between the main channel of a river and the surrounding landscape (at least temporarily). A common practice for achieving this type of goal is prescribed releases from surface-water reservoirs that are aimed at connecting the river with floodplain/riparian habitats (Galat and Lipkin, 2000, Poff, 2014, Richter and Thomas, 2007). Deploying a network of field-based data loggers along the riverine landscape of interest can be used to monitor if the magnitude and duration of the reservoir releases achieve the connectivity goals and allow for these schemes to be modified if needed. The STICLs we used in our analysis are an exciting tool that will allow riverine processes to be studied in more detail and we propose that more analysis of the type performed here are needed so that formal approaches and frameworks for deploying these types of data loggers within lowland landscapes can become developed.

References

AMOROS, C. & ROUX, A. L. 1988. Interaction between water bodies within the floodplains of large rivers: function and development of connectivity. Münstersche Geographische Arbeiten,, 29, 125-130.

ARISMENDI, I., DUNHAM, J. B., HECK, M. P., SCHULTZ, L. D. & HOCKMAN-WERT, D. 2017. A Statistical Method to Predict Flow Permanence in Dryland Streams from Time Series of Stream Temperature. Water, 9, 1-13.

BHAMJEE, R. & LINDSAY, J. B. 2011. Ephemeral stream sensor design using state loggers. Hydrology and Earth System Sciences, 15, 1009-1021.

BLASCH, K. W., FERRE, T. P. A., CHRISTENSEN, A. H. & HOFFMANN, J. P. 2002. New Field Method to Determine Streamflow Timing Using Electrical Resistance Sensors. Vadose Zone Journal, 1, 289-299.

BLASCH, K. W., FERRÉ, T. P. A. & HOFFMANN, J. P. 2004. A statistical technique for interpreting streamflow timing using streambed sediment thermographs. Vadose Zone Journal, 3, 936-946.

CASTILLO, C. R., GÜNERALP, I., HALES, B. & GÜNERALP, B. In-Preparation. Scale-free structure of surface-water connectivity in a lowland river-floodplain landscape. Nature Geoscience.

CHAPIN, T. P., TODD, A. S. & ZEIGLER, M. P. 2014. Robust, low-cost data loggers for stream temperature, flow intermittency, and relative conductivity monitoring. Water Resources Research, 50, 6542-6548.

CONSTANTZ, J., STONESTROM, D., STEWART, A. E., NISWONGER, R. & SMITH, T. R. 2001. Analysis of streambed temperatures in ephemeral channels to determine streamflow frequency and duration. Water Resources Research, 37, 317-328.

CSWRCB 2004. Electrical Conductivity/Salinity Fact Sheet. Clean Water Team Guidance Compendium for Watershed Monitoring and Assessment. Sacramento, CA: California State Water Resources Control Board.

DAVIS, N. A. & SMITH, E. H. 2013. Dynamics of a community of dominant woody riparian species along a coastal river of Texas. Southwestern Naturalist, 58, 286-298.

ELLIOTT, L. F., TREUER-KUEHN, A., BLODGETT, C. F., TRUE, C. D., GERMAN, D. & DIAMOND, D. D. 2014. Ecological System of Texas: 391 Mapped Types. In: TEXAS PARKS AND WILDLIFE DEPARTMENT & TEXAS WATER DEVELOPMENT BOARD (eds.). Austin, TX.

FEMA 2014. Flood Insurance Study: Refugio County, Texas and Incorporated Areas. Flood Insurance Studies. Denton, TX: Federal Emergency Management Agency.

FULBRIGHT, T. E., DIAMOND, D. D., RAPPOLE, J. & NORWINE, J. 1990. The Coastal Sand Plain of Southern Texas. Rangelands, 12, 337-340.

GALAT, D. L. & LIPKIN, R. 2000. Restoring ecological integrity of great rivers: Historical hydrographs aid in defining reference conditions for the Missouri River. Hydrobiologia, 422-423, 29-48.

GILLMAN, M. A., LAMOUREUX, S. F. & LAFRENIÈRE, M. J. 2017. Calibration of a modified temperature-light intensity logger for quantifying water electrical conductivity. Water Resources Research, 53, 8120-8126.

GOULSBRA, C. S., LINDSAY, J. B. & EVANS, M. G. 2009. A new approach to the application of electrical resistance sensors to measuring the onset of ephemeral streamflow in wetland environments. Water Resources Research, 45, 1-7.

HUDSON, P. F., SOUNNY-SLITTINE, M. A. & LAFEVOR, M. 2013. A new longitudinal approach to assess hydrologic connectivity: Embanked floodplain inundation along the lower Mississippi River. Hydrological Processes, 27, 2187-2196.

ISHIYAMA, N., AKASAKA, T. & NAKAMURA, F. 2014. Mobility-dependent response of aquatic animal species richness to a wetland network in an agricultural landscape. Aquatic Sciences, 76, 437-449.

JAEGER, K. L. & OLDEN, J. D. 2012. Electrical resistance sensor arrays as a means to quantify longitudinal connectivity of rivers. River Research and Applications, 28, 1843-1852.

JENSEN, C. K., MCGUIRE, K. J., MCLAUGHLIN, D. L. & SCOTT, D. T. 2019. Quantifying spatiotemporal variation in headwater stream length using flow intermittency sensors. Environmental Monitoring and Assessment, 191, 1-19.

KAPLAN, N. H., SOHRT, E., BLUME, T. & WEILER, M. 2019. Monitoring ephemeral, intermittent and perennial streamflow: a dataset from 182 sites in the Attert catchment, Luxembourg. Earth System Science Data, 11, 1363-1374.

LEGLEITER, C. J. & KYRIAKIDIS, P. C. 2008. Spatial prediction of river channel topography by kriging. Earth Surface Processes and Landforms, 33, 841-867.

MEITZEN, K. M., DOYLE, M. W., THOMS, M. C. & BURNS, C. E. 2013. Geomorphology within the interdisciplinary science of environmental flows. Geomorphology, 200, 143-154.

NELSON, J. & TOLAN, J. 2008. Final Historical Data Review on Mission River and Aransas River Tidal. Austin, TX: Texas Parks and Wildlife Department.

NORWINE, J. & JOHN, K. 2007. The changing climate of South Texas, 1900-2100 : problems and prospects, impacts and implications, Kingsville, TX : CREST-RESSACA, Texas A & M University-Kingsville, 2007.

NUECES RIVER AUTHORITY 2019. Clean Rivers Program. In: NUECES RIVER AUTHORITY (ed.). Corpus Christi, TX. Available: https://www.nueces-ra.org/CP/CRP/SWQM/

PAILLEX, A., SIEBERS, A. R., EBI, C., MESMAN, J. & ROBINSON, C. T. 2019. High stream intermittency in an alpine fluvial network: Val Roseg, Switzerland. Limnology and Oceanography.

POFF, N. L. 2014. Rivers of the anthropocene? Frontiers in Ecology and the Environment, 12, 427.

POOLE, G. C. 2002. Fluvial landscape ecology: Addressing uniqueness within the river discontinuum. Freshwater Biology, 47, 641-660.

PRISM CLIMATE GROUP 2019. PRISM Gridded Climate Data. In: PRISM CLIMATE GROUP - OREGON STATE UNIVERSITY (ed.). Eugene, OR. Available: http://prism.oregonstate.edu/.

RICHTER, B. D. & THOMAS, G. A. 2007. Restoring environmental flows by modifying dam operations. Ecology and Society, 12, 1-26.

SARA 2016. Strategic Mapping Program (StratMap) - San Antonio River Authority Imagery. In: SAN ANTONIO RIVER AUTHORITY (ed.). Texas Natural Resource Information System. Available: https://webservices.tnris.org/arcgis/services/StratMap/StratMap16_NC_CIR_12in_SARA/ImageServer/WMSServer.

SCHOENBAECHLER, C. & GUTHRIE, C. G. 2011. Coastal Hydrology for the Mission-Aransas Estuary. Austin, TX, USA: Texas Water Development Board: Surface Water Resources Division - Bays and Estuaries Program.

SIEBERS, A. R., PAILLEX, A. & ROBINSON, C. T. 2019. Flow intermittency influences the trophic base, but not the overall diversity of alpine stream food webs. Ecography, 42, 1523-1535.

U.S. ENVIRONMENTAL PROTECTION AGENCY. 2012. 5.9 Conductivity [Online]. U.S. Environmental Protection Agency. Available: https://archive.epa.gov/water/archive/web/html/vms59.html [Accessed 16 October 2019 2019].

USGS 2016. National Water Information System data available on the World Wide Web (USGS Water Data for the Nation). In: U.S. GEOLOGICAL SURVEY (ed.). Available: https://waterdata.usgs.gov/nwis/inventory/?site_no=08189500&agency_cd=USGS.

USGS-TWSC 2014. Geologic Database of Texas. In: U.S. GEOLOGICAL SURVEY - TEXAS WATER SCIENCE CENTER (ed.). Austin, TX.

WOHL, E. 2017. Connectivity in rivers. Progress in Physical Geography, 41, 345-362.

WOHL, E., BRIERLEY, G., CADOL, D., COULTHARD, T. J., COVINO, T., FRYIRS, K. A., GRANT, G., HILTON, R. G., LANE, S. N., MAGILLIGAN, F. J., MEITZEN, K. M., PASSALACQUA, P., POEPPL, R. E., RATHBURN, S. L. & SKLAR, L. S. 2018. Connectivity as an emergent property of geomorphic systems. Earth Surface Processes and Landforms, 44, 4-26.

CHAPTER V

CONCLUSIONS

Summary

Terrain-Based Analysis of Surface-Water Connectivity

We use a gridded lidar-based digital terrain model (DTM) and historical streamflow records to develop a gridded digital relative elevation model (DREM) where each grid-cell depicts the relative height difference between the land-surface at the grid-cell location and the river water-surface at the time of lidar data acquisition. We then use this DREM to delineate hydrologic facets that divide the landscape into sets of patches and represent the drainage structure within the riverine landscape. By thresholding the DREM, we also simulate surface-water inundation within the riverine landscape for 80 different streamflow conditions and analyze the associated surface-water connectivity between the facets using methods from graph theory.

Our results indicate that Mission River and the surrounding landscape experience wide-spread inundation for streamflow conditions below published bankfull estimates. This is due to backwater flooding into tributaries, secondary channels, and other low-lying areas within the floodplain. With regards to surface-water connectivity, we use six graph theoretical metrics to describe connectivity and associated system attributes. All six of our metrics have a nonlinear relationship with river-stage. Moreover, the connectivity is largely maintained by facets that behave like hubs. These hub-like facets contain the main channel and the aforementioned floodplain features that allow

backwater flooding to spread throughout the riverine landscape and these locations should be considered as prime candidates for preservation if river-floodplain connectivity is a concern.

Surface-Water Connectivity Patterns

We developed a hydrodynamic model informed by a detailed DTM to simulate surface-water inundation within Mission River and the surrounding landscape. Informed by historical flow records and a detailed Flood Insurance Study for Mission River we then simulated 23 steady streamflow scenarios that span the historical range of flow records. We then analyze the surface-water connections between the river and two sets of ecological habitat patches by constructing spatially explicit networks for each streamflow scenario and analyzing them with empirical methods from complex network theory.

Our results indicate that the configuration of the landscape network created by surface-water connections for several of the simulated streamflow conditions can be considered scale-free. Networks with scale-free configuration have been widely studied across many disciplines because of their universal structure and function. This is the first documented example of a (roughly) scale-free network structure that is induced by surface-water connections within a river-floodplain landscape. Riverine landscapes are composed of multiple subsystems across space and the findings we present here highlight how these subsystems interact during inundation events. This is important because a better understanding of the particular pattern associated with these interactions

can provide more insight into the feedbacks between the individual processes that developed the heterogeneity in riverine landscapes that allowed the pattern to arise.

Monitoring Surface-Water Connectivity with Data Loggers

We constructed and calibrated a set of low-cost data loggers that are intended to be deployed in the field for the purposes of monitoring surface-water inundation and the associated connectivity that it creates within a riverine landscape. Specifically, we deployed our data loggers in portions of the Mission River main channel and floodplain that experience intermittent surface-water inundation to monitor the frequency and duration with which surface-water connects them with the perennial portions of the main channel. Given this need, we employed Stream Temperature, Intermittence, and Conductivity loggers (STICLs) because they were designed to be used in a somewhat similar fashion within channels of ephemeral streams. We had STICLs deployed within the Mission River landscape during five time-periods (TPs) within the window of 25-May-2016 to 31-Dec-2018. While the number of deployed STICLs varied by TP (one TP had five and another had twenty-three), STICLs were deployed at eight general locations within the riverine landscape with some being in a Pleistocene fluviatile terrace portion and others being within a Holocene alluvium portion. This allowed us to compare the time-series produced by our STICLs with surface-water inundation maps and time-series of precipitation and river discharge to determine if the predicted presence/absence of water from our STICLs can be considered accurate.

Our results indicate that the records produced by our STICLs are well suited for identifying the time and duration of hydrologic events that resulted in the wetting and/or

inundation of the location at which the respective STICLs were installed. With regards to the frequency and duration of inundation, STICLs deployed at relatively lower elevations within the vertical profile of the landscape were generally inundated more often and for longer durations that STICLs at relatively higher elevations. Moreover, the electrical conductivity (*EC*) of the inundating waters that our STICLs record allow us to compare them with historical water quality records in order to estimate the source of the inundating waters. Riverine flooding was the primary source of inundation for our STICLs, but intense rainfall and coastal storm-surge were found to also cause some inundation for some of the hydrologic events that our STICLs experienced. These results indicate that STICLs are a useful tool when monitoring surface-water connectivity in a quantifiable fashion is the interest.

Main Conclusions

The research presented in this Dissertation operated under the main objective of building towards the development of a framework for quantifying landscape connectivity induced by surface-water connections within lowland riverine landscapes. We employed some underutilized methods and tools to address this objective and our findings have allowed us to make the following main conclusions:

1. Theory and methods used in graph and network analysis provide a powerful set of tools that are well-suited for quantifying dynamic connectivity over a landscape. We propose that graph/network analysis should be adopted by more river scientists because it has been widely used by other disciplines and this will allow better communication amongst scientists and resource managers.

2. Lowland riverine landscapes are characterized as having dynamic surface-water connections that create an expanding and contracting network that conceptually meets many of the criteria of scale-free graphs/networks. The structure and function of scale-free networks within numerous application domains has been widely studied in the literature and this knowledge-base can help increase our basic understanding of how energy, matter, biota, and information is exchanged between components of the riverine landscape system. We propose that more empirical research is needed from other lowland riverine landscapes to determine if this is a common pattern found within these types of environments.
3. Stream Temperature, Intermittence, and Conductivity loggers (STICLs) are another set of tools that will provide a means for quantifying surface-water connectivity within riverine landscapes. In particular, they can be used to monitor the frequency and duration of connectivity between the river and floodplain. Moreover, STICL records and other environmental data can be used to infer the hydrologic mechanisms creating the surface-water inundation and associated connectivity.

We believe that the research presented in this Dissertation has allowed us to address the main objective well. Connectivity is a popular term and concept within the natural sciences and the methods and tools presented here provide a means for quantifying connectivity within lowland riverine environments.

APPENDIX A

SUPPORTING INFORMATION FOR CHAPTER II

Introduction

This Appendix is provided to further describe some datasets and methods that were utilized in our analysis. In particular, this document describes four components of the research. *DTM Data and Generation* describes the generation of a digital terrain model (DTM) that was vital to all portions of this research. *Rating Curve Fitting* describes the fitting and performance of a rating curve that is used to predict stage as a function of discharge. This is followed by *Return Period for Streamflows* that describes fitting a probabilistic distribution to peak flow statistics from streamflow records collected within the study area. Finally, *Quantile Divisions Used in Determining Geometric Influence on Connectivity* shows how our set of nodes/HFs were divided into quantiles to determine the influence that geometric properties have on hydrologic surface connectivity within the floodplain.

DTM Data and Generation

DTM Data

LiDAR point clouds using a near-infrared channel were collected using an aerial platform with an LH Systems ALS50 LiDAR system on June 1-15, 2006 by Sanborn Mapping Company, Inc. under the auspices of the Texas Water Development Board (TWDB) and the U.S. Federal Emergency Management Agency (FEMA). These point clouds have a mean point density of 1.4 m with a horizontal accuracy that meets FEMA

standards (root mean square error (RMSE) ≈ 3.4 m) and vertical accuracy of ~18.5 cm. A DTM of the study area with a 5-m spatial resolution was generated using these LiDAR point clouds. Mean daily river stage for Mission River during LiDAR acquisition was 1.06 m (~1.4 m above sea level). The mean daily flows are skewed by a storm event that occurred in the first week of LiDAR acquisition (stage ranged from 0.7 to 2.9 m during acquisition period). We made inquiries to TWDB and Sanborn to further pinpoint the time-period associated with LiDAR acquisition in order to not rely on a mean value for the two-week window, but dates for the acquisition time-period were not available at a higher temporal resolution. The LiDAR data we use are freely available and they were downloaded in LAS format with NAD83 zone-14N and NAVD88 as the horizontal and vertical datums, respectively, from the National Oceanic and Atmospheric Administrations (NOAA)'s Digital Coast website (http://coast.noaa.gov/digitalcoast/data/coastallidar). Point clouds were classified and reviewed by the NOAA Office of Coastal Management in order to filter ground (or bare-earth) classified points from the rest of the point cloud.

DTM Generation

Bare-earth point clouds in LAS format were converted to a multipoint shapefile (with 22,701,500 points or spot heights) using ArcGIS 10.2 (ESRI, 2014) to generate a raster-based digital terrain model (DTM). For this purpose, we performed inverse distance weighted (IDW) interpolation utilizing the Geostatistical Wizard from ArcGIS in order to determine the parameter specifications for the operation. We used an oval kernel with a 2:1 ratio in major and minor semi-axies in the interpolation with the major

axis oriented in the north-south direction (floodplain has general north-south orientation). Optimization of the decay parameter (p) yielded a value of 3.5 for 60 sample points (n). The kernel was divided into quadrants with divides that were perpendicular to the major and minor oval axes with each quadrat containing 15 sample points. With respect to LiDAR the spot heights, the surface (i.e., DTM) has a vertical RMSE of 8.4 cm. The Geostatistical Analyst layer was then converted to GeoTIFF raster format with 5-m spatial resolution.

The near-infrared wavelength utilized by the airborne LiDAR scanner resulted in voids within point-clouds over areas with water due to signal absorption. Voids yielded interpolation errors and a lack of "hydrological correctness" due to "digital dams" within active channels of the floodplain. A "Fill" operation, from within the ArcGIS Spatial Analyst toolbox, was used to fill any artificial or real depressions in the original DTM. The filled-DTM was also inverted so that the Fill procedure could be used to remove "peaks" within the dataset. This analysis is only interested in strictly establishing hydrological correctness within the main and other active channels; thus the channel banks were manually delineated using high resolution aerial photography and these boundaries were used to extract the channels. Synthetic LiDAR sample points were established within the delineated channel boundaries. Elevation values from the filled-DTM were assigned to synthetic and original LiDAR sample points that fell within the channel boundaries. An IDW interpolation was conducted with original spot height values outside of the active channels and assigned/synthetic spot height values within the channel boundaries. The IDW interpolation utilized an oval kernel with a 2:1 ratio in

major and minor semi-axies was used in the interpolation with a decay parameter (p) of 4 and 60 sample points (n). Moreover, the kernel was divided into quadrants with divides that were perpendicular to the major and minor oval axes each containing 15 sample points. With respect to original and synthetic spot heights, the newly generated surface has a vertical RMSE of 8.2 cm.

The newly-interpolated DTM still contained numerous digital dams within the channel. A Python script was developed that removes digital dams by employing a moving window that travels along stream centerlines for each channel. This moving window identifies the upstream and downstream elevations within the window and assigns elevation values to pixels within the window using linear interpolation in order to ensure downstream routing for pixels. Moreover, a stream burning algorithm was also implemented that imposes a 0.1mm gradient between an upstream and downstream pixel within the main channel.

A DTM with 5-m spatial resolution was delineated using IDW interpolation (Figure II-1c). Within the geographic extent of the study area, elevation ranges from 0 to 19 m above sea level with a mean elevation of 8.2 m. The greatest variation in elevation occurs within the geomorphological floodplain that has a general north-south trend and gradually widens and deepens in the downstream direction. The relatively high spatial resolution of our DTM (5-m) allows for floodplain features such as secondary channels, natural levees, and bluffs that are littered throughout the study area to be identified visually. Influences to DTM interpolation error from man-made structures within developed areas and along active channels are present throughout DTM. No effort is

made to rectify the remaining interpolation errors because most developed areas are not included within the floodplain and it was ensured that the DTM was hydrologically correct.

The original LiDAR data has a horizontal and vertical accuracy of 3.4 m and 18.5 cm (based on root mean square error (RMSE)), respectively, for Refugio and Aransas counties. We are mostly concerned with the vertical accuracy of our DTM and when our delineated surface is compared to 9 U.S. National Geodetic Survey (NGS) that fall within the geographic extent of our study area, our DTM has a vertical RMSE of 74 cm and mean absolute error (MAE) of 56 cm. The relatively large degree of error in our DTM is potentially skewed by elevation values within the Town of Refugio where man-made structures can complicate LiDAR derived elevation measurements. Three of the NGS benchmarks fall within Refugio and our RMSE and MAE decline to 35 and 25 cm, respectively, if the Refugio benchmarks are not included in the calculation. Our analysis is only concerned with elevation within the floodplain, but unfortunately there are no NGS benchmarks within our delineated floodplain. Although the limited number of man-made structures within the floodplain leads us to assume that our DTM error is not significantly different from our estimates using all benchmarks (RMSE = 74 cm and MAE = 56 cm) within the study area.

Rating Curve Fitting

Our analysis of hydrologic impedance allowed the determination of the stage that is needed for a respective hydrologic facet to become hydrologically connected to the main channel. Combing this information with a fitted rating curve (curve parameters and

goodness-of-fit shown in Table A-1) for stage and discharge at the U.S. Geological Survey gaging station on Mission River below Refugio, TX (Gage ID: 08189500).

Table A-1. Equation and parameterization used in the four-parameter logistic function that predicts the river-stage associated with a particular discharge value. The parameters of the logistic function (a, b, c, d) are the minimum asymptote, hill slope, inflection point, and maximum asymptote, respectively. The goodness-of-fit was also evaluated using the coefficient of determination (R2), slope (m) of the observed and predicted slope line, p-value for the confidence level of the estimated slope value, and the root mean squared error (RMSE) and mean absolute error (MAE) between the observed and predicted river stage values.

Equation	**Parameter Values**			
	a	***b***	***c***	***d***
$f(x) = d + \frac{a-d}{1+\left(\frac{x}{c}\right)^b}$	0.60	0.82	97.76	11.62

Goodness-of-Fit Indicators				
R^2	***m***	***p-value***	***RMSE***	***MAE***
0.98	0.98	< 0.01	0.11	0.05

Return Period for Streamflows

In our determination of the river-stage values that would result in a hydrologic connection for each respective HF, we also used peak-flow statistics to determine the associated return period for the respective streamflows. The mapping of return period helps describe the spatial variations in hydrologic connectivity. Normal, Log-Normal, Gamma, Log-Gamma, Pearson Type III, Log-Pearson Type III, and Generalized Extreme Value (GEV) distributions were all fit to peak river-stage values. We found the GEV distribution to fit the peak-flow data best (Table A-2). Moreover, tests for exponentiality (e.g., Kolmogorov-Smirnov test for the distribution's parameter; Lilliefors' test for exponentiality from Lilliefors (1969)) indicated that peak-flows could follow a type of exponential distribution (Table A-3).

Table A-2. Goodness-of-fit indicators scores between the observed peak discharge and fitted frequency distributions. Observed values are from the 0189500 gage on Mission River (see Figure II-1c).

Distribution	R^2	*m*	*NSE*	*d*	*PBIAS*	*RSR*	*MSR*
Normal	0.63	0.76	0.61	0.89	**0.00**	11649.8	155.3
Log-Normal	**0.97**	1.40	0.77	0.96	-15.35	6786.8	90.5
Gamma	0.95	**0.86**	0.94	0.98	4.78	1640.2	21.9
Log-Gamma	0.89	2.12	-0.89	0.82	-36.32	55851.7	744.7
Pearson Type III	0.96	**0.86**	**0.95**	**0.99**	4.90	**1528.8**	**20.4**
Log-Pearson Type III	0.93	0.74	0.89	0.96	5.43	3172.5	42.3
Generalized Extreme Value	**0.97**	**1.02**	**0.97**	**0.99**	**-0.14**	**911.6**	**12.2**

The two best scores for each goodness-of-fit indicator are shown in bold. R2: coefficient of determination for linear regression (ranges between 0 and 1 with higher values indicating a better fit); m: slope of the linear regression (range between -∞ and ∞ with values closer to 1 indicating a better fit); NSE: Nash-Sutcliffe model efficiency (ranges between -1 and 1 with values closer to 1 indicating a better fit); d: index of agreement (ranges between 0 and 1 with values closer to 1 indicating a better fit); PBIAS: percent bias (ranges between -∞ and ∞ with values closer to 0 indicating a better fit); RSR: root mean squared error (RMSE) divided by the observed standard deviation (ranges between 0 and ∞ with values closer to 0 indicating a better fit); MSR: mean absolute error divided be the observed standard deviation (ranges between 0 and ∞ with values closer to 0 indicating a better fit).

Table A-3. Statistical tests for exponentiality of peak discharge from the 0189500 gage on Mission River (see Figure II-1c).

Statistical Test	*D*	p-value
Kolmogorov-Smirnov	0.110	0.341
Lilliefors	0.109	0.135

The Kolmogorov-Smirnov test was applied to the rate parameter of the exponential distribution where D is the maximum discrepancy between the fitted and theoretical distribution. Similarly, Lilliefors test for exponentiality also determines the maximum discrepancy between the fitted and theoretical distribution. A p-value is also provided for both tests with a null hypothesis of no exponentiality in the observed distribution. The p-value > 0.05 for both tests, thus the possibility of the peak flow data following an exponential distribution cannot be rejected.

Quantile Divisions Used in Determining Geometric Influence on Connectivity

The six variables used to describe geometric properties of our facets include (1) facet area; (2) the ratio between the minor and major axes ($axis_{min}$ and $axis_{maj}$, respectively) for the minimum bounding ellipse for each facet; (3) the mean distance from the geometric centroid of a facet to the geometric centroid of all other facets within a 3000 m buffer; (4) mean slope for the terrain within an facet; (5) length of delineated channel for each facet; and (6) the minimum distance to the main channel facet. To assess how these geometric properties influence the quantification of connectivity; we divided the facets into quantiles using the six aforementioned geometric variables. Table A-4 summarizes the value range and samples associated with each geometric variable.

By design, the range in sample size for each quantile grouping is similar (range: 234 – 236). However, the similarity in the range of values is not always the case when it comes to the values for the geometric variables. For example, some geometric variables have a fairly similar range ($Axis_{min}$ /$Axis_{maj}$ and mean distance between HF centroids), while the other variables tend to have more skewed distributions.

Table A-4. The six geometric variables used in the assessment of how geometric properties amongst and between hydrologic facets influences the overall assessment of connectivity. The value for each variable is computed for every facet than they are subdivided into groups using quantiles (Q1, Q2, Q3, and Q4). The value ranges for each variable and sample size of HFs included in each quantile group are also provided.

Geometric Variable	Range in Values (sample size)			
	Q1	***Q2***	***Q3***	***Q4***
Facet area (1000 m^2)	0.20 - 9.20 (235)	9.23 - 17.82 (234)	17.85 - 31.85 (235)	31.90 – 3,420 (235)
$Axis_{min}/Axis_{maj}$ for minimum bounding ellipse (ratio)	0.07 - 0.38 (233)	0.38 - 0.50 (235)	0.50 - 0.63 (235)	0.63 - 0.98 (236)
Mean distance between facets that are within 3000 m	1.58 - 1.72 (235)	1.72 - 1.77 (234)	1.77 - 1.86 (235)	1.86 - 2.18 (235)
Mean slope of facet terrain (%)	0.15 - 1.29 (235)	1.30 - 2.08 (234)	2.08 - 3.21 (235)	3.21 - 14.46 (235)
Delineated channel length within facet (m)	0.00 - 62.07 (235)	62.43 - 136.60 (234)	137.4 - 262.6 (235)	263.1 – 30,570 (235)
Distance to main channel facet (m)	0.00 - 32.02 (234)	35.35 - 245.00 (235)	245.1 - 552.5 (235)	554.70 – 1,702 (235)

References

ESRI 2014. ArcGIS 10.2 Desktop. 10.2.2 ed. Redlands, CA, USA: ESRI.

LILLIEFORS, H. W. 1969. On the Kolmogorov-Smirnov Test for the Exponential Distribution with Mean Unknown. Journal of the American Statistical Association, 64, 387-389.

APPENDIX B

SUPPORTING INFORMATION FOR CHAPTER III

Introduction

This Appendix is provided to further describe some of the datasets and methods that were utilized in our analysis. In particular, this document describes four components of the research. *Hydrological Regime for Mission River* provides a quantitative description of the historical flow regime for Mission River using data from a gaging station. *Calibration of Hydrodynamic Model* shows how our hydrodynamic model outputs compare to published estimates of the water surface elevation from Flood Insurance Studies. *Description of Land Classification* describes the two landscape patch datasets used in our analysis. This is followed by *Spatial Datasets Developed Using Hydrodynamic Simulations* describes the depth of inundation datasets developed using hydrodynamic model simulations and the overlay analysis that is conducted between these datasets and the land classifications. Finally, *Other Topological and Algebraic Network Metrics* that describes the other network connectivity measures used in our analysis.

Hydrological Regime for Mission River

The study area has a subhumid-to-semiarid subtropical climate with extreme variability in precipitation (Davis and Smith, 2013, Fulbright et al., 1990, Norwine and John, 2007). Streamflows at the U.S. Geological Survey gaging station below Refugio (Station Number: 08189500) are also highly variable. Mean daily discharge (Q) ranges

from 0 to 1903 m^3/s with a mean of 3.5 m^3/s (Figure B-1b; mean daily *Q* records for time period of 01-Jul-1939 to 31-Dec-2018). Similarly, the distribution of mean daily stage (*h*) is also highly variable with a range of 0 to 11.3 m with a mean of 0.9 m (Figure B-1a). Using the rating-curve (*h* plotted against *Q*; Figure B-1c), bankfull conditions occur at the 08189500 gage with a discharge (*Q*) of 211 m^3/s and *h* of 8.0 m and this is determined by using the break in the relationship between *h* and *Q*. This break indicates that *h* will not rise with *Q* at the previous rate because riverine water has spread out onto the floodplain. While there are good historical records for Mission River flows at the 08189500 gage, the main channel and floodplain widen downstream as the main channel becomes more sinuous. This results in high variation of hydraulic and geomorphic conditions that can complicate the application of point-samples streamflow measurements to other portions of the river reach (Hudson et al., 2013, Tockner et al., 2000). Moreover, the lower half of the main channel within the study area is influenced by tidal processes (Davis and Smith, 2013, Nelson and Tolan, 2008), that further complicates hydraulic and geomorphic conditions.

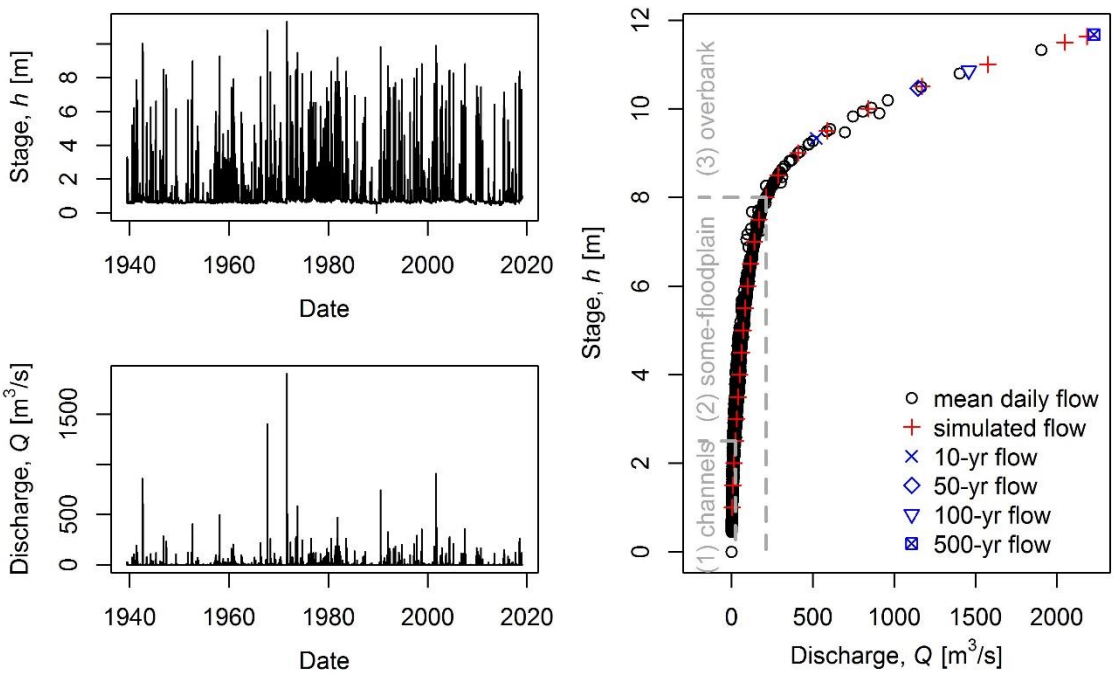

Figure B-1. Time-series' of mean daily (a) stage and (b) discharge for Mission River at the USGS stream gage at Refugio, TX (Gage ID: 08189500) from 1-Jul-1939 to 31-Dec-2018. (c) Rating-curve for the location at the 08189500 gage created using the mean daily data in (a) and (b). The flow scenarios used in the network analysis and model calibration are also plotted. The characteristics of the three phases of the inundation process ((1) channel-inundation, (2) some-floodplain-inundation, and (3) overbank-inundation) are also shown on the plot. (Note: Hydrodynamic model is calibrated to flood profiles from a FEMA detailed Flood Insurance Study for Refugio County (FEMA, 2014).)

Calibration of Hydrodynamic Model

We calibrate our hydrodynamic model to longitudinal water surface elevation (WSE) profiles from a recent Federal Emergency Management Agency (FEMA) flood insurance study (FIS) (FEMA, 2014). The downstream limit of the FIS is roughly at the same limit as our study area and a comparison of the WSE profiles is shown in Figure B-6.

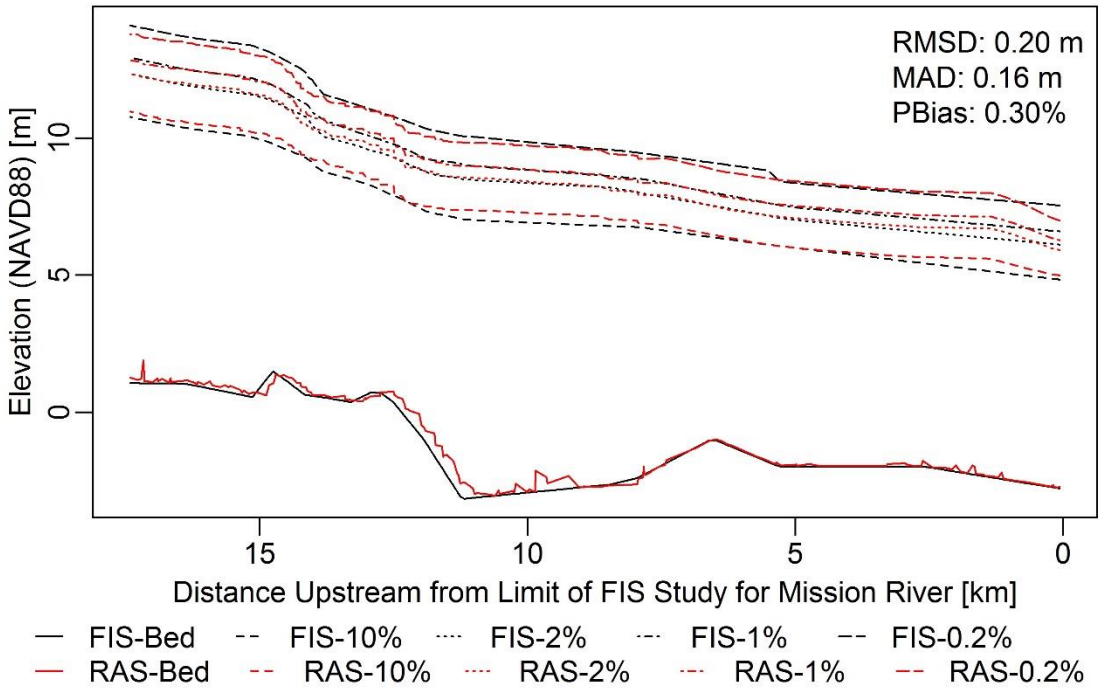

Figure B-2. Comparison of longitudinal water surface elevation (WSE) profiles between the FEMA flood insurance study (FIS) and our HEC-RAS simulations. Goodness-of-fit indicators (root mean squared deviation (RMSD), mean absolute deviation (MAD), and percent bias (PBias)) between our simulations and those from the FIS are also shown. (Note: FIS corresponds to profiles from the FEMA-FIS; RAS corresponds to profiles from our simulations; Bed corresponds to the elevation of the stream bed; 10, 2, 1, and 0.2% correspond to the chance of occurring within a given year for the flow scenario.)

Description of Land Classification

Two types of landscape patch – (1) soil-patches and (2) vegetation-patches – were used in the flood and network analysis. Descriptive statistics of the soil-patches are provided in Table B-1 and similar information regarding the vegetation-patches is provided in Table B-2. See *Chapter III: Methods* for a description of how the datasets were developed.

Table B-1. Descriptions and geometric statistics of the 16 soil-based patch types developed by manually delineating channels and other geomorphic features and combing them with an edited version of the Ecological Mapping Systems of Texas (EMST). (Note: values in parentheses pertain to patches that do not become hydrologically connected in any of the 23 flow simulations; na = not applicable; N = patch count; Min = minimum value; Max = maximum value; μ = mean value; σ = standard deviation; and ∑ = sum or total.)

Patch Abbr.	Patch Desc.	Data Source	N	Stage for Conn. (h_c)				Area (A)			Perimeter (P)		
				Min	Max	μ	σ	μ	σ	$\sum$	μ	σ	$\sum$
				[m]				[km^2]			[km]		
MC	Main Channel	Digitized	1 (na)	1.00	1.00	1.00	0.00	1.09 (na)	0.00 (na)	1.09 (na)	34.89 (na)	0.00 (na)	34.89 (na)
T	Tributary	Digitized	6 (na)	1.00	2.50	1.58	0.58	0.08 (na)	0.05 (na)	0.50 (na)	9.75 (na)	5.54 (na)	58.50 (na)
S	Slough	Digitized	7 (na)	2.00	5.50	3.50	1.61	0.03 (na)	0.04 (na)	0.20 (na)	2.67 (na)	2.01 (na)	18.69 (na)
CO	Cutoff/ Oxbow	Digitized	3 (na)	3.00	4.50	3.50	0.87	0.11 (na)	0.10 (na)	0.34 (na)	3.90 (na)	3.08 (na)	11.71 (na)
G	Gully	Digitized	79 (9)	1.50	11.50	6.63	2.92	0.00 (0.00)	0.00 (0.00)	0.07 (0.00)	0.29 (0.13)	0.23 (0.10)	23.16 (1.14)
ST	Small Tributary	Digitized	19 (1)	3.00	11.00	8.05	2.63	0.00 (0.00)	0.00 (0.00)	0.08 (0.00)	1.33 (0.38)	0.78 (0.00)	25.24 (0.38)
LB	Loamy Bottomland	EMST	42 (22)	2.00	10.00	5.68	2.22	0.15 (0.00)	0.29 (0.01)	6.46 (0.00)	2.06 (0.08)	2.80 (0.24)	86.64 (0.62)
CB	Clayey Bottomland	EMST	65 (9)	2.00	9.50	5.16	1.55	0.10 (0.00)	0.23 (0.00)	6.34 (0.00)	1.92 (0.03)	2.97 (0.02)	124.98 (0.28)
TSL	Tight Sandy Loam	EMST	26 (11)	4.00	11.50	8.54	2.57	0.47 (0.02)	0.92 (0.04)	12.13 (0.24)	4.42 (0.56)	6.89 (0.81)	114.80 (6.20)
B	Blackland Prairie	EMST	15 (15)	4.50	11.63	8.94	2.80	0.53 (0.00)	0.67 (0.00)	7.92 (0.02)	4.25 (0.12)	3.84 (0.18)	63.73 (1.86)
LS	Loamy Sand	EMST	22 (8)	2.00	11.50	8.20	2.89	0.20 (0.03)	0.25 (0.06)	4.48 (0.23)	2.78 (0.47)	2.70 (0.80)	61.05 (0.28)
C	Claypan Prairie	EMST	17 (11)	9.50	11.63	10.68	0.57	0.08 (0.22)	0.09 (0.25)	1.39 (2.37)	1.86 (2.54)	1.82 (2.09)	31.54 (27.90)
RB	Rolling Blackland	EMST	29 (9)	4.00	11.50	7.34	2.56	0.05 (0.00)	0.12 (0.00)	1.58 (0.00)	1.34 (0.03)	1.63 (0.03)	38.93 (0.28)
SH	Sand Hills	EMST	2 (na)	5.50	6.50	6.00	0.71	0.38 (na)	0.42 (na)	0.75 (na)	2.24 (na)	1.42 (na)	4.48 (na)
SL	Sandy Loam	EMST	1 (na)	11.00	11.00	11.00	0.00	0.04 (na)	0.00 (na)	0.04 (na)	1.14 (na)	0.00 (na)	1.14 (na)
L	Lakebed	EMST	na (1)	na	na	na	na	na (0.07)	na (0.00)	na (0.07)	na (1.22)	na (0.00)	na (1.22)
TOT	Total	All	334 (96)	1.00	11.63	6.39	1.09	0.13 (0.03)	0.37 (0.11)	43.38 (2.94)	2.09 (0.45)	3.76 (1.08)	699.5 (43.61)

Table B-2. Descriptions and geometric statistics of the 20 vegetation-based patch types developed by manually delineating features and combing them with an edited version of the Ecological Mapping Systems of Texas (EMST). (Note: values in parentheses pertain to patches that do not become hydrologically connected in any of the 23 flow simulations; na = not applicable; FP = floodplain; UL = upland; Herb = herbaceous; HW = hardwood; Mes. = mesquite; EG = evergreen; Dec. = deciduous; Anth. = anthropogenic; comp. = composite; N = patch count; Min = minimum value; Max = maximum value; μ = mean value; σ = standard deviation; and ∑ = sum or total.)

Patch Abbr.	Patch Desc.	Data Source	*N*	Stage for Conn. (h_c)				Area (*A*)			Perimeter (*P*)		
				Min	Max	*μ*	*σ*	*μ*	*σ*	∑	*μ*	*σ*	∑
				[m]				[km^2]			[km]		
MC	Main Channel	Digitized	1 (na)	1.00	1.00	1.00	0.00	1.09 (na)	0.00 (na)	1.09 (na)	34.89 (na)	0.00 (na)	34.89 (na)
T	Tributary	Digitized	6 (na)	1.00	2.50	1.58	0.58	0.08 (na)	0.05 (na)	0.50 (na)	9.75 (na)	5.54 (na)	58.50 (na)
S	Slough	Digitized	7 (na)	2.00	5.50	3.50	1.61	0.03 (na)	0.04 (na)	0.20 (na)	2.67 (na)	2.01 (na)	18.69 (na)
CO	Cutoff/ Oxbow	Digitized	3 (na)	3.00	4.50	3.50	0.87	0.11 (na)	0.10 (na)	0.34 (na)	3.90 (na)	3.08 (na)	11.71 (na)
G	Gully	Digitized	79 (9)	1.50	11.50	6.63	2.92	0.00 (0.00)	0.00 (0.00)	0.07 (0.00)	0.29 (0.13)	0.23 (0.10)	23.16 (1.14)
ST	Small Tributary	Digitized	19 (1)	3.00	11.00	8.05	2.63	0.00 (0.00)	0.00 (0.00)	0.08 (0.00)	1.33 (0.38)	0.78 (0.00)	25.24 (0.38)
OW	Open Water	EMST	2 (1)	5.50	8.00	6.75	1.77	0.04 (0.00)	0.05 (0.00)	0.07 (0.00)	1.40 (0.03)	1.67 (0.00)	2.81 (0.03)
CW	Coastal Wetland	EMST Comp.	4 (5)	4.50	7.00	5.50	1.22	0.01 (0.00)	0.02 (0.00)	0.04 (0.00)	0.59 (0.04)	0.76 (0.02)	2.35 (0.18)
FHW	FP Herb Wetland	EMST Comp.	17 (2)	4.50	9.00	6.53	1.33	0.01 (0.00)	0.02 (0.00)	0.17 (0.00)	0.53 (0.02)	0.46 (0.00)	9.05 (0.04)
FHF	FP HW Forest	EMST Comp.	212 (64)	2.00	11.63	6.16	2.36	0.03 (0.00)	0.08 (0.00)	6.32 (0.01)	0.97 (0.04)	1.73 (0.06)	205.34 (2.30)
FG	FP Grassland	EMST Comp.	47 (14)	3.50	10.00	5.95	1.91	0.05 (0.00)	0.16 (0.00)	2.53 (0.01)	1.39 (0.13)	2.01 (0.25)	65.15 (1.88)
FMF	FP Mixed Forest	EMST Comp.	131 (42)	3.50	11.50	6.44	2.07	0.01 (0.00)	0.02 (0.00)	1.63 (0.01)	0.71 (0.04)	0.75 (0.09)	92.65 (1.86)
FOF	FP Live Oak Forest	EMST Comp.	147 (38)	2.00	11.50	6.43	2.27	0.01 (0.00)	0.02 (0.00)	1.26 (0.00)	0.55 (0.03)	0.62 (0.03)	81.36 (1.15)
FDS	FP Dec. Shrubs	EMST Comp.	81 (28)	3.50	11.00	6.30	1.80	0.01 (0.00)	0.02 (0.00)	0.83 (0.00)	0.64 (0.04)	0.68 (0.09)	52.03 (1.16)
FES	FP EG Shrubs	EMST Comp.	23 (7)	4.50	11.00	6.80	2.11	0.00 (0.00)	0.00 (0.00)	0.09 (0.01)	0.37 (0.13)	0.28 (0.25)	8.48 (0.92)

Table B-2 (continued). Descriptions and geometric statistics of the 20 vegetation-based patch types developed by manually delineating features and combing them with an edited version of the Ecological Mapping Systems of Texas (EMST). (Note: values in parentheses pertain to patches that do not become hydrologically connected in any of the 23 flow simulations; na = not applicable; FP = floodplain; UL = upland; Herb = herbaceous; HW = hardwood; Mes. = mesquite; EG = evergreen; Dec. = deciduous; Anth. = anthropogenic; comp. = composite; N = patch count; Min = minimum value; Max = maximum value; μ = mean value; σ = standard deviation; and ∑ = sum or total.)

Patch Abbr.	Patch Desc.	Data Source	*N*	Stage for Conn. (h_c)				Area (*A*)			Perimeter (*P*)		
				Min	Max	*μ*	*σ*	*μ*	*σ*	∑	*μ*	*σ*	∑
				[m]				[km^2]			[km]		
UPG	UL Praire/ Grassland	EMST Comp.	71 (67)	4.50	11.63	8.61	2.30	0.14 (0.03)	0.31 (0.09)	9.96 (1.95)	2.49 (1.01)	4.22 (2.38)	176.66 (67.63)
UMW	UL Mes. Woods	EMST Comp.	160 (111)	4.00	11.63	9.02	2.12	0.04 (0.01)	0.12 (0.03)	6.51 (1.28)	1.34 (0.59)	2.34 (0.82)	214.63 (65.70)
UDW	UL Dec. Woods	EMST Comp.	183 (142)	2.00	11.63	8.81	2.33	0.03 (0.01)	0.06 (0.04)	4.75 (1.55)	1.05 (0.51)	1.31 (0.92)	192.32 (72.06)
UEW	UL EG Woods	EMST Comp.	20 (35)	7.00	11.50	10.63	1.12	0.02 (0.01)	0.03 (0.04)	0.34 (0.52)	0.71 (0.61)	0.67 (0.67)	14.30 (21.40)
A	Anth.	EMST Comp.	53 (28)	4.00	11.50	8.25	2.19	0.08 (0.00)	0.31 (0.00)	4.13 (0.12)	1.42 (0.43)	3.06 (0.37)	75.31 (12.01)
TOT	Total	All	777 (594)	1.00	11.63	5.41	0.79	0.03 (0.01)	0.12 (0.04)	40.91 (5.46)	2.09 (0.42)	3.76 (1.04)	699.5 (249.86)

Spatial Datasets Developed Using Hydrodynamic Simulations

The 23 hydrodynamic simulations were used to develop maps of inundation within the study area and this is shown in Figure B-2. An overlay analysis between these inundation maps and the land classifications is used to determine the state of the landscape network for each simulation. Figure B-3 and B-4 show the 23 states of the soil- and vegetation-network, respectfully.

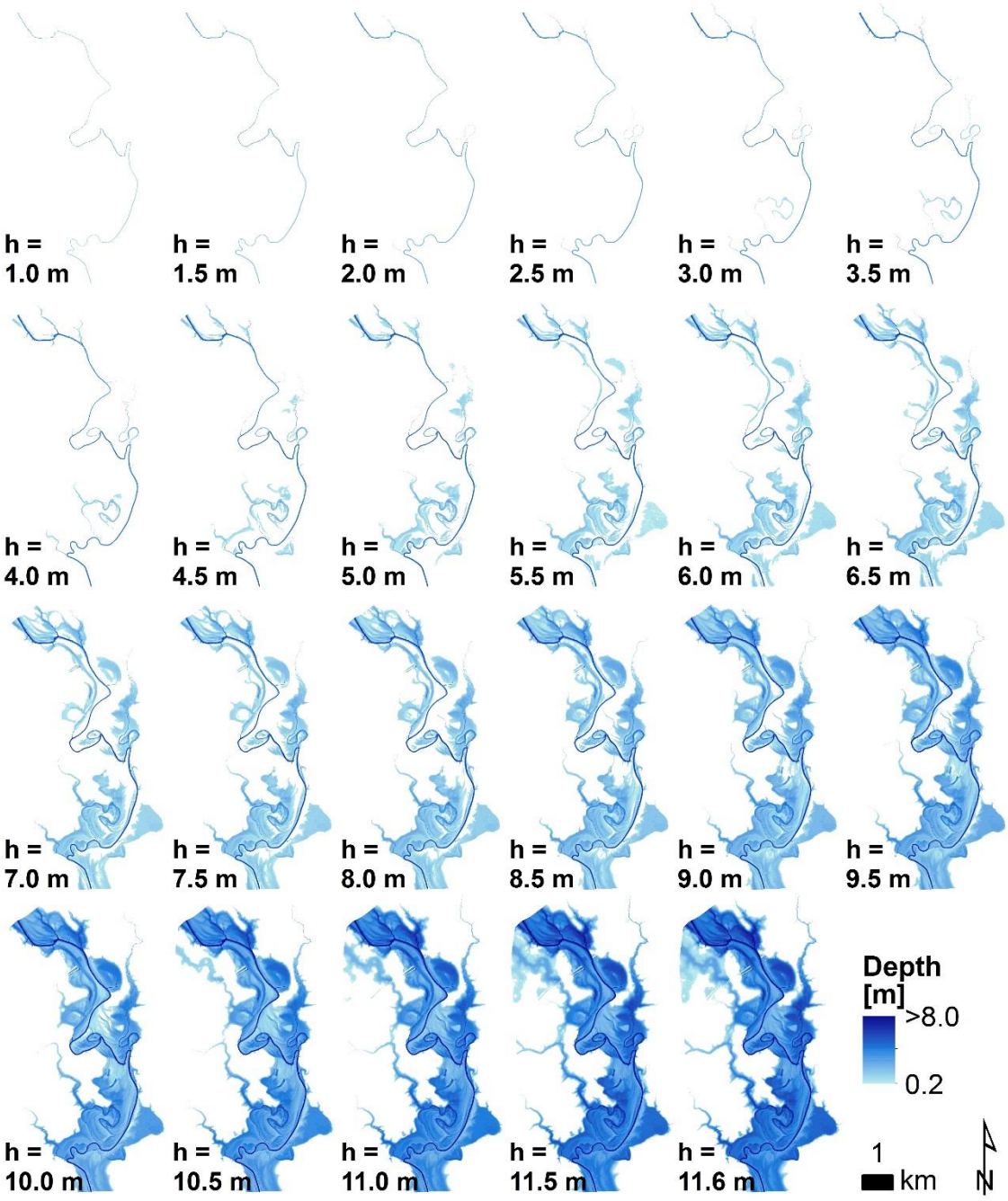

Figure B-3. Maps of the depth of inundation within the study area for the 23 hydrodynamic flow simulations. These are considered steady and they were generated using a two-dimensional HEC-RAS model. The stage (h) associated with each flow is also shown on the lower-left part of each of the maps within the figure.

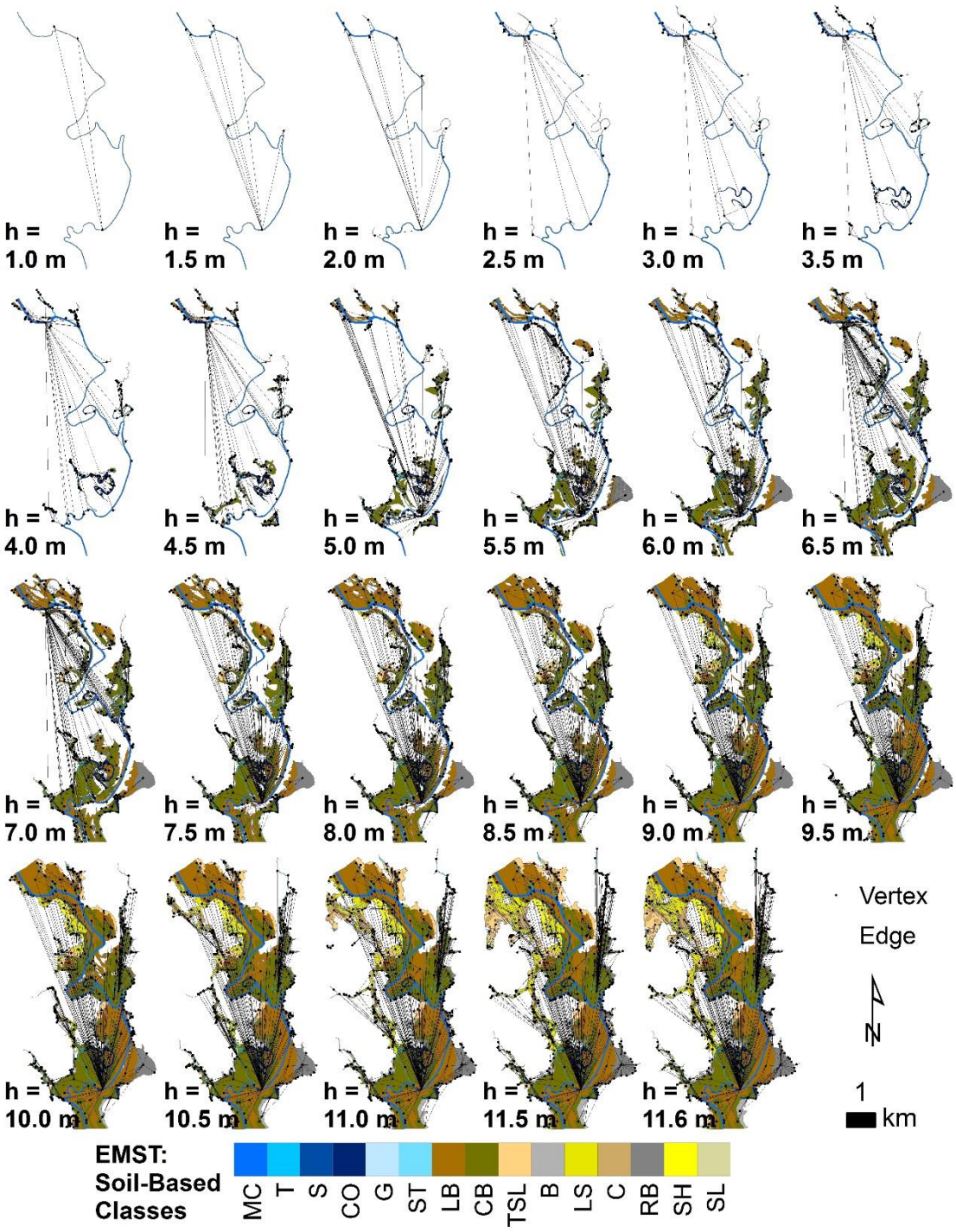

Figure B-4. Maps of the soil-patches that become hydrologically connected with each of the 23 flow simulations. The soil-network that is created by the surface-water connections is also shown (position of a network vertex on its corresponding patch is chosen arbitrarily). The stage (h) associated with each flow is also shown on the lower-left part of each map. (Note: See Table B-1 for patch-type descriptions)

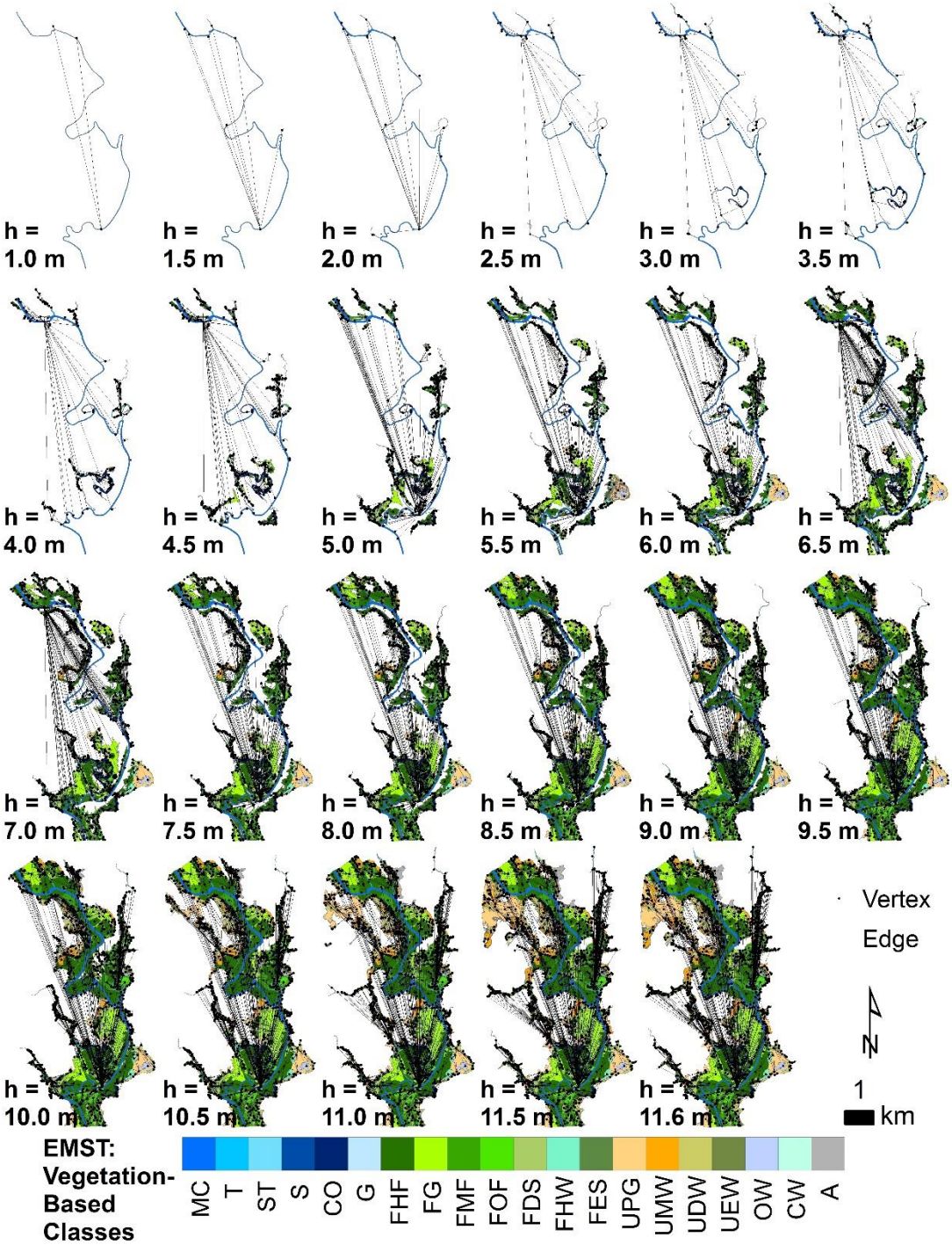

Figure B-5. Maps of the vegetation-patches that become hydrologically connected with each of the 23 flow simulations. The network that is created by the surface-water connections is also shown (the location of a network vertex on its corresponding patch is chosen arbitrarily). The stage (h) associated with each flow is also shown on the lower-left part of each map. (Note: See Table B-2 for patch-type descriptions)

Other Topological and Algebraic Network Metrics

Network-level metrics for the topological and algebraic properties of each network state were computed and plotted as a function of the stage (h) associated with each flow simulation (Figure B-5). See *Chapter III: Methods* for descriptions of the metrics and what they represent.

In the channel-inundation phase (simulations with $1.0 \leq h \leq 2.5$ m) where most of the between-patch connections occur in the vicinity of active channels. The number of vertices in each network state (n) increases linearly from 3 to 25 for both networks as patches of floodplain channel and geomorphic features become hydrologically connected. The number of edges (m) normalized by the theoretical minimum and maximum values for a given n (or normalized m; m_{norm}) reaches its highest values (0.01 and 0.02 for the soil- and vegetation-networks, respectively), but the values remain near the theoretical minimum. This is because patches are only allowed to connect to patches with whom they share a border in our network conceptualization. The mean vertex degree ($\bar{k}$; degree is the number of other vertices a given vertex is connected with) for the soil- and vegetation-networks increase linearly by 74.4 and 68.4%, respectively, with general $\bar{k}$ values that are >2. Similarly, the mean geodesic distance (l) for these networks increases linearly by 63.2 and 69.2%. This is mostly because of the development of small chains of connected patches along the periphery of the MC and T patches. The formation of these chains also results in the increases of the clustering coefficient (C; also known as transitivity) from the theoretical minimum of zero to ~0.07. The central betweenness (C_{btw}, also known as centralization index) decreases by ~6% from the

theoretical maximum of 1.0 and this is because of the outward spread of surface water from the MC patch. There are also decreases for the ratios between the spectral radius (λ_1) and the theoretical upper bound ($\lambda_1/\lambda_{upper}$; decreases by ~27.0% for both networks) and theoretical maximum (λ_1/λ_{maz}; decreases by ~73.0% for both networks); the relative contribution of the network wiring to λ_1 (ξ_{wir}; decreases by 62.1% for both networks); and the algebraic connectivity ($\lambda(A)_{N-1}$) normalized by the theoretical minimum and maximum ($\lambda(A)_{N-1,norm}$; decreases by ~79.5% for both networks). These decreases are because of the of the overall growth of the network with increased flow. In particular, the increases in the relative contribution of the network wiring to λ_1 (ξ_{conn}; increases by 36.5% for both networks) indicates that the increase in the number of edges (m) is the main cause for the decline of the value for these metrics.

In the some-floodplain-inundation phase (simulations with $3.0 \leq h \leq 8.0$ m) where patches in and around geomorphic features within the floodplain become inundated. There is a dramatic increase in the amount of inundated area during this phase (Figure 2a and 2b) and this results in n increasing exponentially from 39 to 365 for the soil-network and 41 to 1007 for the vegetation-based network. m_{norm} initially declines towards the theoretical minimum then it generally remains near these values for the latter half of the phase. A vertex that is associated with a particular patch is only allowed to connect to vertices associated with patches that border the host patch. This is why m_{norm} approaches the theoretical minimum and stays in that vicinity as the network continues to grow. $\bar{k}$ experiences a slight decline early in the some-floodplain-inundation phase, but then it increases on a roughly logarithmic trajectory ($\bar{k}$ increases by 55.7 and 84.3%

for the soil- and vegetation-networks, respectively). The increased number of vertices that become connected to the MC, T, CO, and S patches due to the inundation in and around these features cause the relatively steady increase in $\bar{k}$ for both networks. l sharply increases in both networks (l increases by 66.7 and 92.0% for the soil- and vegetation-networks, respectively) for simulations with $3.0 \leq h \leq 5.5$ m. This dramatic increase is due to the large number of patches that become newly inundated during this portion of the inundation phase. There is relatively modest general decline in l (decreases by 13.2 and 22.9% for the soil- and vegetation-networks, respectively) for the remaining simulations in the some-floodplain-inundation phase and this is because of the inundation of patches that connect previously inundated portions of the landscape and provide shortcuts in the path. C for both networks experiences a general increase on a roughly logarithmic trajectory (C increases by 57.1 and 150% for the soil- and vegetation-networks, respectively). This increase is related to the shortcuts mentioned above that connect previously inundated patches. C_{btw} continues the decreasing trend from the channel-inundation phase for most of the simulations ($3.0 \leq h \leq 6.5$ m) in the some-floodplain-inundation phase (C_{btw} decreases by 8.7 and 7.7% for the soil- and vegetation-network). For simulations with $7.0 \leq h \leq 8.0$ m, C_{btw} initially increases slightly (~5%) than it oscillates with no overall change for both networks. This behavior of a general decline is associated with the overall expansion of flood waters onto floodplain that decreases the centralization of the network. $\lambda_1/\lambda_{upper}$, λ_1/λ_{maz}, ξ_{wir}, and $\lambda(A)_{N-1,norm}$ all exhibit declines with a similar trend for simulations with $3.0 \leq h \leq 5.0$ m. These declines are associated with how m stays close to the theoretical minimum with

network connectivity (ξ_{conn}) that is largely driven by patches that become inundated with simulations that have a relatively low *h*.

The overbank-inundation phase ($h \geq 8.5$ m) is associated with simulations where large portions of the floodplain become inundated with multiple upstream-downstream flow-paths within the floodplain. With the exception of *n*, $\bar{k}$, and C_{btw} that experience some dynamic behavior with increasing *h* (*n* and $\bar{k}$ increase while C_{btw} decreases), all other network metrics experience little-to-no change in the overbank-inundation phase (Figure B-5). The dynamics in *n*, $\bar{k}$, and C_{btw} are most apparent for simulation with $h \geq$ 10.5 m because flood water spill onto upland parts of the coastal plain allowing new flow-paths with high patch connectivity to develop.

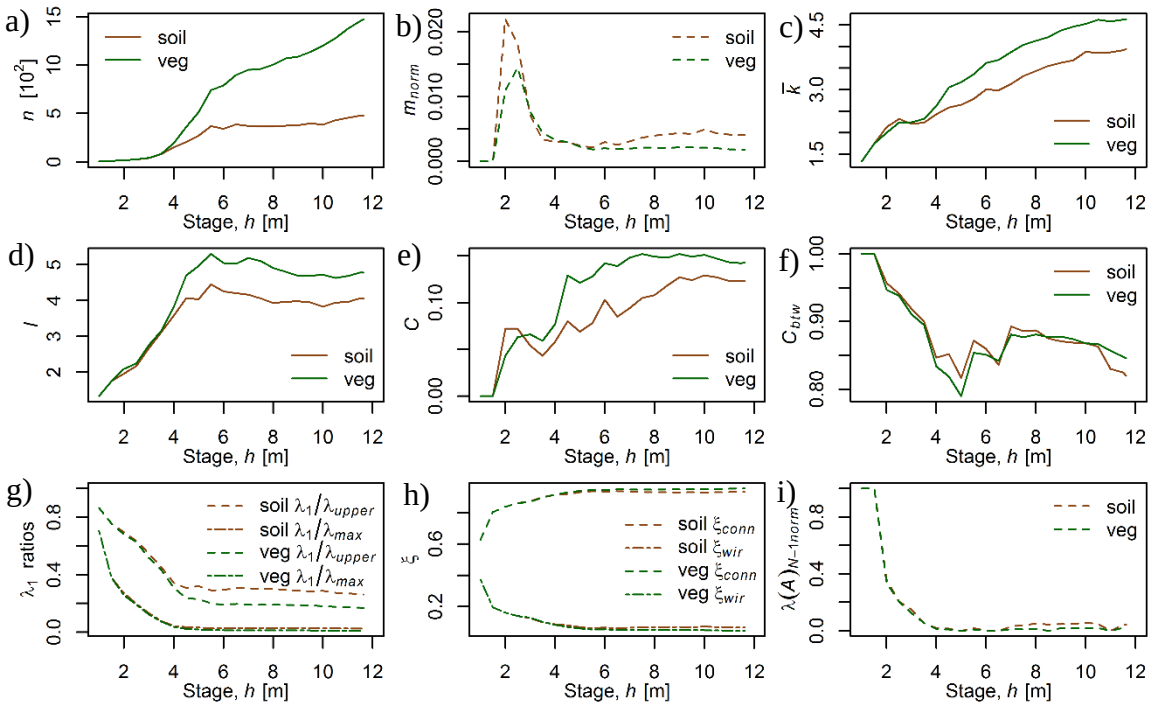

Figure B-6. Algebraic metrics for the network created by each of the 23 flow simulations plotted against stage (h). These metrics include: a) the number of vertices (n); b) the number of edges (m) normalized by the theoretical minimum and maximum m; c) the mean vertex degree ($\bar{\bar{k}}$); d) the mean shortest between vertex pairs (l); e) normalized clustering/transmissivity coefficient (C); f) the betweenness centrality (C_{btw}); g) ratios between the spectral radius and theoretical upper bounds ($\lambda_1/\lambda_{upper}$) and maximums ($\lambda_1/\lambda_{max}$); h) relative contributions to the spectral radius from connectivity (ξ_{conn}) and wiring (ξ_{wir}); and the algebraic connectivity normalized by the theoretical minimum and maximum algebraic connectivity ($\lambda(A)_{N-1_{norm}}$) for each network.

References

DAVIS, N. A. & SMITH, E. H. 2013. Dynamics of a community of dominant woody riparian species along a coastal river of texas. Southwestern Naturalist, 58**,** 286-298.

FEMA 2014. Flood Insurance Study: Refugio County, Texas and Incorporated Areas. Flood Insurance Studies. Denton, TX: Federal Emergency Management Agency.

FULBRIGHT, T. E., DIAMOND, D. D., RAPPOLE, J. & NORWINE, J. 1990. The Coastal Sand Plain of Southern Texas. Rangelands, 12**,** 337-340.

HUDSON, P. F., SOUNNY-SLITTINE, M. A. & LAFEVOR, M. 2013. A new longitudinal approach to assess hydrologic connectivity: Embanked floodplain inundation along the lower Mississippi River. Hydrological Processes, 27**,** 2187-2196.

NELSON, J. & TOLAN, J. 2008. Final Historical Data Review on Mission River and Aransas River Tidal. Austin, TX: Texas Parks and Wildlife Department.

NORWINE, J. & JOHN, K. 2007. *The changing climate of South Texas, 1900-2100 : problems and prospects, impacts and implications*, Kingsville, TX : CREST-RESSACA, Texas A & M University-Kingsville, 2007.

TOCKNER, K., MALARD, F. & WARD, J. V. 2000. An extension of the flood pulse concept. Hydrological Processes, 14**,** 2861-2883.

APPENDIX C

SUPPORTING INFORMATION FOR CHAPTER IV

Introduction

This Appendix is provided to further describe the linear-spline models that were fitted to the calibration data from Stream Temperature, Intermittency, and Conductivity loggers (STICLs). We used calibration-trials that involved submerging our STICLs in calibration standards so that the "light intensity" values that the data loggers were originally intended to record can be used to predict electrical conductivity (*EC*) of inundating waters. We fit linear-splines to the calibration data for the two phases of STICL development that was undertaken. The coefficients and some of the diagnostics of these fits are shown in Tables C-1 and C-2.

Fitted Linear-Spline Models

Table C-1. Description of the linear spline model fits to the ten STICLs that were part of the phase 1 deployment. The electrical conductivity (EC) for the trials are 0 (distilled water), 84, 1413, 2070, 8974, 15000, and 80000 µS/cm. The range of EC values included in the model for each STICL (EC_{range}), the x-values for the linear spline knots (x_n), the slopes (β_n) of the lines between knots, the standard error (SE) for the slope estimates ($SE_{\beta n}$), and the SE for the model fit (SE_{mod}) are also shown. All fitted linear spline models area statistically significant at the $\alpha = 0.05$ level and an * next to β_n indicates that the estimate is statistically significant at the $\alpha = 0.05$ level.

Logger ID	EC_{range} [µS/cm]	x_n	β_n	$SE_{\beta n}$	SE_{mod} [µS/cm]
S02	0 – 8,974	x_1 = 3,619	β_1 = 2.41E-03*	$SE_{\beta 1}$ = 9.67E-05	201.06
		x_2 = 34,445	β_2 = 8.08E-03*	$SE_{\beta 2}$ = 2.90E-05	
		x_3 = 198,897	β_3 = 1.57E-02*	$SE_{\beta 3}$ = 1.10E-04	
		x_4 = 242,491	β_4 = 8.44E-02*	$SE_{\beta 4}$ = 5.81E-05	
S03	0 – 8,974	x_1 = 2,004	β_1 = 2.10E-03*	$SE_{\beta 1}$ = 8.88E-05	213.17
		x_2 = 39,956	β_2 = 8.36E-03*	$SE_{\beta 2}$ = 3.23E-05	
		x_3 = 200,777	β_3 = 1.25E-02*	$SE_{\beta 3}$ = 1.50E-04	
		x_4 = 238,654	β_4 = 8.33E-02*	$SE_{\beta 4}$ = 6.32E-05	
S04	0 – 8,974	x_1 = 4,376	β_1 = 1.69E-03*	$SE_{\beta 1}$ = 5.27E-06	15.74
		x_2 = 49,600	β_2 = 7.76E-03*	$SE_{\beta 2}$ = 2.24E-06	
		x_3 = 219,013	β_3 = 1.95E-02*	$SE_{\beta 3}$ = 1.12E-05	
		x_4 = 253,513	β_4 = 8.95E-02*	$SE_{\beta 4}$ = 4.81E-06	
S06	0 – 8,974	x_1 = 4,430	β_1 = 2.06E-03*	$SE_{\beta 1}$ = 1.16E-04	278.92
		x_2 = 40,063	β_2 = 9.90E-03*	$SE_{\beta 2}$ = 5.12E-05	
		x_3 = 172,667	β_3 = 2.73E-02*	$SE_{\beta 3}$ = 2.68E-04	
		x_4 = 198,701	β_4 = 8.15E-02*	$SE_{\beta 4}$ = 7.87E-05	
S08	0 – 8,974	x_1 = 2,982	β_1 = 1.99E-03*	$SE_{\beta 1}$ = 1.50E-04	346.39
		x_2 = 39,447	β_2 = 8.81E-03*	$SE_{\beta 2}$ = 5.75E-05	
		x_3 = 189,798	β_3 = 2.03E-02*	$SE_{\beta 3}$ = 2.81E-04	
		x_4 = 222,063	β_4 = 8.28E-02*	$SE_{\beta 4}$ = 1.02E-04	
S10	0 – 8,974	x_1 = 4,133	β_1 = 4.62E-03*	$SE_{\beta 1}$ = 4.10E-04	422.45
		x_2 = 16,533	β_2 = 1.39E-02*	$SE_{\beta 2}$ = 9.64E-05	
		x_3 = 121,245	β_3 = 5.00E-03*	$SE_{\beta 3}$ = 3.82E-04	
		x_4 = 154,312	β_4 = 1.37E-01*	$SE_{\beta 4}$ = 2.24E-04	
S12	0 – 8,974	x_1 = 3,160	β_1 = 1.91E-03*	$SE_{\beta 1}$ = 8.57E-06	22.73
		x_2 = 44,089	β_2 = 6.75E-03*	$SE_{\beta 2}$ = 2.88E-06	
		x_3 = 238,360	β_3 = 1.39E-02*	$SE_{\beta 3}$ = 1.18E-05	
		x_4 = 286,580	β_4 = 1.57E-01*	$SE_{\beta 4}$ = 1.21E-05	
S13	0 – 8,974	x_1 = 3,949	β_1 = 1.96E-03*	$SE_{\beta 1}$ = 6.22E-05	160.09
		x_2 = 42,711	β_2 = 8.41E-03*	$SE_{\beta 2}$ = 2.48E-05	
		x_3 = 202,875	β_3 = 1.19E-02*	$SE_{\beta 3}$ = 1.16E-04	
		x_4 = 240,718	β_4 = 7.87E-02*	$SE_{\beta 4}$ = 4.48E-05	
S14	0 – 8,974	x_1 = 2,125	β_1 = 2.25E-03*	$SE_{\beta 1}$ = 5.90E-05	131.89
		x_2 = 37,240	β_2 = 7.76E-03*	$SE_{\beta 2}$ = 1.82E-05	
		x_3 = 209,179	β_3 = 1.56E-02*	$SE_{\beta 3}$ = 9.40E-05	
		x_4 = 244,490	β_4 = 8.12E-02*	$SE_{\beta 4}$ = 3.77E-05	

Table C-2. Description of the linear spline models fits to the 18 STICLs that were part of the phase 2 deployment. The electrical conductivity (EC) for the trials are 23, 84, 447, 1413, 2764, 8974, and 15000 µS/cm. The range of EC values included in the model for each STICL (EC_{range}), the x-values for the linear spline knots (x_n), the slopes (β_n) of the lines between knots, the standard error (SE) for the slope estimates ($SE_{\beta n}$), and the SE for the model fit (SE_{mod}) are also shown. All fitted linear spline models area statistically significant at the $\alpha = 0.05$ level and an * next to β_n indicates that the estimate is statistically significant at the $\alpha = 0.05$ level.

Logger ID	EC_{range} [µS/cm]	x_n	β_n	$SE_{\beta n}$	SE_{mod} [µS/cm]
L01	23 – 8,974	x_1 = 18,025	B_1 = 1.44E-03*	$SE_{\beta 1}$ = 2.17E-04	456.42
		x_2 = 57,867	B_2 = 3.78E-03*	$SE_{\beta 2}$ = 1.89E-04	
		x_3 = 154,312	B_3 = 1.57E-02*	$SE_{\beta 3}$ = 2.85E-04	
		x_4 = 220,354	B_4 = 7.45E-02*	$SE_{\beta 4}$ = 1.63E-03	
		x_5 = 234,830	B_5 = 2.01E-01*	$SE_{\beta 5}$ = 7.13E-04	
L05	23 – 8,974	x_1 = 44,089	β_1 = 1.13E-03*	$SE_{\beta 1}$ = 2.71E-04	663.63
		x_2 = 55,112	β_2 = 3.67E-03*	$SE_{\beta 2}$ = 2.32E-04	
		x_3 = 159,823	β_3 = 1.61E-02*	$SE_{\beta 3}$ = 4.47E-04	
		x_4 = 220,446	β_4 = 2.55E-02*	$SE_{\beta 4}$ = 6.34E-04	
		x_5 = 267,033	β_5 = 3.19E-01*	$SE_{\beta 5}$ = 1.55E-03	
L06	23 – 8,974	x_1 = 35,177	β_1 = 1.37E-03*	$SE_{\beta 1}$ = 3.88E-04	767.96
		x_2 = 45,901	β_2 = 3.84E-03*	$SE_{\beta 2}$ = 3.08E-04	
		x_3 = 141,080	β_3 = 1.78E-02*	$SE_{\beta 3}$ = 5.63E-04	
		x_4 = 198,401	β_4 = 4.45E-02*	$SE_{\beta 4}$ = 1.38E-03	
		x_5 = 225,268	β_5 = 2.84E-01*	$SE_{\beta 5}$ = 1.75E-03	
L08	23 – 8,974	x_1 = 41,334	β_1 = 1.20E-03*	$SE_{\beta 1}$ = 2.00E-04	447.02
		x_2 = 50,312	β_2 = 3.72E-03*	$SE_{\beta 2}$ = 1.58E-04	
		x_3 = 154,312	β_3 = 1.53E-02*	$SE_{\beta 3}$ = 2.76E-04	
		x_4 = 220,446	β_4 = 2.11E-02*	$SE_{\beta 4}$ = 5.36E-04	
		x_5 = 259,437	β_5 = 2.50E-01*	$SE_{\beta 5}$ = 8.01E-04	
L09	23 – 8,974	x_1 = 37,200	β_1 = 1.37E-03*	$SE_{\beta 1}$ = 1.95E-04	389.39
		x_2 = 44,089	β_2 = 4.39E-03*	$SE_{\beta 2}$ = 1.68E-04	
		x_3 = 130,623	β_3 = 1.29E-02*	$SE_{\beta 3}$ = 2.50E-04	
		x_4 = 204,868	β_4 = 5.59E-02*	$SE_{\beta 4}$ = 1.14E-03	
		x_5 = 224,671	β_5 = 1.60E-01*	$SE_{\beta 5}$ = 4.68E-04	
L11	23 – 8,974	x_1 = 37,200	β_1 = 1.37E-03*	$SE_{\beta 1}$ = 2.03E-04	405.92
		x_2 = 44,089	β_2 = 4.51E-03*	$SE_{\beta 2}$ = 1.80E-04	
		x_3 = 127,969	β_3 = 1.53E-02*	$SE_{\beta 3}$ = 2.93E-04	
		x_4 = 188,986	β_4 = 7.31E-02*	$SE_{\beta 4}$ = 8.51E-04	
		x_5 = 209,424	β_5 = 1.47E-01*	$SE_{\beta 5}$ = 3.97E-04	
L13	23 – 8,974	x_1 = 46,845	β_1 = 1.05E-03*	$SE_{\beta 1}$ = 8.57E-05	226.05
		x_2 = 60,377	β_2 = 3.66E-03*	$SE_{\beta 2}$ = 7.94E-05	
		x_3 = 165,334	β_3 = 1.03E-02*	$SE_{\beta 3}$ = 9.28E-05	
		x_4 = 264,535	β_4 = 3.20E-02*	$SE_{\beta 4}$ = 3.86E-04	
		x_5 = 292,265	β_5 = 1.71E-01*	$SE_{\beta 5}$ = 2.77E-04	

Table C-3 (continued). Description of the linear spline models fits to the 18 STICLs that were part of the phase 2 deployment. The electrical conductivity (EC) for the trials are 23, 84, 447, 1413, 2764, 8974, and 15000 µS/cm. The range of EC values included in the model for each STICL (EC_{range}), the x-values for the linear spline knots (x_n), the slopes (β_n) of the lines between knots, the standard error (SE) for the slope estimates ($SE_{\beta n}$), and the SE for the model fit (SE_{mod}) are also shown. All fitted linear spline models area statistically significant at the $\alpha = 0.05$ level and an * next to β_n indicates that the estimate is statistically significant at the $\alpha = 0.05$ level.

Logger ID	EC_{range} [µS/cm]	x_n	β_n	$SE_{\beta n}$	SE_{mod} [µS/cm]
L14	23 – 8,974	x_1 = 39,879	β_1 = 1.20E-03*	$SE_{\beta 1}$ = 2.09E-04	492.66
		x_2 = 55,112	β_2 = 4.66E-03*	$SE_{\beta 2}$ = 2.21E-04	
		x_3 = 137,779	β_3 = 7.37E-03*	$SE_{\beta 3}$ = 1.96E-04	
		x_4 = 249,425	β_4 = 6.37E-02*	$SE_{\beta 4}$ = 8.57E-04	
		x_5 = 275,805	β_5 = 1.89E-01*	$SE_{\beta 5}$ = 6.41E-04	
L15	23 – 8,974	x_1 = 40,888	β_1 = 1.19E-03*	$SE_{\beta 1}$ = 5.06E-04	1161.96
		x_2 = 52,698	β_2 = 5.61E-03*	$SE_{\beta 2}$ = 6.26E-04	
		x_3 = 121,245	β_3 = 1.10E-02*	$SE_{\beta 3}$ = 5.59E-04	
		x_4 = 210,618	β_4 = 1.64E-01*	$SE_{\beta 4}$ = 4.99E-03	
		x_5 = 222,127	β_5 = 5.11E-01*	$SE_{\beta 5}$ = 5.41E-03	
L16	23 – 8,974	x_1 = 34,611	β_1 = 1.40E-03*	$SE_{\beta 1}$ = 1.30E-04	263.05
		x_2 = 46,845	β_2 = 4.84E-03*	$SE_{\beta 2}$ = 1.30E-04	
		x_3 = 123,698	β_3 = 1.15E-02*	$SE_{\beta 3}$ = 1.30E-04	
		x_4 = 210,774	β_4 = 2.12E-02*	$SE_{\beta 4}$ = 3.04E-04	
		x_5 = 250,849	β_5 = 2.64E-01*	$SE_{\beta 5}$ = 4.77E-04	
L17	23 – 8,974	x_1 = 39,116	β_1 = 1.21E-03*	$SE_{\beta 1}$ = 1.08E-04	252.37
		x_2 = 55,112	β_2 = 4.67E-03*	$SE_{\beta 2}$ = 1.21E-04	
		x_3 = 135,046	β_3 = 1.07E-02*	$SE_{\beta 3}$ = 1.26E-04	
		x_4 = 223,220	β_4 = 3.17E-02*	$SE_{\beta 4}$ = 2.66E-04	
		x_5 = 264,976	β_5 = 2.88E-01*	$SE_{\beta 5}$ = 4.84E-04	
L18	23 – 8,974	x_1 = 35,034	β_1 = 1.39E-03*	$SE_{\beta 1}$ = 2.15E-04	435.61
		x_2 = 46,845	β_2 = 5.86E-03*	$SE_{\beta 2}$ = 2.55E-04	
		x_3 = 111,316	β_3 = 1.24E-02*	$SE_{\beta 3}$ = 2.48E-04	
		x_4 = 191,071	β_4 = 4.97E-02*	$SE_{\beta 4}$ = 9.47E-04	
		x_5 = 215,109	β_5 = 1.09E-01*	$SE_{\beta 5}$ = 3.45E-04	
L22	23 – 8,974	x_1 = 34,712	β_1 = 1.28E-03*	$SE_{\beta 1}$ = 2.85E-04	643.50
		x_2 = 55,112	β_2 = 4.55E-03*	$SE_{\beta 2}$ = 2.94E-04	
		x_3 = 137,779	β_3 = 1.96E-02*	$SE_{\beta 3}$ = 5.30E-04	
		x_4 = 187,379	β_4 = 2.25E-02*	$SE_{\beta 4}$ = 4.82E-04	
		x_5 = 246,330	β_5 = 1.71E-01*	$SE_{\beta 5}$ = 8.06E-04	
L23	23 – 8,974	x_1 = 21,846	β_1 = 1.95E-03*	$SE_{\beta 1}$ = 3.43E-04	511.89
		x_2 = 37,200	β_2 = 5.15E-03*	$SE_{\beta 2}$ = 2.67E-04	
		x_3 = 110,223	β_3 = 2.28E-02*	$SE_{\beta 3}$ = 5.04E-04	
		x_4 = 153,072	β_4 = 2.37E-02*	$SE_{\beta 4}$ = 4.78E-04	
		x_5 = 202,737	β_5 = 1.61E-01*	$SE_{\beta 5}$ = 5.94E-04	

Table C-4 (continued). Description of the linear spline models fits to the 18 STICLs that were part of the phase 2 deployment. The electrical conductivity (EC) for the trials are 23, 84, 447, 1413, 2764, 8974, and 15000 µS/cm. The range of EC values included in the model for each STICL (EC_{range}), the x-values for the linear spline knots (x_n), the slopes (β_n) of the lines between)n knots, the standard error (SE) for the slope estimates ($SE_{\beta n}$), and the SE for the model fit (SE_{mod}) are also shown. All fitted linear spline models area statistically significant at the $\alpha = 0.05$ level and an * next to β_n indicates that the estimate is statistically significant at the $\alpha = 0.05$ level.

Logger ID	EC_{range} [µS/cm]	x_n	β_n	$SE_{\beta n}$	SE_{mod} [µS/cm]
L24	23 – 8,974	x_1 = 25,881	β_1 = 1.48E-03*	$SE_{\beta 1}$ = 3.75E-06	7.26
		x_2 = 50,372	β_2 = 4.26E-03*	$SE_{\beta 2}$ = 3.24E-06	
		x_3 = 137,779	β_3 = 1.59E-02*	$SE_{\beta 3}$ = 4.89E-06	
		x_4 = 198,401	β_4 = 4.09E-02*	$SE_{\beta 4}$ = 8.96E-06	
		x_5 = 231,468	β_5 = 6.26E-02*	$SE_{\beta 5}$ = 2.99E-06	
L26	23 – 8,974	x_1 = 20,340	β_1 = 1.78E-03*	$SE_{\beta 1}$ = 1.02E-04	171.71
		x_2 = 44,089	β_2 = 4.69E-03*	$SE_{\beta 2}$ = 9.05E-05	
		x_3 = 119,863	β_3 = 1.75E-02*	$SE_{\beta 3}$ = 1.27E-04	
		x_4 = 176,357	β_4 = 3.59E-02*	$SE_{\beta 4}$ = 2.11E-04	
		x_5 = 212,032	β_5 = 7.16E-02*	$SE_{\beta 5}$ = 8.49E-05	
L27	23 – 8,974	x_1 = 25,227	β_1 = 1.42E-03*	$SE_{\beta 1}$ = 1.30E-04	273.20
		x_2 = 55,112	β_2 = 5.15E-03*	$SE_{\beta 2}$ = 1.49E-04	
		x_3 = 126,756	β_3 = 1.17E-02*	$SE_{\beta 3}$ = 1.35E-04	
		x_4 = 209,424	β_4 = 6.46E-02*	$SE_{\beta 4}$ = 5.04E-04	
		x_5 = 231,468	β_5 = 1.01E-01*	$SE_{\beta 5}$ = 1.84E-04	
L28	23 – 8,974	x_1 = 23,479	β_1 = 1.56E-03*	$SE_{\beta 1}$ = 1.93E-04	366.06
		x_2 = 49,600	β_2 = 5.16E-03*	$SE_{\beta 2}$ = 1.99E-04	
		x_3 = 121,268	β_3 = 1.20E-02*	$SE_{\beta 3}$ = 1.97E-04	
		x_4 = 199,797	β_4 = 4.11E-02*	$SE_{\beta 4}$ = 4.92E-04	
		x_5 = 232,947	β_5 = 1.33E-01*	$SE_{\beta 5}$ = 3.36E-04	
S15	23 – 2,764	x_1 = 13,949	β_1 = 1.85E-03*	$SE_{\beta 1}$ = 3.95E-05	63.13
		x_2 = 44,565	β_2 = 4.28E-03*	$SE_{\beta 2}$ = 3.11E-05	
		x_3 = 127,652	β_3 = 2.07E-02*	$SE_{\beta 3}$ = 6.14E-05	
		x_4 = 173,027	β_4 = 5.37E-02*	$SE_{\beta 4}$ = 1.07E-04	